# T2R2 東京科学大学 リサーチリポジトリ Science Tokyo Research Repository

### 論文 / 著書情報 Article / Book Information

題目(和文)	高分子フィルムおよびマイクロ・ナノ材料の赤外領域における光学特 性および熱放射特性
Title(English)	Optical Properties and Thermal Radiation of Polymer Films and Micro/Nano Materials in the Infrared Region
著者(和文)	HoangThi Thanh Tam
Author(English)	Tam ThiThanhHoang
出典(和文)	学位:博士(工学), 学位授与機関:東京工業大学, 報告番号:甲第12189号, 授与年月日:2022年9月22日, 学位の種別:課程博士, 審査員:梶川 浩太郎,間中 孝彰,伊藤 治彦,飯野 裕明,三宮 工,久保 若菜
Citation(English)	Degree:Doctor (Engineering), Conferring organization: Tokyo Institute of Technology, Report number:甲第12189号, Conferred date:2022/9/22, Degree Type:Course doctor, Examiner:,,,,,
学位種別(和文)	博士論文
Type(English)	Doctoral Thesis

## OPTICAL PROPERTIES AND THERMAL RADIATION OF POLYMER FILMS AND MICRO/NANO MATERIALS IN THE INFRARED REGION

By:
HOANG THI THANH TAM
Supervisor:
Prof. KOTARO KAJIKAWA
A thesis submitted for the degree of Doctor of Engineering
Department of Electrical and Electronic Engineering, School of Engineering
TOKYO INSTITUTE OF TECHNOLOGY

#### **ACKNOWLEDGEMENTS**

This thesis would not be possible without the support of many people. I want to express my sincere gratitude to my supervisor Prof. Kotaro Kajikawa of the School of Engineering at Tokyo Institute of Technology. His office door always opens whenever I have a question about my research and run into the trouble spots. He always consistently allowed the research in my work but orientated me in the right way whenever he thought I needed it. I could not have imagined having a better advisor and mentor for my Ph.D study.

I express my gratitude to the Japanese Government for awarding me the MEXT scholarship. Without the valuable award, I can not focus on my study.

I am thankful to thesis review committee members: Prof. Takaaki Manaka, Prof. Haruhiko Ito, Prof. Hiroaki Iino, Prof. Takumi Sannomiya and Prof. Wakana Kubo for providing their feedback and valuable suggestions, but also for the hard question which allow me to widen my research from various perspectives.

I am thankful to AGC company for giving me materials and equipment. Furthermore, I am grateful to Prof. Mana Toma for her advice and research support during weekly presentations.

I am thankful to my lab members: Rahul Kumar, Shuto Aizawa, Kento Koike, Nguyen Binh, Kengo Kiyota, Mariko Kobayashi, Shintaro Murai, Naoto Akashi, Yuki Nakamura, Yusuke Kobayashi, Ryoichi Sasaki, Yuji Itakura, Yosuke Sugimoto, Yuki Ito, Tomoya Momose, Shinichi Ikari, Shinnosuke Namihara, Takumi Goto, Kansei Horie, Kei Yoshikawa, Zhou Tong, Hiyabashi, Yanagida and Tsuneoka for the stimulating discussions, and for all the fun we have had in the last five years. I also extend my thanks to friends at Tokyo Tech and from Vietnam.

Finally, I must express my profound gratitude to my parents, my husband, and my sisters for providing me with unfailing support and continuous encouragement throughout five years of study and writing this thesis.

#### **ABSTRACT**

Recently, the infrared (IR) region ( $\lambda = 2.5$  to 25  $\mu$ m) has been essential in science and technology fields for two reasons. (1) It is referred to as the fingerprint region, where the presence of these molecules can be detected via their unique spectral signatures; thus, it is essential for analyzing materials and sensing applications. (2) It covers the thermal radiation spectrum of most objects and the atmospheric transmittance window (ATW). Thus, the investigation of the IR region is vital to investigating modern cooling technologies such as radiative cooling (RC). Based on this knowledge, the objective of our study is to investigate the optical and thermal radiation from polymer films and silica particles in the IR region.

This study investigated the optical properties through the surface phonon polaritons resonance (SPhPR) of silica microspheres for RC application. The SPhPR were observed at 9 and 21  $\mu$ m, which was confirmed by the Mie theory. Because of silica's intrinsic properties, gold-capped microspheres were applied with the expectation that gold could act as the antenna for excited SPhPR in the longer wavelengths. Although SPhPR was not excited as expected, the extraordinary transmittance (EOT) phenomenon through gold-capped microspheres was explored. The EOT is well known in the visible region, while that in the IR region has not been reported yet. The observed transmittance is greater than that of the flat gold film, although the surface of the gold-capped microsphere appears as wholly covered with the gold film. The finite-difference time-domain (FDTD) calculation indicates that light passes through the openings between the gold film on the substrate surface and the gold cap. The EOT occurs in the broadband, free from resonance, and is absent in the visible and near IR region, where gold does not function as an ideal metal.

Next, the thermal radiation property was explored through the RC characterization of polymer materials. The RC technology can cool things with no electricity; thus, it has been applied to various fields, such as clothing, energy harvesting, and solar cells. Furthermore, the outstanding property of polymers is able to use in flexible forms such as films or paint;

that polyester polymers and lumiflon are good candidates for daytime RC materials. They are transparent in the visible region while significantly emitted in the ATW; thus, they can provide high RC performance. In addition, our reported materials have paintability and weather-ability; therefore, they can apply in the larger area with long-term use. Finally, the RC efficiency of samples was compared with some reported materials such as polydimethylsiloxane (PDMS), soda-lime glass (glass), and silica particles on the glass.

On the other hand, RC materials also bring some adverse in daily life, such as frost on the car windshield or condensation on the window. To our knowledge, no non-RC materials have been reported yet. Some transparent non-RC materials were found to block unwilling thermal radiation. The non-RC performance was evaluated for the indium tin oxide (ITO) and dielectric-metal-dielectric (DMD) materials. However, they have some challenges like high fabrication costs and enlargement difficulties. Thus, the silver nanowire-mesh (Ag-NWs) film was considered to be another candidate because of its low cost and paintability.

#### TABLE OF CONTENTS

Acknov	vledgme	ents iv
Abstrac	et	
Abbrev	iations	
List of	<b>Fables</b>	
List of l	Figures	xv
Chapte	r 1: IN	<b>ΓRODUCTION</b>
1.1	Infrare	ed region
1.2	Surfac	e phonon polaritons
1.3	Extrao	rdinary transmission
	1.3.1	Background
	1.3.2	Principle
	1.3.3	Application
1.4	Radiat	ive cooling
	1.4.1	Background
	1.4.2	Principle
	1.4.3	Application of daytime-RC materials

	1.4.4	Application of non-RC materials	10
1.5	Outloo	ok of the thesis	11
Chapte	r 2: AN	ALYSIS METHOD	12
2.1	Optica	l property	12
	2.1.1	Surface phonon polaritons	12
	2.1.2	Extraordinary transmission	13
2.2	Radiat	ive cooling efficiency	15
	2.2.1	In-house measurement	15
	2.2.2	Field measurement	17
Chapte	r 3: OP	TICAL PROPERTIES OF SILICA PARTICLES	20
3.1	Backg	round	20
3.2	Experi	mental method	21
	3.2.1	Samples for SPhP measurements	21
	3.2.2	Samples for EOT measurements	21
	3.2.3	Measurement	23
3.3	Result	s of SPhP	23
3.4	Experi	mental results of EOT	27
	3.4.1	$SiO_2$ , and $Au$ - $SiO_2$ -microsphere monolayers	27
	3.4.2	Coverage dependence	28
	3.4.3	Size dependence	30
	3.4.4	Material independence	31
3.5	Calcul	ated results of EOT	32

	3.5.1	$SiO_2$ , and $Au$ - $SiO_2$ -microsphere monolayers	32
	3.5.2	Coverage dependence	33
	3.5.3	Gap between microspheres	34
	3.5.4	Size dependence	36
	3.5.5	Gold thickness dependence	37
	3.5.6	Material independence	38
	3.5.7	Electric distribution	39
3.6	CONC	CLUSION	40
Chapte		ANSPARENT MATERIALS FOR DAYTIME-RADIATIVE COOL	
4.1	BACK	GROUND	43
4.2	EXPE	RIMENT	43
	4.2.1	Polyesters samples	43
	4.2.2	Lumiflon samples	44
	4.2.3	Reference samples	47
	4.2.4	Material characterization	47
	4.2.5	In-house setup for temperature measurement	48
	4.2.6	Field setup for temperature measurement	49
4.3	RESU	LTS OF POLYESTER	50
	4.3.1	Optical property	50
	4.3.2	In-house RC measurement	51
4.4	RESU	LTS OF LUMIFLON	54
	441	Ontical property	54

	4.4.2	In-house RC measurements	57
	4.4.3	Field RC measurements	59
4.5	CONC	CLUSION	64
Chapte	r 5: TR	ANSPARENT NON-RADIATIVE COOLING MATERIALS	66
5.1	BACK	GROUND	66
5.2	EXPE	RIMENT	66
	5.2.1	Non-RC materials	66
	5.2.2	Material characterization	67
	5.2.3	In-house temperature measurement	68
	5.2.4	Field temperature measurement	68
5.3	RESU	LTS AND DISCUSSION	69
	5.3.1	Results of ITO and DMD films	69
	5.3.2	Results of the AgNWs mesh film	74
	5.3.3	Comparison of various samples	77
5.4	CONC	CLUSION	79
Chapter 6: CONCLUSION		80	
Chapte	r A: Vie	w factor	82
Chapte	r B: He	at conduction in the sample	84
Chapte	r C: Est	imate the thicknesses of LF films	85
Chante	r D: On	tical properties of PE films	87

Chapter E: Research achievements				
E.1	Publication list	88		
E.2	Conferences attended	88		
Referen	ces	99		

#### **ABBREVIATIONS**

2DHA Two-dimensional hole arrays

AgNWs Silver nanowires

ATW Atmospheric transparency window

Au-PS Gold-capped polystyrene

Au-SiO<sub>2</sub> Gold-capped silica

AZO Aluminum-doped Zinc oxide

BB Blackbody

DMD Dielectric-metal-dielectric
EOT Extraordinary transmission
FDTD Finite difference time domain

FTIR Fourier transmission infrared spectrometer

Glass Soda-lime glass

IR Infrared

ITO Indium tin oxide
LF LUMIFLON
LN Liquid nitrogen

Particles/glass Silica particles on the soda-lime glass plate

PDMS Polydimethylsiloxane

PE Polyethylene

PEN Polyethylene naphthalate
PET Polyethylene terephthalate

PS Polystyrene

RC Radiative cooling

SEM Scanning electron microscopy

SPhPR Surface phonon polaritons resonance

SPP Surface plasmon polaritons

#### LIST OF TABLES

4.1	Summary of optical properties of polyester polymers, and reported daytime RC materials. Averaged transmittance in the visible region, ( $\lambda$ = 0.4-0.75 $\mu$ m), and averaged emissivity in the ATW region, ( $\lambda$ = 8-13 $\mu$ m)	51
4.2	Temperature reduction of a 250 $\mu$ m-thick PET film at different distance between the sample and LN, $d$ , measured and calculated, in the in-house measurement	53
4.3	Temperature reduction of a 250 $\mu$ m-thick PEN film at different distance between the sample and LN, $d$ , measured and calculated, in the in-house measurement	53
4.4	The temperature drop ( $\Delta T$ ) of various materials with error bar at $d$ = 16 cm.	53
4.5	The temperature drop $(\Delta T)$ at different distance between the sample and LN, $d$ , measured and calculated results, in the in-house measurements	58
4.6	The temperature reduction $\Delta T$ , at the different thicknesses of the LF film, measured and calculated results, in the in-house RC measurement at distance $d=16$ cm	59
4.7	The temperature reduction, $\Delta T$ , of various samples, including: LF, PDMS, PE, glass, particles/glass, measured and calculated results, in the in-house RC measurement at distance $d=16$ cm	60
4.8	The temperature reduction $\Delta T$ (°C), under the sunlight of the Ag film, the LF film on the Ag substrate, the LF film on the glass substrate, and glass substrate in the sun. The calculated temperature drop is also listed	60
4.9	The temperature reduction $\Delta T$ (°C), in the shade of the Ag film, the LF film on the Ag substrate, the LF film on the glass substrate, and the glass substrate. The calculated temperature drop is also listed	60

4.10	The temperature reduction $\Delta T$ (°C), under the sunlight of the Ag film, the glass substrate, the LF film on the Ag substrate with thicknesses of 50 and 200 $\mu$ m. The calculated temperature drop is also listed	64
4.11	The temperature reduction $\Delta T$ (°C), in the shade of the Ag film, the glass substrate, the LF film on the Ag substrate with thicknesses of 50 and 200 $\mu$ m. The calculated temperature drop is also listed	64
5.1	Temperature reduction of a 300 nm thick-ITO film at different distance between samples and the LN, $d$ , measured and calculated, in the in-house measurement	73
5.2	Temperature reduction of a DMD film at different distance between samples and the LN, $d$ , measured and calculated, in the in-house measurement.	73
5.3	Temperature reduction of the ITO film with different thicknesses , at $d=16$ cm, measured and calculated, in the in-house measurement	73
5.4	Measured and calculated results, $\Delta T$ , of AgNWs-28 times at different distances between the sample and LN, $d$ , in the in-house measurement	77
5.5	Summary of difference temperature of samples and the ambient air inside the chamber, $\Delta T$ (°C), measured by the field experiments. The average temperature was estimated by using the last 20 min of the first and second measurement of opening the shutter	79
A.1	View factors $F_{s \to LN}$ calculated for the present geometry at various distance,	82

#### LIST OF FIGURES

1.1	The spectral range for IR region showing wavelengths (nm/ $\mu$ m) and wavenumbers (cm <sup>-1</sup> ). Cite [2]	1
1.2	Permittivity of $SiO_2$	2
1.3	Configuration of the EOT phenomenon	3
1.4	Biosensor based on the EOT phenomenon [17]	5
1.5	(a) Solar irradiance with an air mass coefficient of 1.5 and atmospheric transmission are shown in the blue and orange lines, and (b) Emissivity spectra of a daytime RC, a non-RC are presented in the green and red lines. The blackbody irradiance at 300 K is plotted in the black line	7
1.6	(a) Condensation on the window, (b) Frost on the car windshield	10
2.1	Model of a spherical particles with the radius, $r$ , and the dielectric constant, $\epsilon_1$	12
2.2	Schematic illustration of (a) side view, and (b) top view of Au- microspheres.	14
2.3	Diagrams of heat for (a) in-house RC measurement, and (b) field RC measurement	15
3.1	Fabrication process of a $SiO_2$ microsphere monolayer	22
3.2	Absorption cross-section of $SiO_2$ microspheres based on the Mie theory. Noted that results of $\phi$ = 5 and 20 $\mu$ m were multiplied by 0.1 and 0.02, respectively	24
3.3	Images of SiO <sub>2</sub> particles on the glass substrate: (a) $\phi = 1 \mu m$ , (b) $\phi = 5 \mu m$ , (c) $\phi = 20 \mu m$	24

3.4	Reflectivity and emissivity of $SiO_2$ spheres on the glass substrate. The hatched areas indicate the ATW. The dashed line is measured reflectance, $R$ . The solid line is estimated emissivity, $E = 1 - R$ , when assuming $T = 0$ .	25
3.5	SEM images of (a) $SiO_2$ , and (b) $Au$ - $SiO_2$ -microsphere monolayers	27
3.6	Transmittance spectra of a 25 nm-thick Au film, SiO <sub>2</sub> , and Au-SiO <sub>2</sub> -microsphe monolayers	re 27
3.7	SEM images of the Au-SiO <sub>2</sub> microsphere monolayers	28
3.8	(a) Transmittance spectra of the Au-SiO <sub>2</sub> -microsphere monolayers with different coverages, $\sigma$ , and (b) their transmittance spectra normalized by the coverages	29
3.9	SEM images of the $Au$ - $SiO_2$ microsphere monolayers of different microsphere diameters	30
3.10	(a) Transmittance spectra of the Au-SiO <sub>2</sub> -microsphere monolayers with different diameter, $\phi$ , and (b) their transmittance spectra normalized by the coverages	30
3.11	SEM images of the Au-PS microsphere monolayers	31
3.12	(a) Transmittance spectra of the Au-PS-microsphere monolayers with different coverage, $\sigma$ , and (b) their transmittance spectra normalized by the coverage	31
3.13	Calculated transmittance spectra of the $SiO_2$ , and $Au$ - $SiO_2$ -microsphere monolayers 1 $\mu$ m in diameter	32
3.14	Calculated transmittance spectra of the Au-SiO $_2$ with various inter-particle distances, and (b) their transmittance spectra normalized by the coverage, $\sigma$ .	33
3.15	Calculated and measured transmittance at a wavelength of 16 $\mu$ m, $T$ , as a function of coverage $\sigma$ and the gap distance	34
3.16	(a) Schematic drawing of Model 1, where the microsphere are attached ( $g = 0$ ). Model 1b is Model 1a without the microspheres. (b) Transmittance spectra of Models 1(a) and 1(b). (c) Schematic drawing of Model 2, where the microspheres are separated with a gap of 0.05 $\mu$ m. Model 2b is Model 2a without the microspheres. (d) Transmittance spectra of Model 2(a) and 2(b)	35

3.17	Calculated transmittance spectra of the Au-SiO <sub>2</sub> -microsphere monolayers with various size $\phi = 0.3$ , 1, 3 $\mu$ m and (b) their transmittance spectra normalized by the coverage, $\sigma$	36
3.18	Calculated transmittance spectra of the Au-SiO $_2$ with 1 $\mu$ m in diameter, and difference gold thickness	37
3.19	Calculated transmittance spectra of the Au-SiO <sub>2</sub> , and Au-PS-microsphere monolayers 1 $\mu$ m in diameter	38
3.20	(a) Electric field distribution profile of the Au-SiO $_2$ microsphere monolayer forming a square lattice, where the microspheres are attached ( $g=0~\mu m$ ), and excited by light at a wavelength of 16 $\mu m$ . Both electric field distributions in the cut plane including AB and CD are illustrated. The white parts at the boundaries A and B represent the electric field grater than 6 (indicated by arrows). (b) Electric field distributions in the cut plane including AB, where the spheres are separated with gaps ( $g=0.05~\mu m$ )	39
3.21	(a) Electric field distribution profiles of the Au-SiO <sub>2</sub> microsphere monolayer forming a square lattice (a) and a hexagonal lattice (b), where the microspheres are attached ( $g = 0 \mu m$ ), and excited by light at a wavelength of 16 $\mu m$ . Both electric field distributions in the cut plane at $z = 0$ , at the substrate surface.	41
4.1	Image of (a) 250 $\mu$ m-thick PET, and (b) 250 $\mu$ m-thick PEN films	44
4.2	Chemical structures of (a) PET, and (b) PEN films	44
4.3	Chemical structure of LF [95]	45
4.4	Photo images of (a) LF powder, and (b) LF solution after toluene dissolution.	45
4.5	Substrates were used in this study are (a) silicon, (b) glass, (c) glass coated on both sides by a 100 nm-thick gold film, and (d) glass coated by a 100 nm-thick silver film	46
4.6	(a) Schematic for in-house measurement, (b) and (c) Images of a chamber and the sample's holder, respectively	48
4.7	(a) Schematic for field temperature measurement, (b) Photograph of the chamber and samples	49
4.8	Visible transmittance spectra of the samples: PDMS, PET, PEN films, and the glass plate. The thickness is given in parentheses.	50

4.9	Emissivity spectra of the samples: films of PDMS, PET, and PEN; glass plate; and the blackbody radiation spectrum at 300 K. The hatched areas indicate the ATW	52
4.10	Measured temperature between ambient air and (a) 250 $\mu$ m-thick PET, (b) 250 $\mu$ m-thick PEN films	52
4.11	Transmittance of LF films on the glass substrate and the solar irradiance. The thicknesses of the film are 50 $\mu$ m and 200 $\mu$ m. Note that the solar irradiance is multiplied by 5 x 10 <sup>-4</sup>	54
4.12	Emissivity spectra of LF films with thicknesses of 4, 12, 25, 50, 100 and 200 $\mu$ m in the IR wavelength range (2.5-25 $\mu$ m). Numbers in parentheses indicate film thickness. The hatched areas indicate the ATW	55
4.13	Emissivity spectra of various samples in the IR wavelength range (2.5-25 $\mu$ m), including a 350 $\mu$ m-thick PDMS, a 50 $\mu$ m-thick LF, a 400 $\mu$ m-thick PE, a 1 mm-thick glass, 20 $\mu$ m-diameter SiO <sub>2</sub> particles on the glass. Numbers in parentheses indicate film thickness. The hatched areas indicate the ATW	56
4.14	Measured temperature of ambient, a glass coated both sides by 100 nm-thick gold films (substrate), and a 50 $\mu$ m-thick LF film. The shutter opened at 30 min, and the gap between the sample and the LN were changed to 23, 19, 16 cm, in order	57
4.15	Measured temperature reduction by the in-house experiments, as the function of thickness of LF and PE films. The distance of samples and the LN is fixed at $d = 16$ cm. The dashed line is a guide to eyes	58
	Daytime RC results (a) in the sun and (b) in the shade. The shutter opened from 30 min to 210 min. Samples are 100 nm-thick Ag film, 1 mm-thick glass substrate, 50 $\mu$ m-thick LF film on a glass and 50 $\mu$ m-thick LF film on Ag substrate. Temperature of ambient both inside and outside the chamber was recorded	61
4.17	(a) Daytime RC results in the sun and (b) RC results in the shade. The shutter opened at 30 min and 120 min. Samples are the 100 nm-thick Ag film, the 1 mm-thick glass substrate, the 50 $\mu$ m-thick LF film on a Ag substrate and a 200 $\mu$ m-thick LF film on a Ag. Temperature of ambient both inside and outside the chamber was recorded. The number indicate	
	the film thickness in $\mu$ m	63
5.1	Schematic structure of (a) ITO, and (b) DMD films on the glass substrate.	66

5.2	Fabrication process of the AgNWs film on the glass substrate	67
5.3	(a) Schematic of the field setup, images of (b) a chamber, and (c) samples inside a chamber	68
5.4	Transmittance of ITO films with thicknesses of 20, 50, 150 and 300 nm in the visible wavelength range ( $\lambda$ = 0.4-0.75 $\mu$ m). Numbers in parentheses indicate film thickness	69
5.5	Reflectance of ITO films with thicknesses of 20, 50, 150 and 300 nm in the IR wavelength range (2.5-25 $\mu$ m). Numbers in parentheses indicate film thickness	70
5.6	Transmittance of different samples in the visible region: a 300 nm-thick ITO, DMD films, and a 1 mm-thick glass	71
5.7	Reflectance of different samples in the IR region: a 300 nm-thick ITO, DMD films, and a 1 mm-thick glass	71
5.8	Measured temperature between ambient air, glass and (a) a 300 nm-thick ITO, (b) DMD films	72
5.9	Optical microscope images with the magnification of 60 times of the Ag- NWs mesh film on a glass, (a) 3 times, (b) 14 times and (c) 28 times of spin-coating process repetitions	74
5.10	Transmittance of AgNWs films on the glass substrate. The result of the glass presents as the reference. The numbers in the parenthesis indicate the number of spin coating repetition.	75
5.11	Reflectance of AgNWs films on the glass substrate. The result of the glass presents as the reference. The numbers in the parenthesis indicate the number of spin coating repetitions. The black line indicates the blackbody radiation at 300 K. The hatched areas indicate the ATW	76
5.12	Measured field temperature of samples: a 300 nm-thick ITO, DMD, and AgNWs with the spin coating repetition of 28 times and glass substrate. The ambient air both inside and outside the chamber was also measured	77
A.1	Geometry for the calculation of the view factors	82
C.1	The cross-sectional SEM images of LF films with different thicknesses ( $t$ : $\mu$ m) (a) $t = 25$ (b) $t = 50$ (c) $t = 100$ (d) $t = 200$	85

C.2	The reflectance spectrum of LF on the Au substrate in the visible region.  The number indicated the estimated thickness	86
D.1	Emissivity spectra of PE films with thicknesses of 25, 125, 275, and 400 $\mu$ m in the IR wavelength range (2.5 - 25 $\mu$ m). Numbers in parentheses indicate film thickness. The hatched area indicates the ATW	87

#### **CHAPTER 1**

#### INTRODUCTION

#### 1.1 Infrared region

Infrared (IR) is the electromagnetic radiation, including wavelengths from 0.8 to 500  $\mu$ m [1]. Figure 1.1 presents three different bands of IR region: near-IR,  $\lambda = 0.8$  - 2.5  $\mu$ m, mid-IR,  $\lambda = 2.5$  - 25  $\mu$ m and far-IR,  $\lambda = 25$  - 500  $\mu$ m [2]. Especially, the IR region is essential in science and technology fields because of two below reasons.

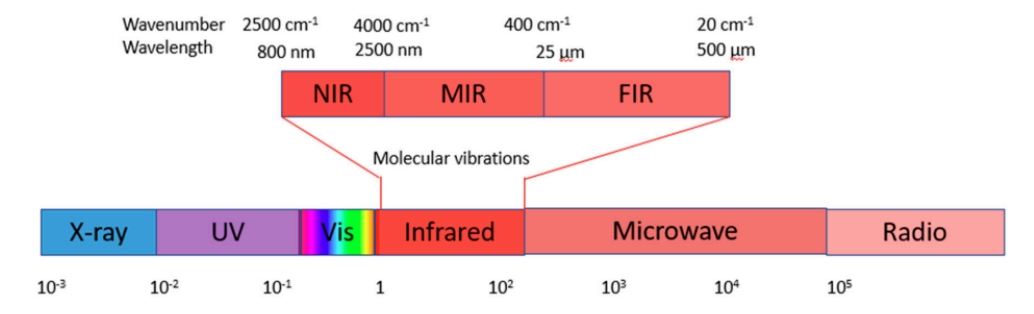


Figure 1.1: The spectral range for IR region showing wavelengths (nm/  $\mu$ m) and wavenumbers (cm<sup>-1</sup>). Cite [2]

Firstly, the IR band at wavelengths  $\lambda = 6.6$  - 25  $\mu$ m includes the fingerprint region, which contains a very complicated series of absorption. The absorption corresponds to bending molecular vibration such as N-H, O-H, C-H, C=O, C=N, C=C, C $\equiv$ C, and C $\equiv$ N bendings. In this region, even a small difference in the structure produces a change in absorption peaks. Thus, the fingerprint region is unique and essential for analyzing materials [3], and sensing applications [4, 5].

Secondly, the IR covers thermal emission peaks of most objects with temperatures ranging from 200 - 1400 K. In addition, the IR range covers the atmospheric transparency window (ATW) ( $\lambda$  = 8 to 13  $\mu$ m, and 16 to 25  $\mu$ m). Thus, the IR region is vital for investigating modern cooling technologies such as radiative cooling (RC).

#### 1.2 Surface phonon polaritons

The surface phonon polaritons (SPhP) phenomenon is the interaction of the electromagnetic field and the lattice vibration in the dielectric material. SPhP resonance can be excited only when the negative real part of permittivity is observed within the Reststrahlen band [6]. Similar to the condition of exciting surface plasmon polariton, SPhP in the particles can only be excited when the polarizability is enhanced. The polarization,  $\alpha$ , is defined as the degree of polarization of particles when an electric field is applied. It is shown in the equation:

$$\alpha = 4\pi r^3 \frac{\epsilon_1 - \epsilon_2}{\epsilon_1 + 2\epsilon_2},\tag{1.1}$$

where r,  $\epsilon_1$ ,  $\epsilon_2$  are the radius of a sphere, permittivity of material, and permittivity of medium, respectively.

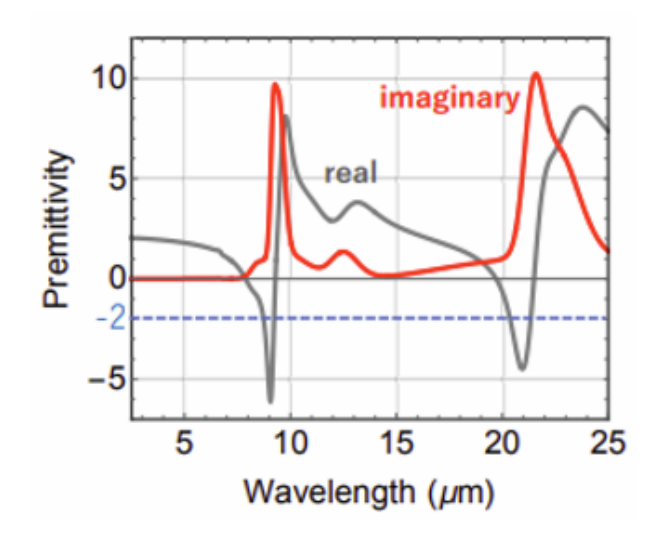


Figure 1.2: Permittivity of SiO<sub>2</sub>.

Figure 1.2 presents the real and imaginary permittivity of SiO<sub>2</sub>. The surrounding ambient is air,  $\epsilon_2 = 1$ . Under the quasi-static approximation, the polarizability is enhanced when  $\epsilon_1 + 2$   $\epsilon_2 = 0$ . Thus, the SPhP resonance could be observed at the wavelength of 9 and 21  $\mu$ m. The absorption peak coincides with the ATW; thus, SiO<sub>2</sub> particles promise high RC performance.

#### 1.3 Extraordinary transmission

#### 1.3.1 Background

The extraordinary transmission (EOT) is a phenomenon in which the transmission of the electromagnetic field is higher than that expected from small holes or gap areas in the metallic film [7, 8]. The unusual optical transmission was observed by Ebbensen et al. in 1998 [9]. EOT has attracted significant attention to exploring the transmission mechanism and application for chemical sensors, and biosensors [10]. Although these studies are carried out for visible and near-IR light, the EOT in the IR range remains unclear. To the knowledge, only one paper has reported EOT using periodically perforated silicon-dioxide film at the IR wavelength [7]. However, the EOT of the metal-capped microspheres in the IR region has not been reported yet.

#### 1.3.2 Principle

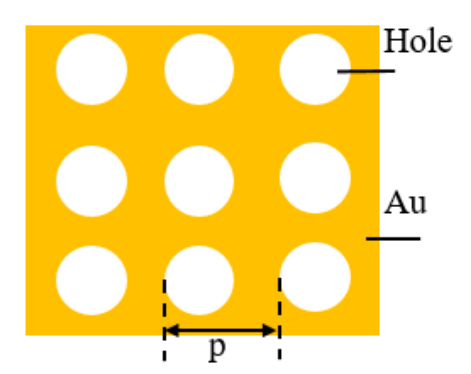


Figure 1.3: Configuration of the EOT phenomenon

In this section, the principle of the normal EOT phenomenon will be explained. Figure 1.3 presents a metal film with perforated holes, periodically distributed with a constant lattice p. In general, different types of EOT can be found when the holes are isolated, randomly distributed, or periodically arranged [10]. The various physical mechanisms are responsible for surface-enhanced EOT, localized EOT, absorption-induced transparency, and Brewster angle EOT [10].

Firstly, the surface-enhanced EOT is based on the excitation of a surface plasmon at the front and rear metallic interfaces. It was discovered for the square arrays of holes. The surface mode enhanced the evanescent field at the spot and thus contributes to the light through the hole array [11].

Secondly, the localized EOT was discovered in both isolated and random arrays of holes. The transmittance depends on the hole geometry and material characteristics. The spots with a high aspect ratio in the geometric length scales support localized electromagnetic fields that can enhance transmission [12, 13].

Thirdly, absorption-induced transparency was observed in a perforated metal film due to the dependence of surface-enhanced EOT on the lattice constant. It occurs close to a sharp absorption band where the real part of the dielectric constant is large while the imaginary part is small [14, 15].

Fourth, the Brewster angle EOT occurs at the grazing angle of incidence when the impedance matches the incoming wave, thus increasing the transmission. The restriction of this type of EOT is that the hole sizes must be smaller than the period and the wavelength [16].

#### 1.3.3 Application

EOT is also used for the sensing application. Figure 1.4 presents the experimental set-up and SEM image of two-dimensional hole arrays (2DHA) sensor chip [17]. The advantage of using a 2DHA chip is that the setup does not need to use any prism, reducing the detector's size. Moreover, the 2DHA sensor chip features strongly depend on the dielectric constant of the surrounding medium; thus, the small change of dielectric constant in a liquid cell can modify the scattered field intensities and the resonance position. Such kind of change can be estimated through the measured EOT spectra.

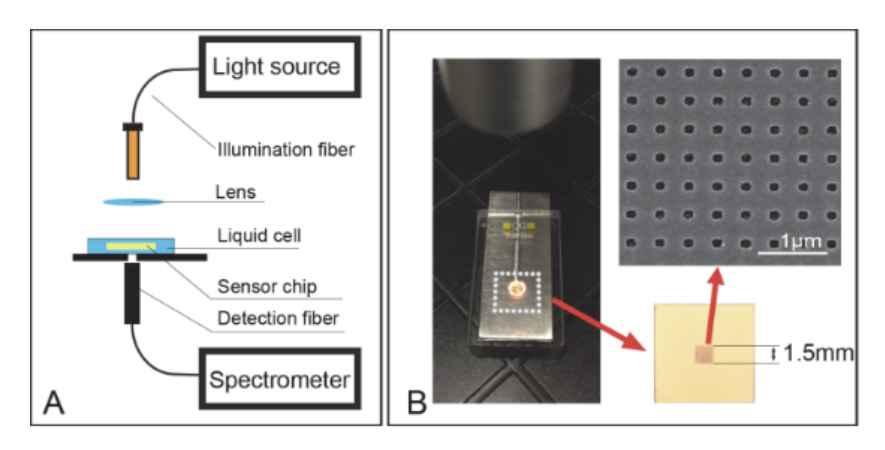


Figure 1.4: Biosensor based on the EOT phenomenon [17].

#### 1.4 Radiative cooling

#### 1.4.1 Background

RC is a purely passive cooling method that can save energy and reduce emissions by dissipating heat into the universe through the ATW [18, 19]. Even with the uncomplicated RC structures, the cooling power of 100 W/m<sup>2</sup> can be achieved on clear days [20, 21]. With the progress of industrial development and economic growth, we consume substantial amounts of electricity and generate a large quantity of CO<sub>2</sub>. Moreover, cooling is critical to human life, especially in hot countries. In contrast, traditional cooling technologies such as air conditioner is warming the environment. Thus, the renewable cooling way has a significant impact on energy sustainability [22, 23]. Nighttime RC materials and their applications were demonstrated [24, 25], while the peak cooling demand occurs during the daytime. Therefore, many researchers have investigated daytime RC materials with different structures, such as lattice structure [26], and conical shape array [27]. Even they present high RC efficiency while do not promise real applications because of high fabrication costs and the problem with large areas [28, 29, 30]. Therefore, many polymers with simple structures and high RC efficiency were reported, such as polydimethylsiloxane (PDMS) [31], polytetrafluoroethylene (PTFE) [32], and polymethyl methacrylate (PMMA) [33]. The advantages of polymers are low fabrication costs and being able to use them in flexible forms.

Thus, in this study, polymers were also considered as candidates for daytime RC materials.

RC materials promise many applications, such as cool SCs and buildings without power input. However, they also bring adverse effects, such as frost on car windshields and condensation on windows. Therefore, non-RC materials are essential as RC materials. To the knowledge, no non-RC materials have been reported yet.

#### 1.4.2 Principle

To explore the principle of the RC, the heat transfer method will be explained. Heat transfer is how the energy flows in heat from hotter to colder objects. The heat can be transferred in three ways: by conduction, convection, and radiation [34].

Conduction is the transfer of heat by direct contact between bodies or through the same body [35]. Materials such as gold, silver, or copper have high thermal conductivity and conduct heat well. In contrast, materials such as glass or wood have lower conductivity [36, 37].

Convection is the transfer of heat via the interchange of hot and cold molecules with a fluid or gas moving at a different temperature [38]. Two main types of convection heat transfer are natural convection and forced convection. Natural convection occurs due to the variation of temperature between two points. Forced convection is due to external factors such as the pump and fan.

Radiation is the heat transfer via electromagnetic radiation, known as thermal radiation. In contrast to the heat transfer by conduction and convection, it occurs even in a vacuum without any medium. The heat transfer via radiation occurs at the speed of light. An example of radiation heat transfer is solar radiation.

Three following laws are associated with thermal radiation heat transfer. Firstly, the Stefan–Boltzmann law describes the radiant intensity and estimates by:

$$Q = \epsilon \sigma T^4, \tag{1.2}$$

where  $\sigma = 5.67 \text{ x } 10^{-8} \text{ W/m}^2\text{K}^4$ , is called the Stefan–Boltzmann constant.  $\epsilon$  is emissivity of the object, which plays an important role in the radiation heat transfer, and T is temperature. Secondly, Kirchhoff's law of thermal radiation, the object's absorption equals its emission. Thirdly, Plank's law describes the blackbody radiation spectrum, which depends only on the object's temperature. The blackbody is the ideal physical object, which can absorb and emit 100% of thermal radiation. Figure 1.5(b), the blackbody radiation at 300 K is presented.

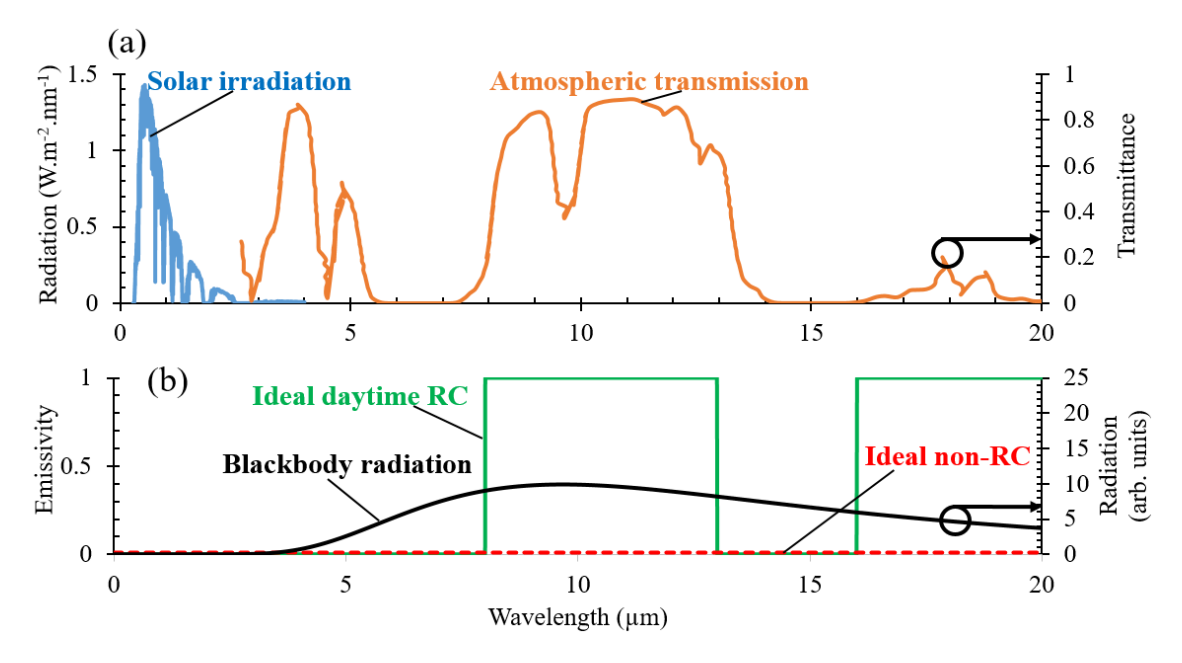


Figure 1.5: (a) Solar irradiance with an air mass coefficient of 1.5 and atmospheric transmission are shown in the blue and orange lines, and (b) Emissivity spectra of a daytime RC, a non-RC are presented in the green and red lines. The blackbody irradiance at 300 K is plotted in the black line.

The stable temperature of the Earth is based on the RC principle. In detail, the Earth absorbed the solar irradiation and raised its temperature. Then the portion of absorbed heat dissipates to the cold universe (at 3 K) in the form of thermal radiation via the ATW. Therefore, in the daytime, the Earth has a surface temperature of near 300 K. In the nighttime, the absorption of sunlight is absent, and the Earth's surface loses heat to the universe. The temperature at night is low as a result [39].

The Earth's atmosphere exits between the Earth surface and the universe [40, 41]. As

radiation occurs though atmosphere, it is affected by multiple factors, including humidity [42], geographical location [43], and cloud coverage [44]. However, Figure 1.5(a) indicates that atmosphere is transparent for thermal radiation at 8-13  $\mu$ m, and 16-25  $\mu$ m [45, 46]. Especially, the ATW coincides with the peak emission of blackbody at 300 K (Figure 1.5(b)) [44]. Thus, the RC technology allows to cool the sky-faced objects.

The basic principle of the passive daytime RC materials is that the absorbed heat energy is lower than emitted heat energy under the direct sunlight [29]. The ideal emissivity of daytime RC materials is presented in Figure 1.5(b). It has three characteristics: (1) 100% of light is transmittance (zero emittance) in the visible region to minimize the solar power absorption; (2) 100% of light is emitted in the ATW to maximize radiated power. It means that no light transmits and reflects; (3) no emitted light where the atmosphere is opaque to minimize the absorbed power due to atmospheric thermal radiation [47].

The principle of non-RC materials is minimum heat dissipation to the universe in the nighttime when the absorbed sunlight is zero. The ideal non-RC materials need to satisfy two conditions: (1) 100% of light is transmittance (zero emittance) in the visible region to avoid heating up under the sunlight, and (2) 100% of light is reflectance (low emittance) in the IR region, especially in the ATW to avoid heat loss to the universe. The emissivity of the ideal non-RC materials presents in Figure 1.5(b).

#### 1.4.3 Application of daytime-RC materials

Daytime RC application has attracted interest in recent years. It has been demonstrated for cooling objects such as buildings and SCs [48]. Moreover, this technology can combine with other technology to generate power and harvest freshwater.

Firstly, the application of daytime RC in building cooling will be explained. Nearly 20% of world energy consumption is used in building cooling using the air conditioner and electric fans. Furthermore, this trend is predicted to triple by 2050 and becomes more desired in the hot country [49, 50]. Daytime RC materials in building applications can

coat both roof and siding materials that need to be cooled [51, 52]. It emits the stored heat in opaque materials under sunlight and reflects/transmits off incoming solar radiation [53, 54]. However, heat loss due to RC should be considered in the cold region when designing RC materials [55, 56].

Secondly, daytime RC materials are applied to cool SCs. In principle, the daytime RC materials can be applied to reduce the operating temperature while maintaining the solar absorption of SCs [57]. The SCs absorbed the sunlight; there is a portion of absorbed solar radiance that does not convert into electricity and generates heat [58]. Thus, the operating temperature of SCs is typically 50-55 °C or higher [59, 60]. The high operating temperature adversely affects solar cells' efficiency and lifetimes. As previous published, the efficiency decreases 0.45% when the SCs temperature rises 1 °C [61]. For example, An et al. reported that the temperature of SCs with the radiative cooler was reduced by over 18.3 °C in comparison with bare SCs; as a result, the absolute power conversion efficiency can be increased by 0.45%. In another example, Wang et al. sand-witched the SCs between two glass plates [62]. The reduction temperature of SCs was 36 °C, leading to 31% increase of  $V_{\rm OC}$ . The lifetime of SCs is expected to expand from 4 to 15 times. From these examples, we can imagine the importance of daytime RC materials for SCs. Ideal films for cooling SCs are transparent over solar wavelengths ( $\lambda = 0.4$  - 2.5  $\mu$ m) but strongly emission in the ATW.

Thirdly, daytime RC materials have been applied to harvest freshwater. Clean water is a global challenge, especially in the region where water is abundant [63]. Thus, passive vapor condensation becomes essential. However, the traditional water harvest only works during nighttime by convection and conduction heat transfers. Thus, combining the traditional method and the novel- RC material to generate water in both daytime and nighttime has recently attracted attention [64, 65].

#### 1.4.4 Application of non-RC materials

Figure 1.6 presents images of condensation on windows and frost on the car windshield [66, 67]. Condensation is the transformation process of water vapor in the air to water. It happens when the moisture in the atmosphere comes in contact with a surface whose temperature is close to the dew points [68]. In addition, frost is the thin layer of ice and is the form of condensation. It occurs when the temperature of an object drops below the freezing point temperature. Both condensation and frost phenomena usually occur in the early morning of a clear winter's night. During the daytime, these phenomena do not appear because the absorption of solar radiation is dominant. However, during the nighttime, the temperature of an object is near the ambient air temperature, and the convective heat transfer does not work. Only radiative heat transfer can continue to dissipate heat and cool down the object's temperature. In addition, the glass has a high RC performance; thus, its heat losses to the universe. The condensation and frost on windows, car windshields were observed as the results [69]. The currently active frost removal methods are hot water, and mechanical, which lead to both time-consuming and costly [70, 71]. Thus, the passive prevention of condensation/frost by non-RC materials is highly desirable.

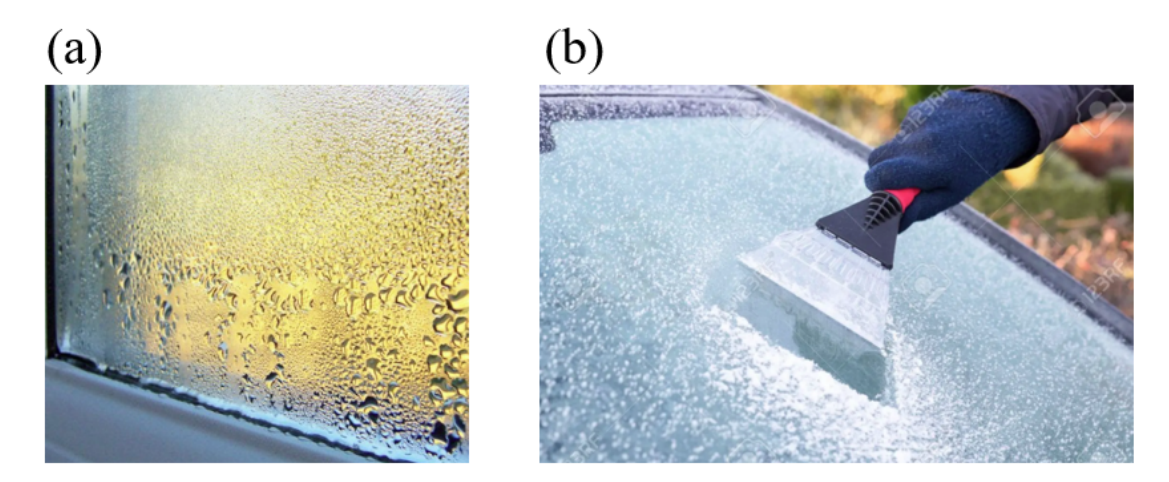


Figure 1.6: (a) Condensation on the window, (b) Frost on the car windshield.

#### 1.5 Outlook of the thesis

The IR region has been essential in science and technology to analyze materials, sensing applications, and passive RC technology. Based on this knowledge, this study aims at investigating the optical and thermal radiation properties of novel materials in the IR region.

Chapter 1 summarizes the background of the IR region, SPhP resonance, EOT, and RC technology.

Chapter 2 discusses the analysis method of optical and thermal radiation properties. Mie theory and FDTD are presented to investigate the optical property. The in-house and field RC calculations are carried out to investigate the thermal radiation. Dependence of total thermal radiation on experimental setups is included.

In chapter 3, the optical properties of SiO<sub>2</sub> particles are shown. The SPhP resonance of SiO<sub>2</sub> was explored, which coincided with the ATW. Thus, SiO<sub>2</sub> particles were used as the reference for RC materials. This section also presents the EOT phenomenon of gold-capped microspheres in the IR region. The mechanism and properties of the EOT are precise by both calculated and measured results.

In chapter 4, transparent materials for daytime RC are shown. The high RC efficiency of polyester polymers and fluoropolymers is demonstrated. Primarily, the in-house and field experimental setups were built up to measure RC efficiency. Next, samples were fabricated. Finally, the sample's optical properties and their RC efficiency were investigated. The RC efficiency was confirmed by calculated results.

In chapter 5, transparent non-RC materials for blocking unwilling thermal radiation are presented. The blocking thermal radiation of transparent electrodes such as indium tin oxide (ITO) and dielectric-metal-dielectric (DMD) films are shown. Silver-nanowires (AgNWs) mesh film is considered to be another candidate of non-RC materials for real applications.

In chapter 6, conclusions of this work are summarized.

#### **CHAPTER 2**

#### **ANALYSIS METHOD**

#### 2.1 Optical property

#### 2.1.1 Surface phonon polaritons

In 1908, Gustav Mie developed the theory to understand the color in absorption or scattering of small particles, called Mie theory. The attention point is that Mie theory's mathematics is extremely straightforward in understanding an interaction of electromagnetic field and the spheres. Figure 2.1 shows a model of a spherical particle, which has a dielectric constant and radius,  $\epsilon_1$  and r, respectively. The surrounding is the medium with a dielectric constant of  $\epsilon_2$ . The relative refractive index can be defined as  $m = \epsilon_1/\epsilon_2$ .

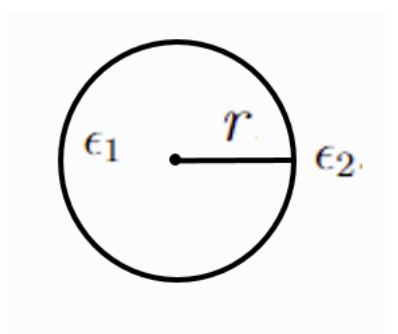


Figure 2.1: Model of a spherical particles with the radius, r, and the dielectric constant,  $\epsilon_1$ .

Firstly, coefficients of the field inside the particles are shown by  $c_n, d_n$ :

$$c_n = \frac{m\psi_n(x)\xi'_n(x) - m\xi_n(x)\psi'_n(x)}{\psi_n(mx)\xi'_n(x) - m\xi_n(x)\psi'_n(mx)}$$
(2.1)

$$d_n = \frac{m\psi_n(x)\xi'_n(x) - m\xi_n(x)\psi'_n(x)}{m\psi_n(mx)\xi'_n(x) - \xi_n(x)\psi'_n(mx)}$$
(2.2)

In view that the permeability of the particles and the surrounding medium is similar.

Then, the scattering coefficients are shown by  $a_n$  and  $b_n$ :

$$a_{n} = \frac{m\psi_{n}(mx)\psi'_{n}(x) - \psi_{n}(x)\psi'_{n}(mx)}{m\psi_{n}(mx)\xi'_{n}(x) - \xi_{n}(x)\psi'_{n}(mx)}$$
(2.3)

$$b_{n} = \frac{\psi_{n}(mx)\psi'_{n}(x) - m\psi_{n}(x)\psi'_{n}(mx)}{m\psi_{n}(mx)\xi'_{n}(x) - m\xi_{n}(x)\psi'_{n}(mx)}$$
(2.4)

where,  $\psi_n(r) = rj_n(r)$  and  $\xi_n(r) = r[j_n(r) + iy_n(r)]$ . The parameter x depends on the wavenumber x = k \* r.

 $j_n(r)$  and  $y_n(r)$  are the Riccati-Bessel function, which are:

$$j_n(r) = \sqrt{\frac{\pi}{2r}} J_{n+1/2}(r)$$
 (2.5)

$$y_n(r) = \sqrt{\frac{\pi}{2r}} Y_{n+1/2}(r)$$
 (2.6)

The scattering cross-section,  $C_{\rm sca}$ , and extinction cross-section,  $C_{\rm ext}$ , are:

$$C_{\text{sca}} = \frac{2\pi}{k^2} \sum_{n=1}^{\infty} [(2n+1)(|a_n|^2 + |b_n|^2)]$$
 (2.7)

$$C_{\text{ext}} = \frac{2\pi}{k^2} \sum_{n=1}^{\infty} [(2n+1)Re(a_n + b_n)]$$
 (2.8)

Then, absorption cross section,  $C_{\rm abs}$ , is:

$$C_{\rm abs} = C_{\rm ext} - C_{\rm sca} \tag{2.9}$$

All the basic equation is referenced from the book by Bohren and Huffman [72].

#### 2.1.2 Extraordinary transmission

The FDTD method is used to solve problems of electromagnetic, which seem to be simplest both conceptually and in terms of implementation. The simple idea of the FDTD method is to discrete in the time and the space, Maxwell's equations with central difference approximations, which was first proposed by Yee [73]. In this study, the FDTD software (Full WAVE, Synopsys Inc.) was used to explore the mechanism of the EOT.

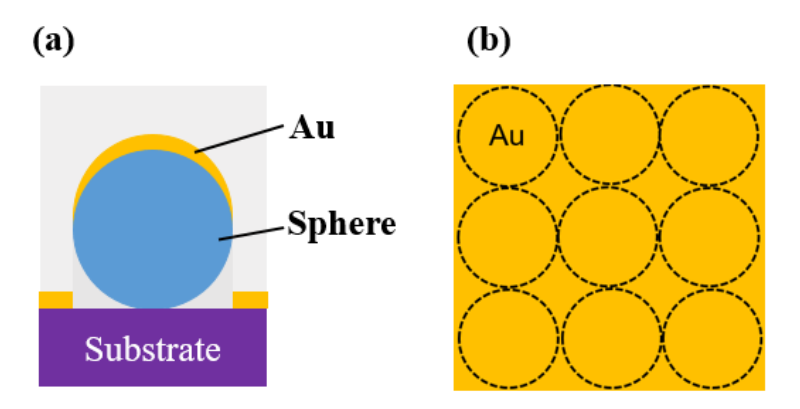


Figure 2.2: Schematic illustration of (a) side view, and (b) top view of Au- microspheres.

In the Au-capped microsphere structure, the thickness of a gold film was fixed at 25 nm, which is much smaller than the diameter of particles. Figure 2.2(a) presents the side view structure of the calculation model. The above half of the sphere was covered by the gold film while the bottom half of its remained without a film. Figure 2.2(b) shows the top view structure of a model. It seems that all surface of the microsphere seems to be fully covered by the gold film. The Yee mesh size in the x, y, and z-direction was 10  $\times$  10  $\times$  5 nm<sup>2</sup>. The periodic boundary condition was applied in the x and y-directions. Moreover, the perfectly-matched-layer condition was applied in the z-direction, where the z-direction is along the surface normal. The dielectric constant of SiO<sub>2</sub> was taken from the literature presented by Malitson [74], and Kitamura [75] to cover the wide wavelength range, from the ultraviolet to the IR region. The dielectric constant of PS is referenced from the literature [76, 77]. The dielectric constant of gold is cited from the literature presented by Olmon [78]. All the dielectric constants are installed in the FDTD software.

#### 2.2 Radiative cooling efficiency

#### 2.2.1 In-house measurement

An apparatus was developed to measure the dropped temperature of samples in-house environment. The Dewar glass was then filled with the LN (at 77K) in this test. Samples are separated from the LN with a distance of d. The experimental setup is presented in Figure 4.6. The diagram of the heat is presented in Figure 2.3(a).

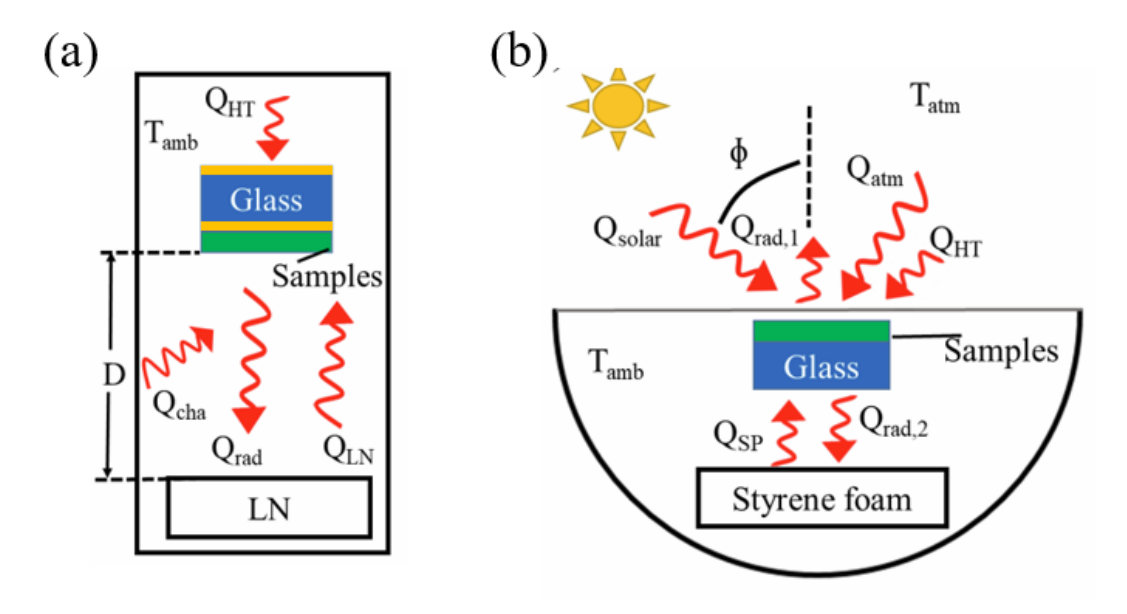


Figure 2.3: Diagrams of heat for (a) in-house RC measurement, and (b) field RC measurement.

The total heat of the sample,  $Q_{\text{total}}$ , is defined below:

$$Q_{\text{total}} = Q_{\text{rad}} - Q_{\text{cha}} - Q_{\text{LN}} - Q_{\text{HT}}. \tag{2.10}$$

 $Q_{\rm rad}$  is the thermal radiation emitted by the sample. It is

$$Q_{\rm rad} = \pi A_{\rm s} F_{\rm s \to LN} \int_0^\infty d\lambda I_{\rm BB}(T_{\rm s}, \lambda) \epsilon_{\rm s}(\lambda), \tag{2.11}$$

where,  $A_s$  and  $F_{s\to LN}$  are the area of the sample and the view factor from the sample to the LN (the value of the view factor is explained in the Appendix A);  $T_s$  is the temper-

ature of the sample;  $I_{\rm BB}$  is the spectral radiance of a blackbody at the temperature T,  $I_{\rm BB} = \frac{2h_{\rm p}c^2}{\lambda^5} \frac{1}{e^{h_{\rm p}c\lambda k_{\rm B}T}-1}$ ;  $h_{\rm p}$ , c,  $k_{\rm B}$ ,  $\lambda$  are the Planck constant, the vacuum velocity of light, Boltzmann constant, and wavelength, respectively.  $\epsilon_s(\lambda)$  is the spectral emissivity of the sample. Although  $\epsilon_s(\lambda)$  depends on the emission angle, the measured absorption spectra to the surface normal are used. Because the emission angle to the refrigerant is less than 25°, which can be regarded as surface normal within the error.

 $Q_{\rm cha}$  is the heat from the chamber surface. The inner surface of the chamber is Al foil. The emissivity of Al foil is 0.012, which is calculated from the refractive index of Al [79]. Therefore, the thermal view factor from the sample to the chamber surface is  $F_{\rm cha\to s}$ . Thus, the heat from the chamber is defined as:

$$Q_{\rm cha} = \pi A_{\rm cha} F_{\rm cha \to s} \int_0^\infty d\lambda I_{\rm BB}(T_{\rm amb}, \lambda) \epsilon_{\rm Al} \epsilon_{\rm s}(\lambda)$$
 (2.12)

Where,  $A_{\rm cha}$  and  $T_{\rm amb}$  are the chamber area and temperature of the ambient. Since only LN refrigerant and the chamber surface can be viewed from the samples,  $F_{\rm s\to LN} + F_{\rm s\to cha} = 1$ . Using the reciprocal theorem,  $A_{\rm s}F_{\rm s\to cha} = A_{\rm cha}F_{\rm cha\to s}$ . Then, the relation was estimated,  $F_{\rm cha\to s} = (A_{\rm s}/A_{\rm cha})(1-F_{\rm s\to LN})$ .  $Q_{\rm cha}$  equals:

$$Q_{\rm cha} = \pi A_{\rm s} (1 - F_{\rm s \to LN}) \int_0^\infty d\lambda I_{\rm BB}(T_{\rm amb}, \lambda) \epsilon_{\rm Al} \epsilon_{\rm s}(\lambda)$$
 (2.13)

 $Q_{\rm LN}$  is the heat from the LN, which is defined as:

$$Q_{\rm LN} = \pi A_{\rm s} \int_0^\infty d\lambda I_{\rm BB}(T_{\rm LN}, \lambda) \epsilon_{\rm LN} \epsilon_{\rm s}(\lambda)$$
 (2.14)

where,  $\epsilon_{\rm LN}$  and  $T_{\rm LN}$  are the emissivity and the temperature of the LN. Moreover, the radiance of the blackbody at  $T_{\rm LN}$ , 77K, is near zero. Thus,  $Q_{\rm LN}$  = 0.

 $Q_{\rm HT}$  is the heat transfer from the sample to the air, which is defined as:

$$Q_{\rm HT} = 2A_{\rm s}h(T_{\rm amb} - T_{\rm s}) \tag{2.15}$$

where h is the heat transfer coefficient, which depends on the wind speed, w. In this study, h = 3 + 3w was used [80, 81]. In the in-house experiment, the chamber was sealed, and air from outside could not flow into the chamber, w = 0. Thus, the value of  $h = 3 \text{ Wm}^{-2}\text{K}^{-1}$  was used. The temperature difference between the real and front surfaces was considered due to the low heat conductivity of the glass substrate. They can be regarded as equal, as described in Appendix B; thus, factor 2 was used.

Only emission in the wavelength range of  $\lambda = 2.5$  to 25  $\mu$ m is available. Thus, the integration of  $Q_{\rm rad}$ ,  $Q_{\rm cha}$ ,  $Q_{\rm LN}$  was estimated in this region. This wavelength can cover 83% of all blackbody radiation energy at 300 K.

To estimate the dropped temperature of the sample, the procedure outlined in the previous work was followed [82, 83], where the different temperature  $\Delta T = T_{\rm amb} - T_{\rm s}$  at the steady-state temperature,  $Q_{\rm total}$  is zero. The dropped temperature was calculated at different distances for specific samples in this study. The total power was estimated by solving equations at  $T_{\rm amb} = T_{\rm s}$ .

#### 2.2.2 Field measurement

Field RC measurements were performed with the setup depicted in Figure 4.7. The diagram of heat in the field RC measurement is presented in Figure 2.3(b). The total heat of the sample,  $Q_{\text{total}}$ , is defined below:

$$Q_{\text{total}} = Q_{\text{rad},1} + Q_{\text{rad},2} - Q_{\text{solar}} - Q_{\text{atm}} - Q_{\text{HT}} - Q_{\text{SF}}.$$
 (2.16)

 $Q_{\mathrm{rad},1}$  is the heat of radiation from the upper surface of the sample, which has an emissivity of  $\epsilon_{\mathrm{s}}(\lambda)$  and at the temperature  $T_{\mathrm{s}}$ . It is

$$Q_{\rm rad,1} = \pi A_{\rm s} \int_0^\infty d\lambda I_{\rm BB}(T_{\rm s}, \lambda) \epsilon_{\rm s}(\lambda)$$
 (2.17)

 $Q_{\mathrm{rad,2}}$  is the heat of radiation from the lower surface of the sample, which is glass with

an emissivity of  $\epsilon_{\rm glass}(\lambda)$ , and at the temperature  $T_{\rm s}$ . It is

$$Q_{rad,2} = \pi A_{s} \int_{0}^{\infty} d\lambda I_{BB}(T_{s}, \lambda) \epsilon_{glass}(\lambda)$$
 (2.18)

 $Q_{
m solar}$  is the absorbed heat from sunlight, which depends on the emissivity of the samples in the visible region. It is

$$Q_{\text{solar}}(\theta, \lambda) = \int_{0}^{\infty} d\lambda \epsilon_{s}(\lambda) I_{\text{AM2.0}}(\lambda) \cos\Phi$$
 (2.19)

where,  $\Phi$  is the solar angle concerning the zenith direction. The angle  $\Phi$  at the measurement time was approximately  $60^{\circ}$ . The  $I_{\rm AM2.0}(\lambda)$  is the solar radiation.

 $Q_{
m atm}$  is the absorbed heat from atmosphere. It is

$$Q_{\rm atm} = 2\pi A_{\rm s} \int_0^\infty d\lambda I_{\rm BB}(T_{\rm atm,\lambda}) \epsilon_{\rm s}(\lambda) \int_0^{\pi/2} d\theta \cos\theta \sin\theta \epsilon_{\rm atm}(\theta,\lambda)$$
 (2.20)

where

$$\epsilon_{\text{atm}}(\theta, \lambda) = 1 - t(\lambda)^{\frac{1}{\cos \theta}},$$
(2.21)

 $t(\lambda)$  is the transmittance of the atmosphere and is taken from MODTRAN [84]. The temperature of atmosphere  $T_{\rm atm}$  is used.

 $Q_{\mathrm{PS}}$  is the radiation from the PS which absorbed by the lower glass side of samples. It is written as

$$Q_{\rm PS} = \pi A_{\rm PS} F_{\rm PS \to s} \int_0^\infty d\lambda I_{\rm BB}(T_{\rm amb}, \lambda) \epsilon_{\rm glass}(\lambda) \epsilon_{\rm PS}(\lambda)$$
 (2.22)

where  $A_{\rm PS}$  and  $\epsilon_{\rm PS}$  ( $\lambda$ ) are the area and the emissivity of PS plate, respectively.  $F_{\rm PS \to s}$  is the view factor from the PS to the sample. Since the PS plate is larger than the size of the sample, the  $F_{\rm s \to PS}$  can be regarded as unity. Using the reciprocal theorem,  $A_{\rm s}F_{\rm s \to PS}$  =

 $A_{\mathrm{PS}}F_{\mathrm{PS} 
ightarrow \mathrm{s}}.$  The  $Q_{\mathrm{PS}}$  is:

$$Q_{\rm PS} = \pi A_{\rm s} \int_0^\infty d\lambda I_{\rm BB}(T_{\rm amb}, \lambda) \epsilon_{\rm glass}(\lambda) \epsilon_{\rm PS}(\lambda)$$
 (2.23)

The heat transfer  $Q_{\rm HT}$  given in the in-house RC measurement can be used, where w=1 ms<sup>-1</sup> because covering PE film had gaps and could not completely block the wind. Similar to the in-house calculation, the temperature reduction and the total power were estimated.

#### **CHAPTER 3**

#### OPTICAL PROPERTIES OF SILICA PARTICLES

#### 3.1 Background

In this study, SiO<sub>2</sub> particles were used to investigate SPhP phenomena in the IR region, particularly at the ATW wavelengths, for the RC application. Due to intrinsic properties of SiO<sub>2</sub>, Au capping microspheres were investigated with the expectation that the gold is regarded as the antenna for excited SPhP. Although Au-SiO<sub>2</sub> microspheres did not show the excitation of SPhP at the IR wavelengths, the EOT phenomenon was observed.

Previously, EOT was reported in periodically arranged arrays, such as two-dimensional hole arrays and slits. It occurs in a narrow wavelength range, suggesting that it emerges from surface plasmon resonance. EOT was also reported in metal-capped microsphere crystals [85, 86]. When the microspheres form periodic structures in the order of the light wavelength, the EOT may exhibit a similar mechanism to the ordered holes in a metallic film. This interpretation is supported by abrupt EOT peaks in the transmission spectra. Although these studies are carried out for visible or near-IR light, the EOT in the IR range remains unclear.

In this chapter, both SPhP and EOT phenomena were explained. The SPhP was investigated on SiO<sub>2</sub> microspheres with different diameters ( $\phi$  = 1, 5, and 20  $\mu$ m). The broadband EOT phenomena in Au-SiO<sub>2</sub>-microsphere and Au-PS-microsphere monolayers, in the IR range (5–25  $\mu$ m), were also discussed.

# 3.2 Experimental method

# 3.2.1 Samples for SPhP measurements

The spin-coating method was used to fabricate  $SiO_2$  particles on the glass substrate. For a mono-layer of 5  $\mu$ m-diameter  $SiO_2$  spheres, particle solutions were mixed with ethanol at a mixing volume ratio of 1:1. In the ethanol solution, 0.2 v% of Triton X was added as a surfactant. The  $SiO_2$  solution was centrifuged at 800 rpm for 3 min. Subsequently, 70% of the solvent was removed from the solution. Then, the solution was stirred again via sonication. A mixed  $SiO_2$  solution (approximately 50  $\mu$ l) was dropped on substrates and spin-coated at 1000 rpm for 6 s. For 20  $\mu$ m-diameter  $SiO_2$  beads, particle powder was mixed with the solution at a mixing ratio of 1:3 (mg/ml). The mixed solution was water and ethanol at a volume ratio of 1:2. Then, the particles solution was stirred by the ultrasonic machine. Next, 100  $\mu$ L of mixed  $SiO_2$  particles solution was dropped into the substrate and spin-coated at 1000 rpm for 6 seconds. Finally, samples were dried at room temperature.

### 3.2.2 Samples for EOT measurements

Figure 3.1 presents the preparation process of the Au-SiO<sub>2</sub> monolayer. SiO<sub>2</sub> microspheres were immobilized on a silicon substrate using an adhesive monolayer of a silane-coupling agent, and a 25-nm thick gold film was vacuum-evaporated onto the microsphere monolayers.

The colloidal SiO<sub>2</sub>-bead suspension (sicastar, MPT, Germany) was adopted to form the microsphere monolayer. Their diameters,  $\phi$ , were 0.3, 1, and 3  $\mu$ m. The solid content of the solution was 50 mg/ml. The colloidal suspensions were diluted with pure water at a certain ratio (1/10, 1/10<sup>3</sup>, or 1/10<sup>5</sup>) to control the density of the SiO<sub>2</sub> microspheres on a substrate. The substrate was a 0.53-mm thick silicon wafer (P-type, high resistance, crystal orientation: 100) with a dimension of 25 × 25 mm<sup>2</sup>. They were cleaned by sonication in a aqueous solution of Extran MA 02 (Merk), pure water, isopropanol, and acetone.

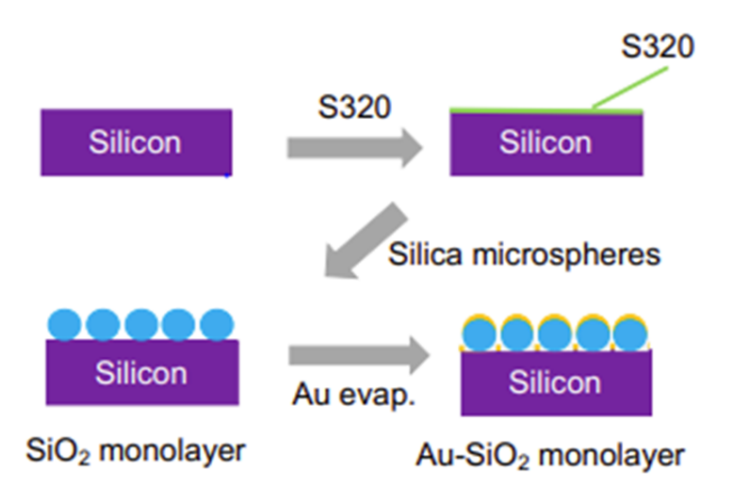


Figure 3.1: Fabrication process of a SiO<sub>2</sub> microsphere monolayer.

The substrate surface was modified with an silane-coupling agent of N-(2 aminoethyl)-3-aminopropyltrimethoxysilane,  $H_2N(CH_2)_2NH(CH_2)_3Si(OMe)_3$  (S320, Sila-Ace, JNC). The S320 monolayer was formed by the immersion of the substrate for 1 h in a mixture solution of an acetic acid/ethanol (5 : 95 v/v), at a volume concentration of 1.1%. The substrates were rinsed with ethanol and were immediately immersed in the  $SiO_2$  colloidal solution for 1 h, to form a  $SiO_2$ -microsphere monolayer. Finally, the substrates were rinsed with deionized water to remove excess  $SiO_2$  microspheres and dried at room temperature. The  $SiO_2$ -microsphere monolayer was coated with a 25-nm thick gold thin film via thermal vacuum evaporation.

For a high-coverage of the Au-PS-microsphere monolayer, the PS bead solution was mixed with ethanol at a mixing volume ratio of 1:3. In the ethanol solution, 0.2 v% of Triton X was added as a surfactant. The PS bead solution was centrifuged at 6500 rpm for 10 min. Subsequently, 42.5% of the solvent was removed from the solution. Then the solution was stirred again via sonication. A mixed PS solution (30  $\mu$ l) was dropped on a silicon substrate and spin-coated at 1000 rpm for 6 s. Medium and low coverage Au-PS microsphere monolayers were prepared on a silicon substrate with a self-assembled monolayer of S320. The PS bead solution was diluted with pure water at the mixing volume of 1:49 and 1:24 for medium and low coverage, respectively. Then, the PS solution was

dropped on the substrate, and left for 30 min. Excess PS particles were removed by rinsing the substrate in pure water and 2-propanol. Finally, samples were dried at room temperature before a gold film was deposited.

## 3.2.3 Measurement

IR spectra were taken with a Fourier-transmission infrared spectrometer (FT/IR-4600, JASCO). The spectral range was from 400 cm<sup>-1</sup> to 4000 cm<sup>-1</sup>, with a resolution of 2 cm<sup>-1</sup>. The corresponding wavelength range is  $2.5-25 \mu m$ . The spot size was 5 mm in a diameter. The IR light is normally incident to the sample with no focusing.

The monolayer was observed via optical microscope with a magnification of 50 times and SEM (JSM-6610A (JEOL)). In addition, the surface coverage of the microspheres was evaluated by the SEM images using the ImageJ software (National Institutes of Health, USA) [87, 88].

Both the transmittance and normalized transmittance were considered to investigate EOT phenomena. The normalized transmittance,  $T_{\rm normalized}$ , indicates the transmittance passing through a single particle. In addition, the transmittance of Au-caped microsphere, T, was estimated by the equation:

$$T = T_{\text{film}} \times (1 - \sigma) + T_{\text{normalized}} \times \sigma, \tag{3.1}$$

where,  $\sigma$  and  $T_{\rm film}$  are the coverage of particles and the transmittance of the gold film, respectively. Since, the transmittance of the gold thin film is absent,  $T_{\rm normalized} = T/\sigma$ .

#### 3.3 Results of SPhP

Figure 3.2 presents the absorption cross-section,  $C_{\rm abs}$ , of SiO<sub>2</sub> microsphere with different diameters, calculated as a function of the wavelength, based on the Mie theory. The cross-section for diameter  $\phi$  = 5 and 20  $\mu$ m were resized to 0.1 and 0.02 of their original. In

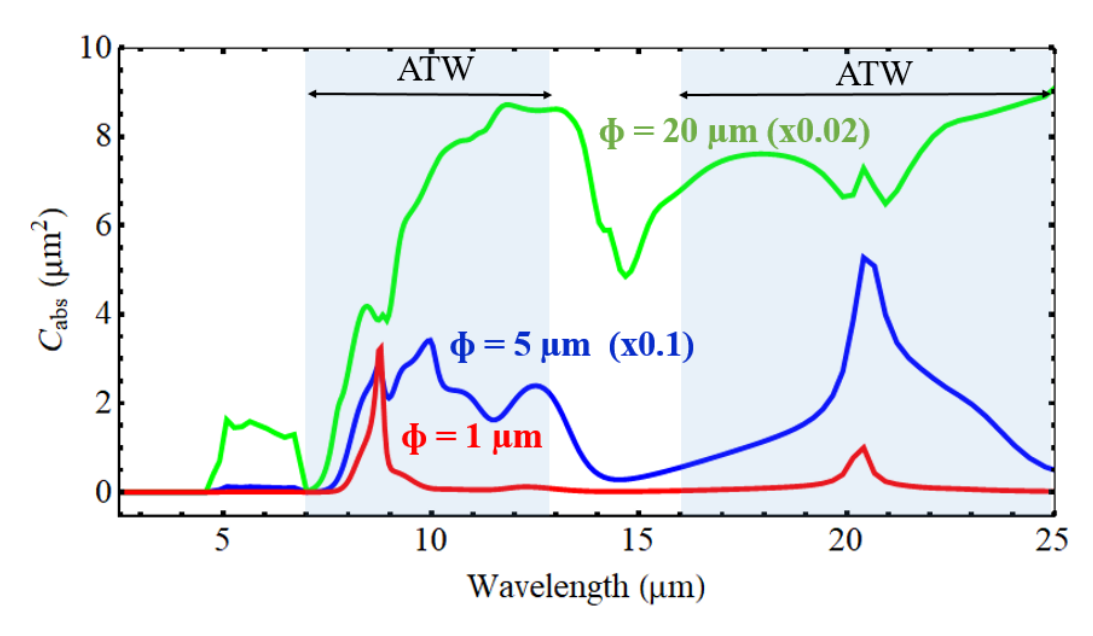


Figure 3.2: Absorption cross-section of SiO<sub>2</sub> microspheres based on the Mie theory. Noted that results of  $\phi = 5$  and 20  $\mu$ m were multiplied by 0.1 and 0.02, respectively.

1  $\mu$ m-diameter SiO<sub>2</sub> particles, resonance peaks are observed at 9 and 21  $\mu$ m, where the imaginary permittivity has a peak, and the real permittivity is negative (Figure 1.2). When increasing the diameter, the absorption cross-section increases, and tails of resonance peaks cover all wavelength ranges of the ATW.

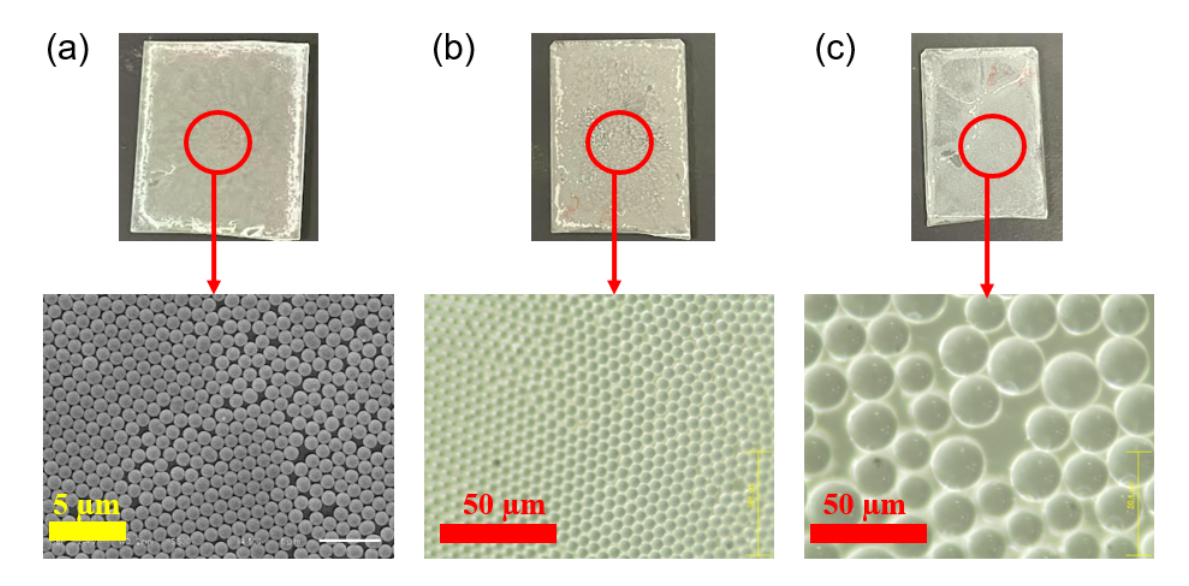


Figure 3.3: Images of SiO<sub>2</sub> particles on the glass substrate: (a)  $\phi = 1 \mu m$ , (b)  $\phi = 5 \mu m$ , (c)  $\phi = 20 \mu m$ .

Figure 3.3(a) presents optical and SEM images of SiO<sub>2</sub> with  $\phi = 1~\mu m$ . Figure 3.3(b)

and Figure 3.3(c) present optical and optical microscope images of  $SiO_2$  with  $\phi = 5$ , 20  $\mu$ m. Images indicate that the monolayer of the  $SiO_2$  beads is formed on the substrate with well-ordering. Some vacancies or dislocations where the substrate is visible are induced during the fabrication process, which are believed to have a negligible effect on the sample's properties.

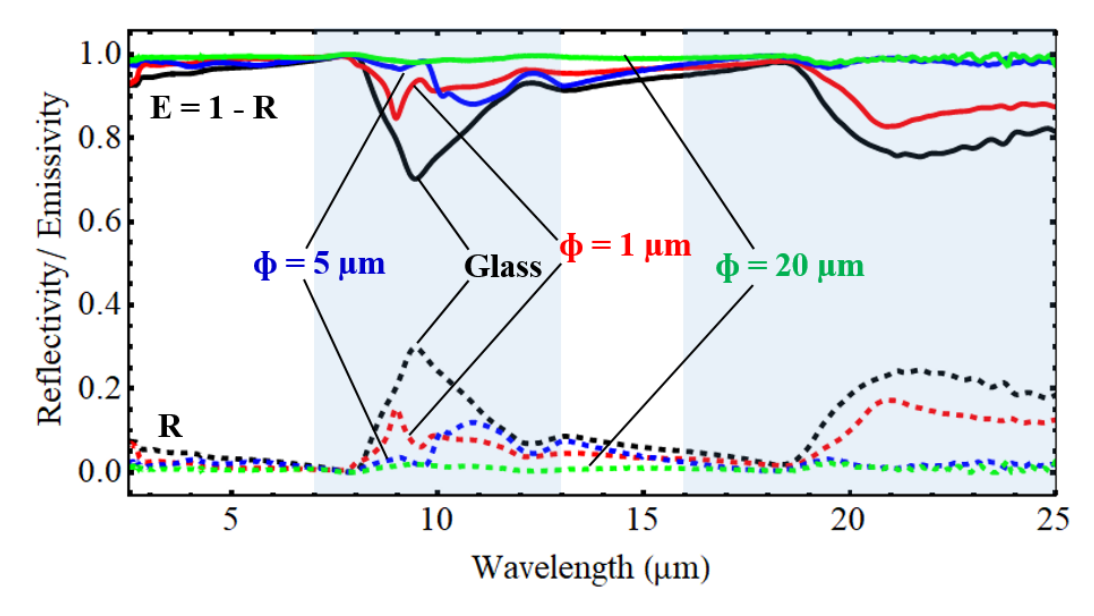


Figure 3.4: Reflectivity and emissivity of  $SiO_2$  spheres on the glass substrate. The hatched areas indicate the ATW. The dashed line is measured reflectance, R. The solid line is estimated emissivity, E = 1 - R, when assuming T = 0.

The reflectance spectrum was measured by the FTIR spectrometer, with the Al mirror being used as the reference. Emissivity was estimated by reflectivity, E=1-R, assuming that the transmittance T=0. Figure 3.4 presents the reflectivity/ emissivity of SiO<sub>2</sub> spheres on the glass substrate. The result of a glass plate is plotted as the reference. In its bulk form, the glass presents the broad and weak absorption peaks arising from the interaction of optical phonon and electromagnetic radiation, so-called bulk phonon-polaritons resonance [89, 90]. In detail, there is the Si-O-Si stretching, located at 8.4-9.8  $\mu$ m (at a wavenumber of 1193-1025 cm<sup>-1</sup>). And the other bending of O-Si-O is located at 22  $\mu$ m (at a wavenumber of 452 cm<sup>-1</sup>) [91].

However, when the glass is coated with a monolayer of SiO<sub>2</sub> spheres, the reflectiv-

ity band disappears and is replaced by the high emissivity. The reflectivity exhibits high broadband emissivity over the full IR spectrum and decreases with particle sizes. For detail, in the 1  $\mu$ m-diameter SiO<sub>2</sub> particles, two resonance peaks were observed at 9 and 21  $\mu$ m, which coincides with the Mie theory results. In the results of 5  $\mu$ m-diameter SiO<sub>2</sub> particles, the resonance peaks expand over the wavelength range. In the 20  $\mu$ m-diameter SiO<sub>2</sub> particles, the emissivity is nearly unity, where the reflectivity is approximate zero. It is obvious that the high emissivity covers all wavelength ranges of the IR region, especially at the ATW.

The enhanced emissivity in the monolayer SiO<sub>2</sub> lies in two different modes [89, 90]. Firstly, it is due to the out-coupling of SPhP states. When a polar dielectric material is formed into tiny particles, the out-coupling of SPhP states can be maximized compared to the bulk [89]. Secondly, it corresponds to the spherical geometry of particles. The SiO<sub>2</sub> beads form non-vertical walls in contact with the dielectric medium such as air. The change in shape translates into differential polar-dielectric boundaries, which result in a variation of the refractive index. Thus, the spherical shape provides an impedance matching between the polar and dielectric media over the extensive ranges of wavelengths [89, 90].

Glass is inexpensive, chemically stable, and has high emissions in the IR region. In addition,  $20 \mu m$ -diameter  $SiO_2$  particles on the glass sample shows high emissivity, nearly unity. Thus, the glass and particles on the glass samples were chosen as the RC material's reference. The calculated and measured results indicate that the larger  $SiO_2$  size promises high RC efficiency, which will be explained in Chapter 4.

For the small  $SiO_2$  particles, such as  $\phi = 1~\mu m$ , only shape peaks are observed, and the tails of peaks do not cover the ATW. Thus, tiny particles are not promising for high RC efficiency. The  $SiO_2$  beads were coated with a thin gold film with the expectation that the gold film could act as the antenna for excited SPhP in the broadband wavelength range. However, Au- $SiO_2$  microspheres did not work in exciting resonance; the EOT phenomenon was explored. In the section below, this phenomenon will be explained more detail.

# 3.4 Experimental results of EOT

# 3.4.1 SiO<sub>2</sub>, and Au-SiO<sub>2</sub>-microsphere monolayers

Figure 3.5 presents SEM images of  $SiO_2$ , and Au- $SiO_2$ -microsphere monolayers. The coverages of the microspheres are 0.87 and 0.86, respectively. The diameter of  $SiO_2$  and thickness of a gold film are 1  $\mu$ m and 25 nm, respectively.

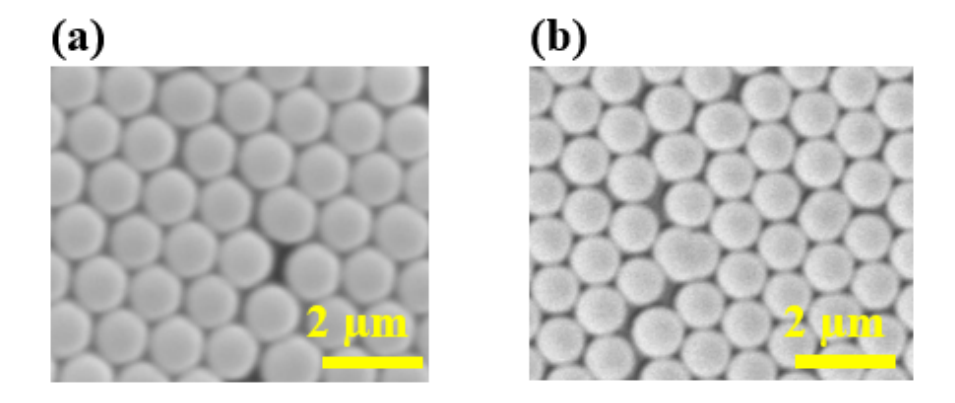


Figure 3.5: SEM images of (a) SiO<sub>2</sub>, and (b) Au-SiO<sub>2</sub>-microsphere monolayers

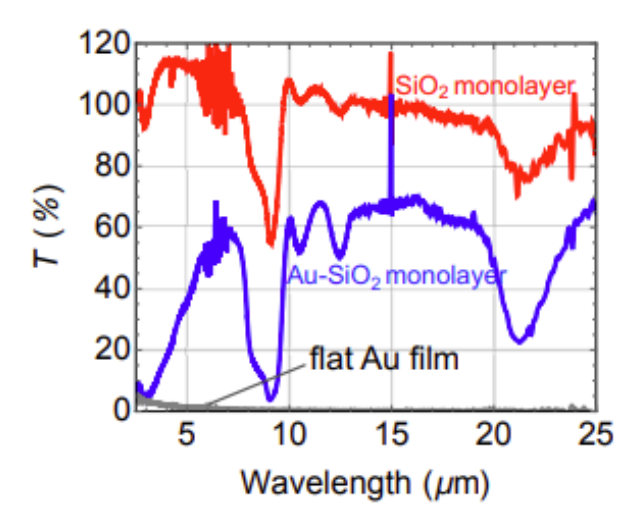


Figure 3.6: Transmittance spectra of a 25 nm-thick Au film, SiO<sub>2</sub>, and Au-SiO<sub>2</sub>-microsphere monolayers.

The transmittance spectra of the Au-SiO<sub>2</sub>- and SiO<sub>2</sub>-microsphere monolayers are presented in Figure 3.6. The baseline was taken with a silicone plate that was used as a substrate. The transmittance was evaluated as the ratio of the light intensity transmitted

through the sample to that of the silicone plate. In addition, the transmittance spectra of a 25-nm thick flat gold film was also measured.

The SiO<sub>2</sub>-microsphere monolayer has a transmittance approximately 100% over the wavelength ranges, except for the wavelengths of the SPhPR, at 9 and 21  $\mu$ m. The transmittance, T, is higher than 100% at the wavelengths from 3 to 7.5  $\mu$ m, as SiO<sub>2</sub> microspheres function as an antireflection coating and reduces the reflectance at the silicone surface.

On the other hand, the Au-SiO<sub>2</sub>-microsphere monolayer has a transmittance approximately 60% over the wavelength range of 5–25  $\mu$ m, except for the wavelengths of the SPhPR, although the surface was fully covered with a 25-nm thick gold film. A 25-nm thick flat gold film transmits less than 1.5% over this wavelength range, which is significantly less than the Au-SiO<sub>2</sub>-microsphere monolayer. These results imply that the gold coating does not prevent the light transmission at the wavelengths. In a previous report [85], the EOT is observed in a narrow wavelength range in the near-IR range ( $\lambda$  = 0.4-1  $\mu$ m). The high transmittance observed in this study has no peak, which indicates a different EOT mechanism. The low transmittance at wavelengths shorter than 5  $\mu$ m stems from the imaginary permittivity of gold at this wavelength range. This also set off the slight increase in the transmittance spectra of the flat gold film at this wavelength range.

# 3.4.2 Coverage dependence

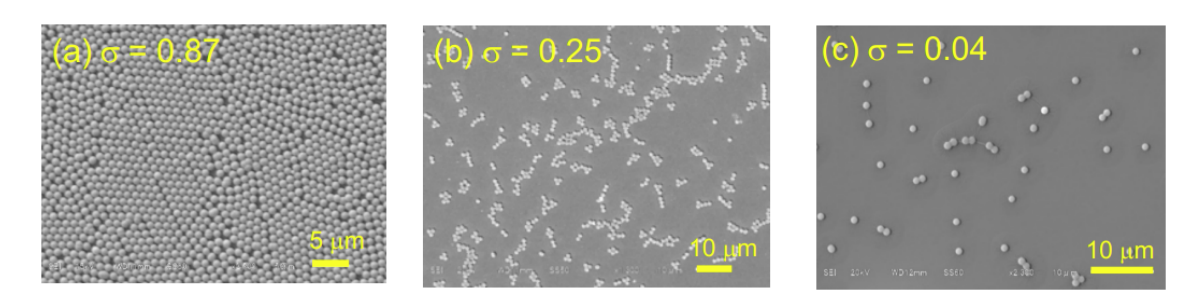


Figure 3.7: SEM images of the Au-SiO<sub>2</sub> microsphere monolayers.

Figure 3.7 presents SEM images of the Au-SiO<sub>2</sub>-microsphere monolayers. The diameter of the microspheres and the thickness of the gold coating were 1  $\mu$ m and 25 nm,

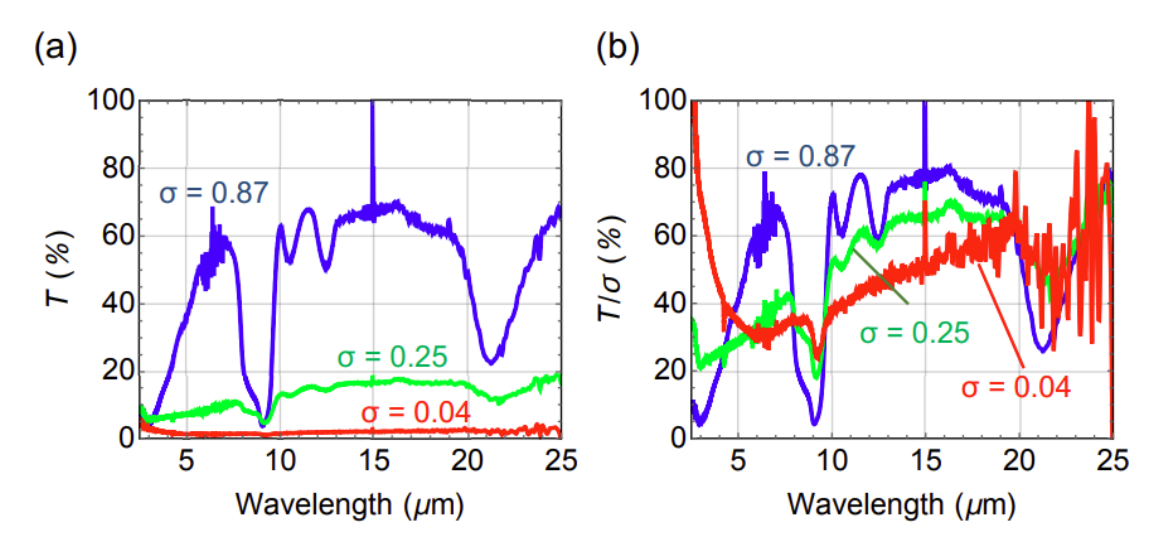


Figure 3.8: (a) Transmittance spectra of the Au-SiO<sub>2</sub>-microsphere monolayers with different coverages,  $\sigma$ , and (b) their transmittance spectra normalized by the coverages.

respectively. The Au-SiO<sub>2</sub>-microsphere monolayers with three different microsphere coverages were prepared by altering the dilution ratio of the colloidal suspension: (a) 1/10, (b)  $1/10^3$ , and (c)  $1/10^5$ , respectively. The mean coverages,  $\sigma$ , evaluated from the SEM images were 0.87, 0.25, and 0.04. At the highest coverage,  $\sigma = 0.87$ , Figure 3.7(a), the microspheres are ordered, and they form two-dimensional crystals. At  $\sigma = 0.25$ , Figure 3.7(b), the microspheres form linear aggregates and the distance between the aggregates are 10  $\mu$ m. At a low coverage,  $\sigma = 0.04$ , Figure 3.7(c), most microspheres are isolated, and some form dimers or trimers.

Figure 3.8(a) presents the transmittance spectra of Au-SiO<sub>2</sub>-microsphere monolayer with different coverages,  $\sigma$ . At  $\sigma$  = 0.87, the transmittance is highest (approximately 60%), and at  $\sigma$  = 0.25 and  $\sigma$  = 0.04, it is approximately 15% and 3%, respectively. The transmittance decreases with a decrease in the coverage, indicating that light is transmitted through Au-capped microspheres. The transmittance normalized by the coverage,  $T/\sigma$ , is also plotted in Figure 3.8(b). Even in the normalized transmittance spectra, the transmittance decreases with a decrease in the coverage. This means that the transmittance is not proportional to the number of microspheres. The dielectric microsphere lattice played an important role in transmission enhancement.

# 3.4.3 Size dependence

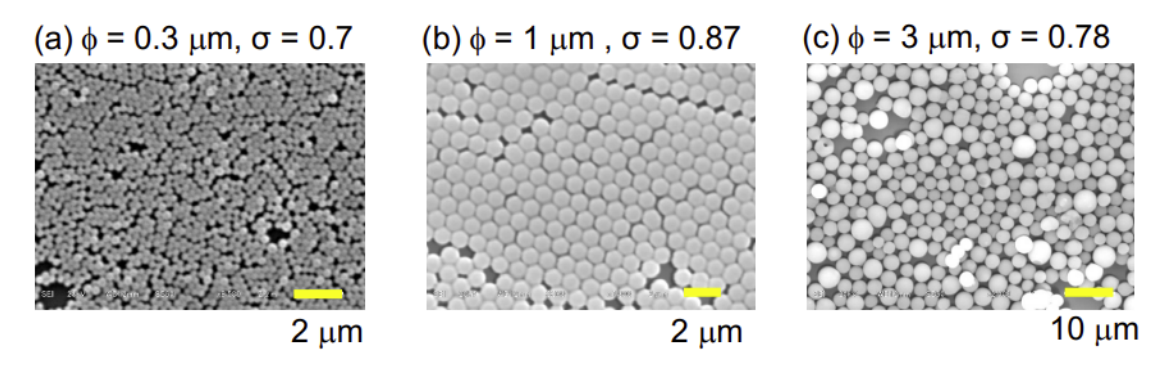


Figure 3.9: SEM images of the Au-SiO<sub>2</sub> microsphere monolayers of different microsphere diameters.

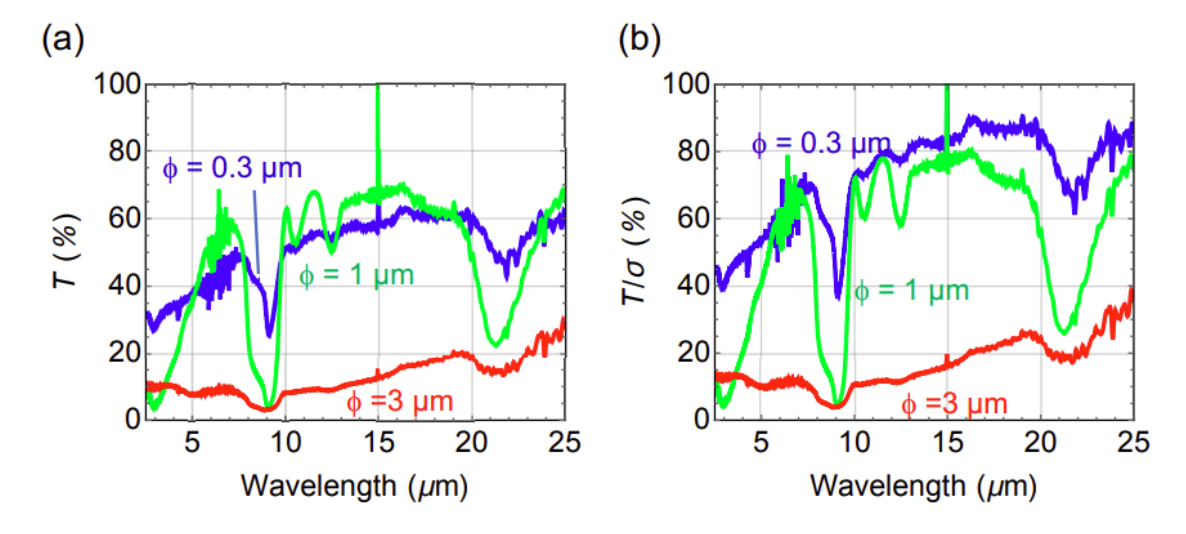


Figure 3.10: (a) Transmittance spectra of the Au-SiO<sub>2</sub>-microsphere monolayers with different diameter,  $\phi$ , and (b) their transmittance spectra normalized by the coverages.

Transmittance spectra of the Au-SiO<sub>2</sub>-microsphere monolayers with different microsphere sizes were examined. Figure 3.9 presents their SEM images. The microspheres in the monolayer ( $\phi = 0.3$  and 1  $\mu$ m) consist of two-dimensional crystals, and the microspheres are attached, whereas the microspheres in the monolayer ( $\phi = 3 \mu$ m) are not ordered well, and the microspheres are separated with gaps, resulting in the lower coverage. This low order may be caused by the large deviation of the microsphere sizes. The transmittance spectra of the Au-SiO<sub>2</sub>-microsphere monolayers are presented in Figure 3.10(a), and the spectra normalized by the coverages are presented in Figure 3.10(b). The ordered mono-

layers of ( $\phi$  = 0.3 and 1  $\mu$ m) have high transmittance, whereas that of  $\phi$  = 3  $\mu$ m is low at approximately 30%, even in the normalized spectrum. This low transmittance at  $\phi$  = 3  $\mu$ m is owing to the gaps between the microspheres, as discussed in the next session, based on the FDTD calculations.

# 3.4.4 Material independence

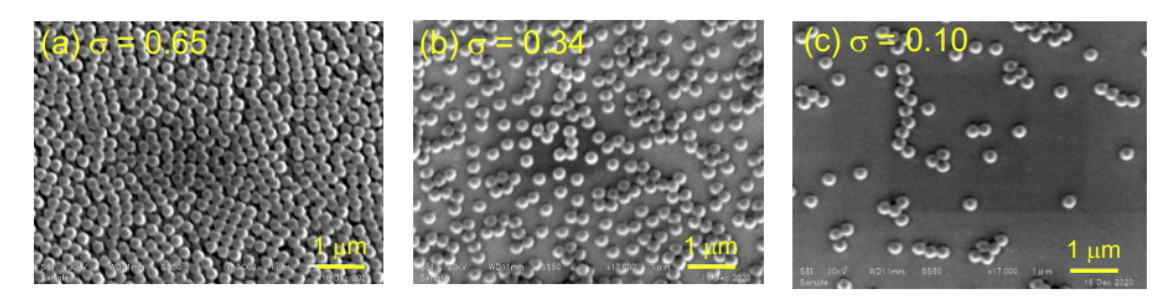


Figure 3.11: SEM images of the Au-PS microsphere monolayers.

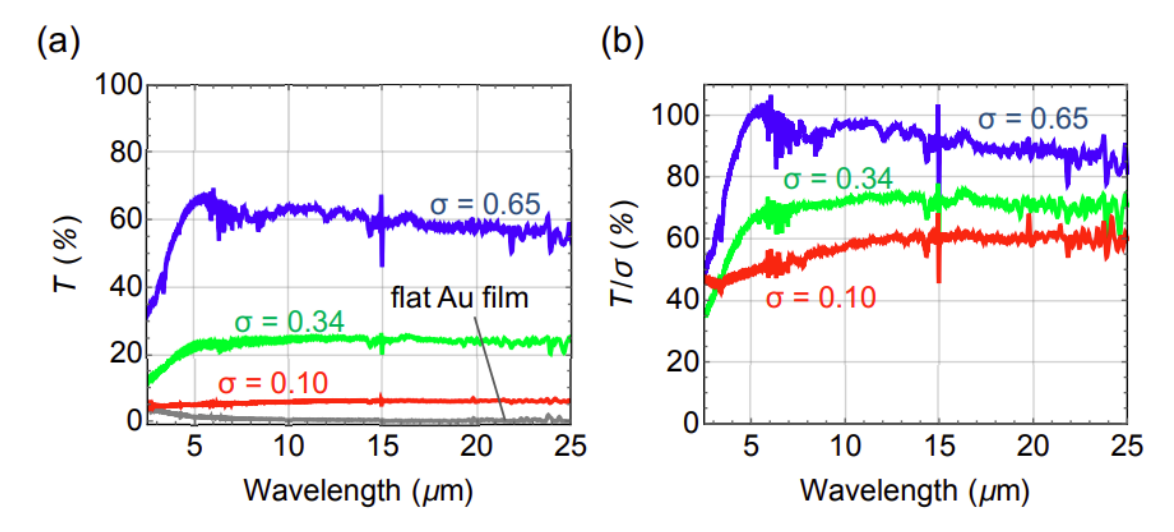


Figure 3.12: (a) Transmittance spectra of the Au-PS-microsphere monolayers with different coverage,  $\sigma$ , and (b) their transmittance spectra normalized by the coverage.

The transmission spectra of the Au-PS-microsphere monolayers were also measured to confirm the microsphere materials' independence from the EOT. The PS particles do not present the SPhP resonance in the IR region. Au-PS-microsphere monolayers ( $\phi$  = 0.25 µm) with coverages of  $\sigma$  = 0.65, 0.34, and 0.10 were prepared. SEM images are presented in Figure 3.11. The microspheres form two-dimensional crystals at  $\sigma$  = 0.65, and

they are isolated in the Au-PS-microsphere monolayers at  $\sigma=0.30$  and 0.10. Coverage is similar to those of the Au-SiO<sub>2</sub>-microsphere monolayers, as discussed above. The transmittance spectra of the Au-PS-microsphere monolayers are presented in Figure 3.12(a), together with the spectra of a 25-nm thick flat gold film. The EOT phenomena of Au-PS-microsphere monolayers occur. Their spectra are almost constant with no peaks, and is approximately 60%, 25%, and 6% for  $\sigma=0.65, 0.34,$  and 0.10, respectively. The corresponding normalized transmittance is presented in Figure 3.12(b). Similar to the Au-SiO<sub>2</sub>-microsphere monolayers, the normalized transmittance of the Au-PS-microsphere monolayers decreases with decreasing coverage. The EOT observed in the Au-PS-microsphere monolayers without any dips suggests that the EOT is not due to SPhPR, and does not depend on the dielectric material. This is supported by the FDTD calculation below.

#### 3.5 Calculated results of EOT

### 3.5.1 SiO<sub>2</sub>, and Au-SiO<sub>2</sub>-microsphere monolayers

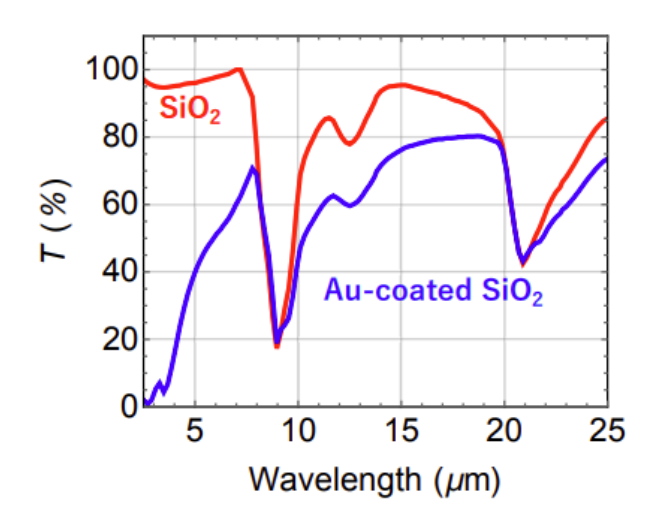


Figure 3.13: Calculated transmittance spectra of the  $SiO_2$ , and  $Au-SiO_2$ -microsphere monolayers 1  $\mu$ m in diameter.

To investigate the EOT mechanism, the SiO<sub>2</sub>- and Au-SiO<sub>2</sub>-microsphere monolayers were modeled. The microspheres form a square lattice, with a lattice constant equal to the microsphere diameter at  $\phi = 1$  µm. Then, the coverage is  $\sigma = \pi/4 = 0.79$ . First, the trans-

mittance spectra of the SiO<sub>2</sub>- and the Au-SiO<sub>2</sub>-microsphere monolayers were presented in Figure 3.13. The gold film thickness capping the microsphere was set to be 25 nm. The corresponding experimental spectra are shown in Figure 3.6. In the IR region (5-25  $\mu$ m), a high transmittance is observed for both structures, except for the SPhPR dips at 9 and 21  $\mu$ m. The absolute transmittance almost agrees with the experimental results, as presented above. Hence, the FDTD calculation optimally reproduce the experimental results.

# 3.5.2 Coverage dependence

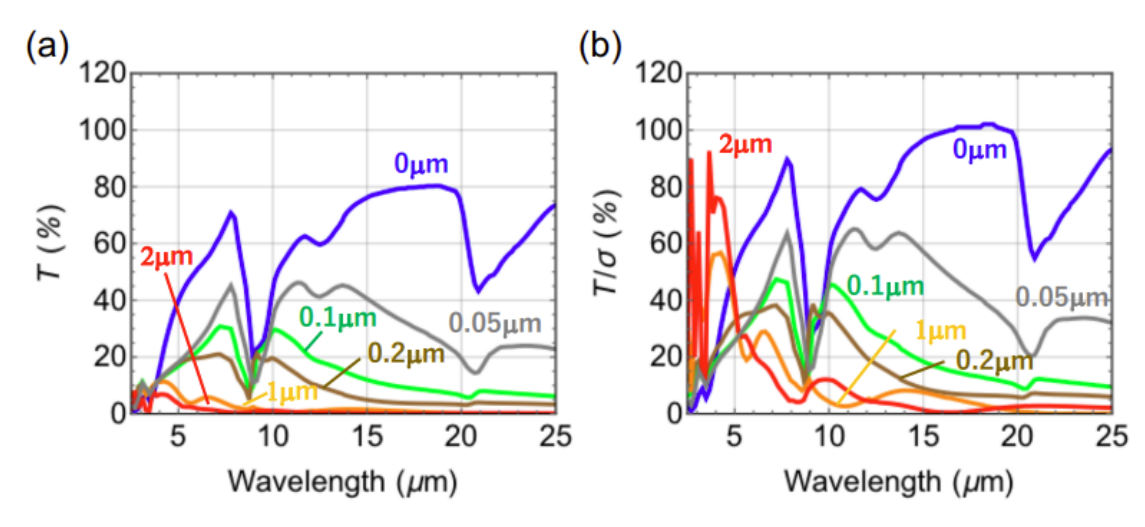


Figure 3.14: Calculated transmittance spectra of the Au-SiO<sub>2</sub> with various inter-particle distances, and (b) their transmittance spectra normalized by the coverage,  $\sigma$ .

The transmittance spectra of the Au-SiO<sub>2</sub>-microsphere monolayers ( $\phi$  = 1  $\mu$ m) with different inter-sphere gaps, g, were presented in Figure 3.14(a). The models with six different gaps were examined. The spheres are attached at g = 0. The transmittance T decreases with the increase in the gap distance g over the spectral range. The low transmittance is owing to the low coverage of the microspheres. To validate this statement, the transmittance normalized by the coverage,  $\sigma$ , was presented in Figure 3.14(b). Normalized transmittance decreases with  $\sigma$ , indicating that the transmittance is significantly affected by the gap distance, or the coverage of microspheres.

Figure 3.15 plots calculated and measured transmittance, T, as a function of coverage,

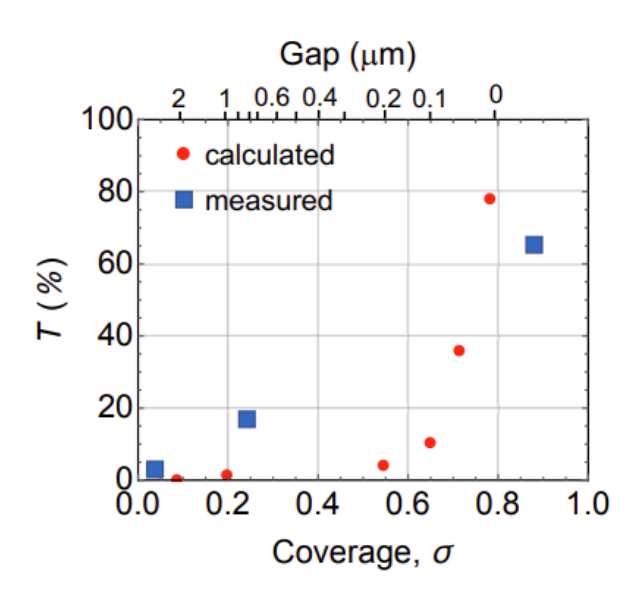


Figure 3.15: Calculated and measured transmittance at a wavelength of 16  $\mu$ m, T, as a function of coverage  $\sigma$  and the gap distance.

 $\sigma$ , at 16  $\mu$ m, where the SiO<sub>2</sub> microsphere is free from the SPhPR. The measured transmittance is taken from Figure 3.8. The calculated and measured transmittance are discrepant, particularly at the low coverage. This is owing to the aggregation of the microspheres in the Au-SiO<sub>2</sub>-microsphere monolayers at  $\sigma$  = 0.25 and 0.04, as presented in the SEM images of Figure 3.7. In the calculation models, the microspheres are isolated. This result indicates that aggregated microspheres exhibit higher transmittance than those of isolated microspheres.

# 3.5.3 Gap between microspheres

The transmittance spectra of the two models are calculated to investigate the EOT. Model 1a is an Au-SiO<sub>2</sub>-microsphere monolayer on a silicon substrate. The microspheres are attached, i.e., g=0, as shown in Figure 3.16(a). The thickness of the gold coating is 25 nm. Model 1b is a 25 nm-thick gold film with 1  $\mu$ m-diameter holes. Model 1b is the geometry of Model 1a without the spheres. The surface appears to be covered with gold when observed from the top. The side view is the cross-sectional view containing the points where the spheres are in contact. Gold was absent on this cross-sectional plane, although

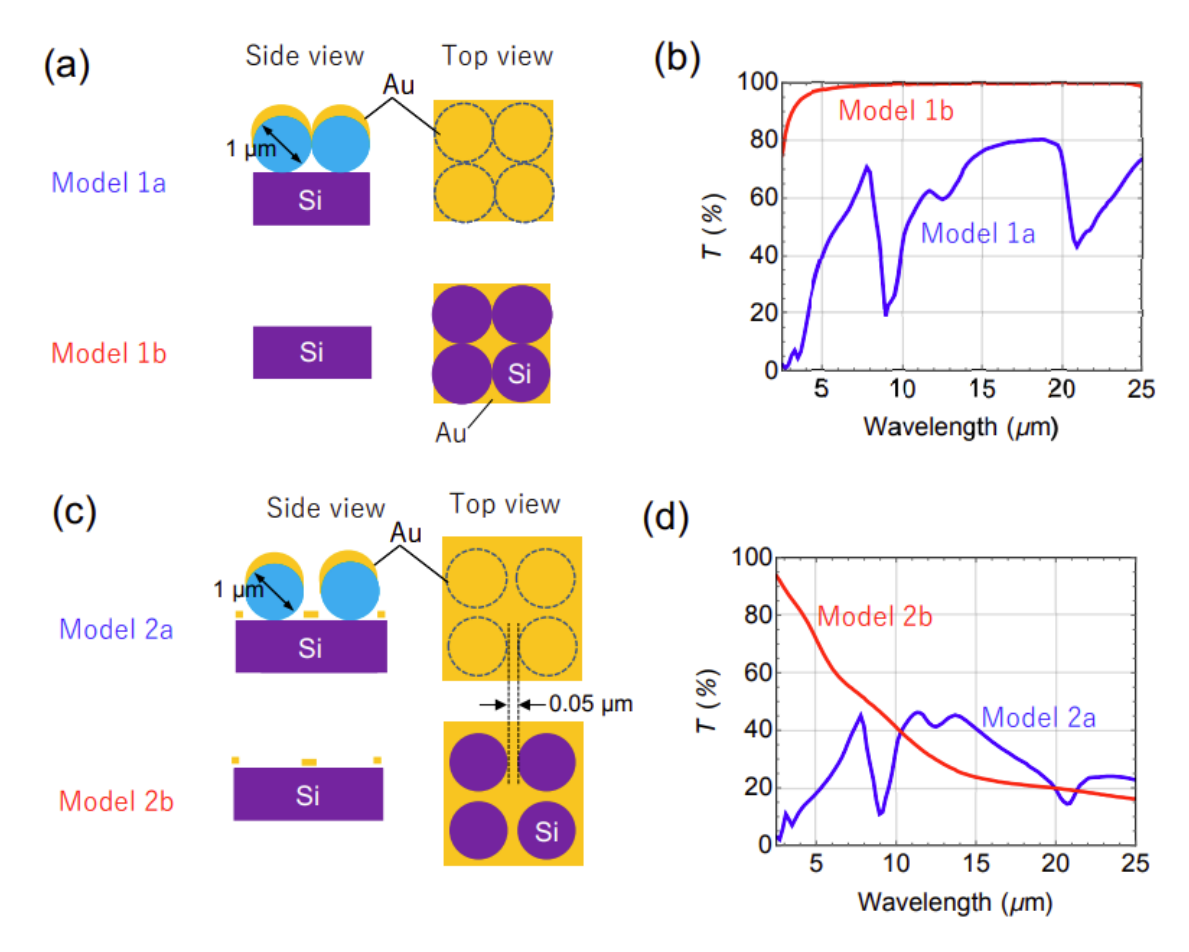


Figure 3.16: (a) Schematic drawing of Model 1, where the microsphere are attached (g=0). Model 1b is Model 1a without the microspheres. (b) Transmittance spectra of Models 1(a) and 1(b). (c) Schematic drawing of Model 2, where the microspheres are separated with a gap of 0.05  $\mu$ m. Model 2b is Model 2a without the microspheres. (d) Transmittance spectra of Model 2(a) and 2(b).

thin diamond-shaped gold films exist on the silicon substrate.

The calculated spectra of Model 1a and 1b are presented in Figure 3.16(b). Model 1b has a high transmittance over the IR range, although the coverage of the thin diamond-shaped gold films is calculated as 21%. This means that the light is transmitted through the circular gaps between the diamond-shaped gold films because each diamond-shaped gold film is isolated. Previously, a similar EOT phenomenon via metallic grating in the IR range was reported [92].

Figure 3.16(c) presents the top and side view of the Model 2a with  $g = 0.05 \mu m$ . In contrast to Model 1, the gold film on the substrate is continuous and contains holes; thus,

the transmittance is low. The calculated spectra of Models 2a and 2b are presented in Figure 3.16(d). The transmittance of Model 2b monotonically decreases with the wavelength. The transmittance of Model 2b is higher than that of Model 2a at a wavelength range longer than 10  $\mu$ m. In this wavelength region, the Au- SiO<sub>2</sub> microspheres promote the transmission, and the transmittance of Model 2a is greater than that of Model 2b. This means that the Au-SiO<sub>2</sub> spheres function as light collectors to collect the light and allow it to pass through the hole, thereby resulting in a greater transmittance.

# 3.5.4 Size dependence

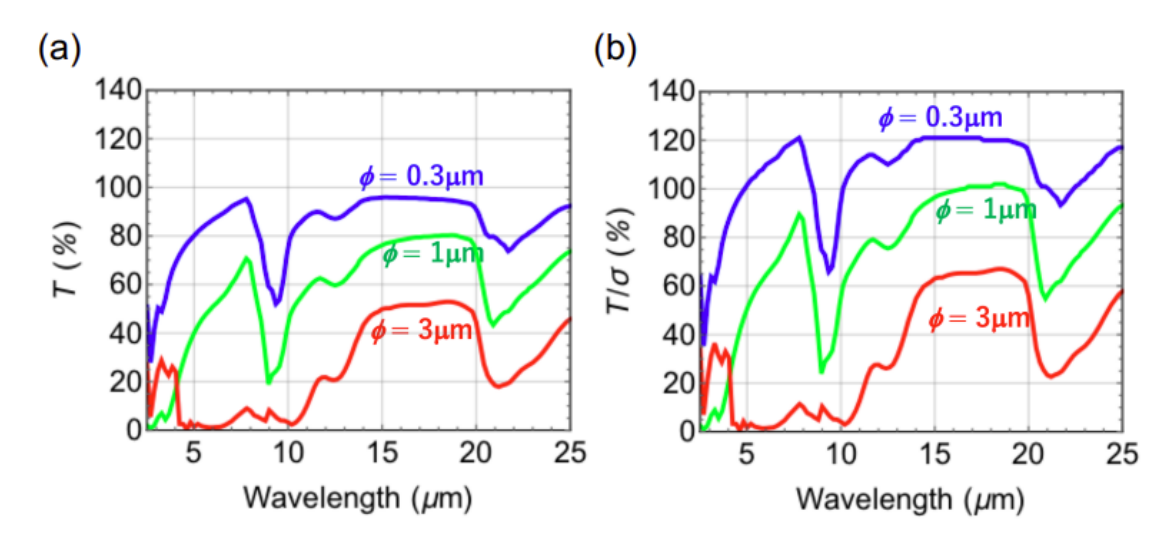


Figure 3.17: Calculated transmittance spectra of the Au-SiO<sub>2</sub>-microsphere monolayers with various size  $\phi$  = 0.3, 1, 3  $\mu$ m and (b) their transmittance spectra normalized by the coverage,  $\sigma$ .

The transmittance spectra calculated for the Au-SiO<sub>2</sub>-microsphere monolayers of different diameters,  $\phi$ , are presented in Figure 3.17(a). The corresponding experimental results are presented in Figure 3.10. The spectra are normalized by the coverage, as illustrated in Figure 3.17(b). Obviously, the transmittance decreases with the size of the microsphere, even in the normalized spectra. This results does not agree with the experimental results, in which the Au-SiO<sub>2</sub>-microsphere monolayers at  $\phi = 0.3 \ \mu m$  are similar to that at  $\phi = 1 \ \mu m$ , in the normalized transmittance spectra in Figure 3.10(b). The difference may be

triggered by the low coverage of the Au-SiO<sub>2</sub>-microsphere monolayer ( $\phi = 0.3 \mu m$ ), where the microsphere crystals are separated, and the low order of the microspheres ( $\phi = 3 \mu m$ ).

The decrease in transmittance with the microsphere size suggests that light is transmitted along the surface of the Au capping microspheres (outer circumference) rather than through the entire microspheres. Consider the top-view of a microsphere monolayer forming a square lattice. The surface number density of the microsphere, N, in a square lattice is written as  $N=1/(4r^2)$ , where r is a diameter of the microspheres relative to the unit length. The surface area of the microsphere is constant at  $\pi/4$ , and is independent of the microsphere size. In contrast, the length of the microsphere circumference, L, is  $L=\pi/(2r)$ , indicating that L increases with decreasing r. Considering the results in which transmittance increases with decreasing size, it is suggested that light propagates along the microsphere circumference. For instance, light passes through the gaps between the gold film on the substrate and on the microspheres; hence the transmittance is high as microspheres are tiny. This picture is supported by the temporal variation of the electric field calculated by the FDTD calculation.

## 3.5.5 Gold thickness dependence

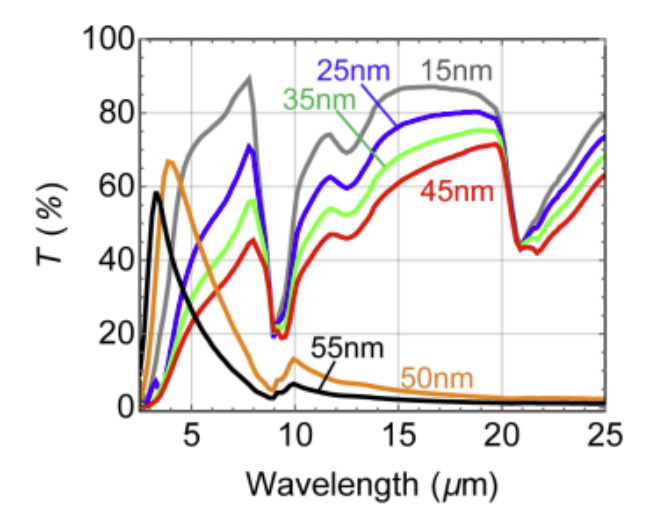


Figure 3.18: Calculated transmittance spectra of the Au-SiO<sub>2</sub> with 1  $\mu$ m in diameter, and difference gold thickness.

The calculated transmittance spectra of the Au-SiO<sub>2</sub>-microsphere monolayers ( $\phi = 1$   $\mu$ m) with different gold thicknesses, d, are presented in Figure 3.18. With increasing the gold thickness, the transmittance gradually decreases, and it is greater than 40% even for the thick gold film at d=45 nm. The transmittance of the Au-SiO<sub>2</sub>-microsphere monolayers with  $d \geq 50$ nm are significantly lower than the others at wavelengths longer than 5  $\mu$ m. This may be due to gold clogging up the spaces between the gaps and the gold caps become continuous with low resistivity. Details are under investigation and will be reported elsewhere.

### 3.5.6 Material independence

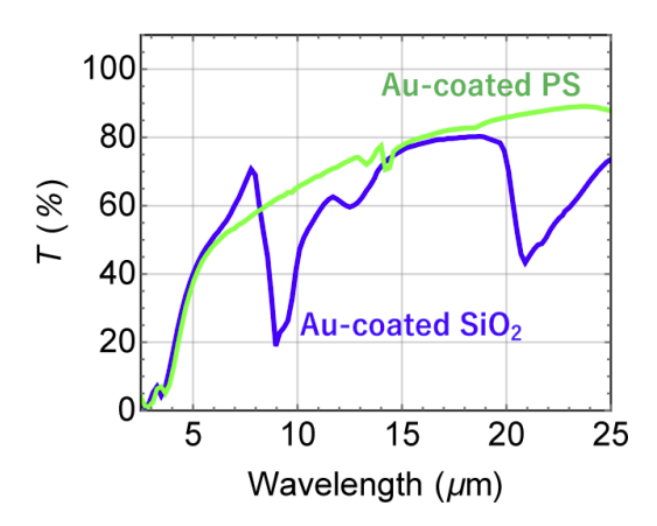


Figure 3.19: Calculated transmittance spectra of the Au-SiO<sub>2</sub>, and Au-PS-microsphere monolayers 1  $\mu$ m in diameter.

Figure 3.19 presents calculated transmittance spectra of the Au-SiO<sub>2</sub>- and Au-PS- microsphere monolayers 1- $\mu$ m in diameter. The transmission spectra are almost similar except for the wavelengths of the SPhPR regions of SiO<sub>2</sub> at 9 and 21  $\mu$ m. In the experimental transmittance spectra of the Au-PS-microsphere monolayers (Figure 3.12), the dips stemming from the SPhPR are absent. Thus, the results contributed that the SPhPR does not play a role in the EOT observed in this study. The EOT is independent of the dielectric materials.

### 3.5.7 Electric distribution

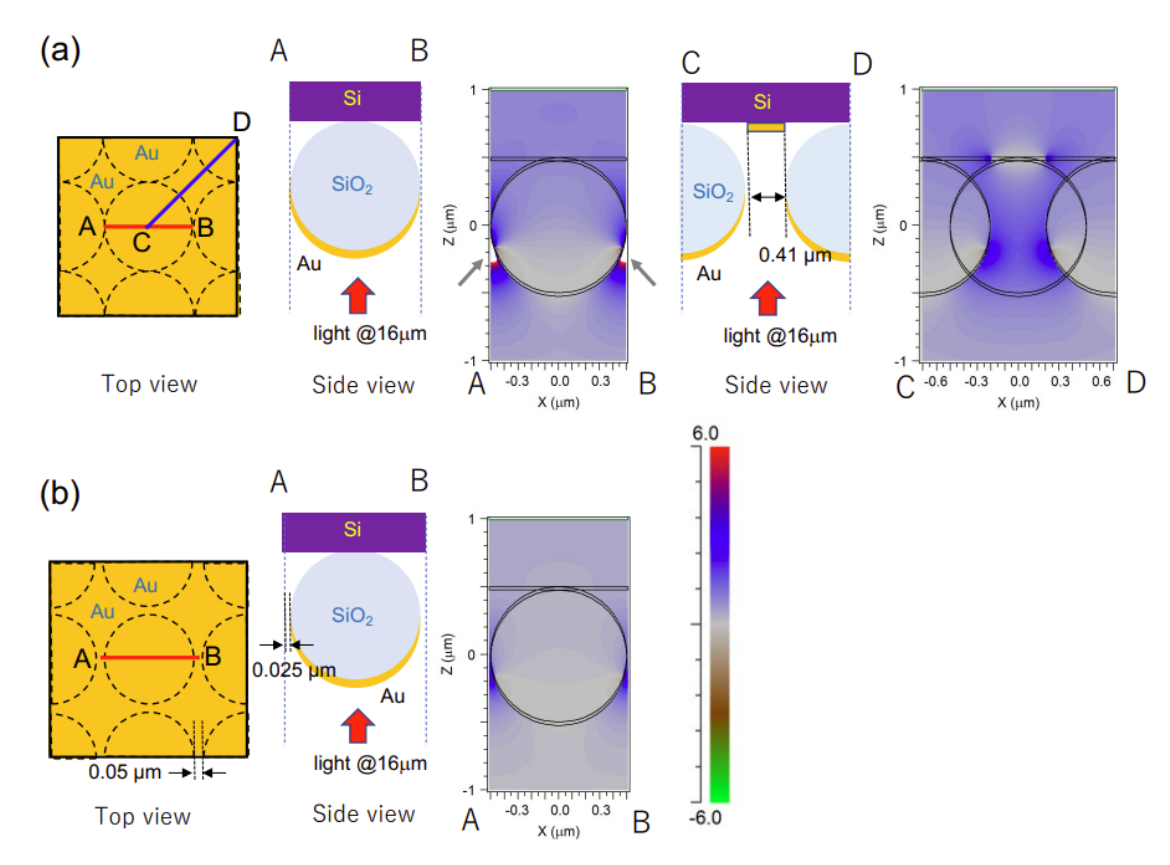


Figure 3.20: (a) Electric field distribution profile of the Au-SiO<sub>2</sub> microsphere monolayer forming a square lattice, where the microspheres are attached ( $g = 0 \mu m$ ), and excited by light at a wavelength of 16  $\mu m$ . Both electric field distributions in the cut plane including AB and CD are illustrated. The white parts at the boundaries A and B represent the electric field grater than 6 (indicated by arrows). (b) Electric field distributions in the cut plane including AB, where the spheres are separated with gaps ( $g = 0.05 \mu m$ ).

Temporal variations in the electric field distribution are calculated via the FDTD method at a wavelength of 16  $\mu$ m, where the SiO<sub>2</sub> microspheres are free from the SPhPR effect. The top and side views of the model for the calculation are presented in Figure 3.20(a). The calculation model is the Au-SiO<sub>2</sub>-microsphere monolayer forming a square lattice, where the microspheres are attached ( $g=0~\mu$ m). The absolute value of the incident field was set to be unity.

Electric field distributions in the cut plane, including AB and CD, are shown. The electric field is enhanced at the point where the spheres are attached, and the light is transmitted

as in the electric field distribution map of the cut plane, including AB. The white parts at the boundary (indicated by arrows) represent the electric field greater than 6, and the maximum electric field is calculated to be approximately 18. The electric field behind the gold cap is negligibly weak owing to the low transmittance of the gold film capping the microspheres. Hence, light passes through the gaps and openings between the gold capping microspheres.

The electric field distributions in the cut plane with CD, where spheres are not in contact, are also illustrated. Even in this model, light is transmitted in a direction along the microsphere surface. These phenomena are not observed for the model with no gold caps, i.e.,  $SiO_2$ -microsphere monolayer. Therefore, the gold cap plays an important role in the EOT. Figure 3.20(b) presents the electric field distribution of Au-SiO<sub>2</sub>-microsphere monolayer that has a gap of  $g = 0.05 \mu m$ . The enhancement of the electric field is weaker than that of Au-SiO<sub>2</sub>-microsphere monolayer with a gap of  $g = 0 \mu m$ , and the transmitted light is less, as summarized by the results in Figure 3.15. Consequently, the electric field enhancement between the spheres facilitates the EOT in the IR region.

Next, electric field distribution profiles at the substrate surface (z=0) are also presented. The profiles of Au-SiO<sub>2</sub> microsphere monolayers forming a square lattice and a hexagonal lattice are shown in Figure 3.21(a) and Figure 3.21(b), respectively. The microspheres are attached ( $g=0~\mu m$ ) and excited by light at a wavelength of 16  $\mu m$ , polarizing in x direction. The electric field is localized at the thin gold films diamond-shaped (a) and triangle (b). Hence, light passes through the gaps between the Au-SiO<sub>2</sub> microspheres and passes through the thin gold films on the substrate.

#### 3.6 CONCLUSION

In this chapter, the optical property of  $SiO_2$  microspheres was investigated. The  $SiO_2$  particles express high emissivity in the IR region because of the SPhP resonance. The 20  $\mu$ m-diameter  $SiO_2$  beads deposited on the glass sample behaves like a nearly perfect thermal blackbody with an emissivity almost unity for all wavelength beyond 2.5  $\mu$ m. The

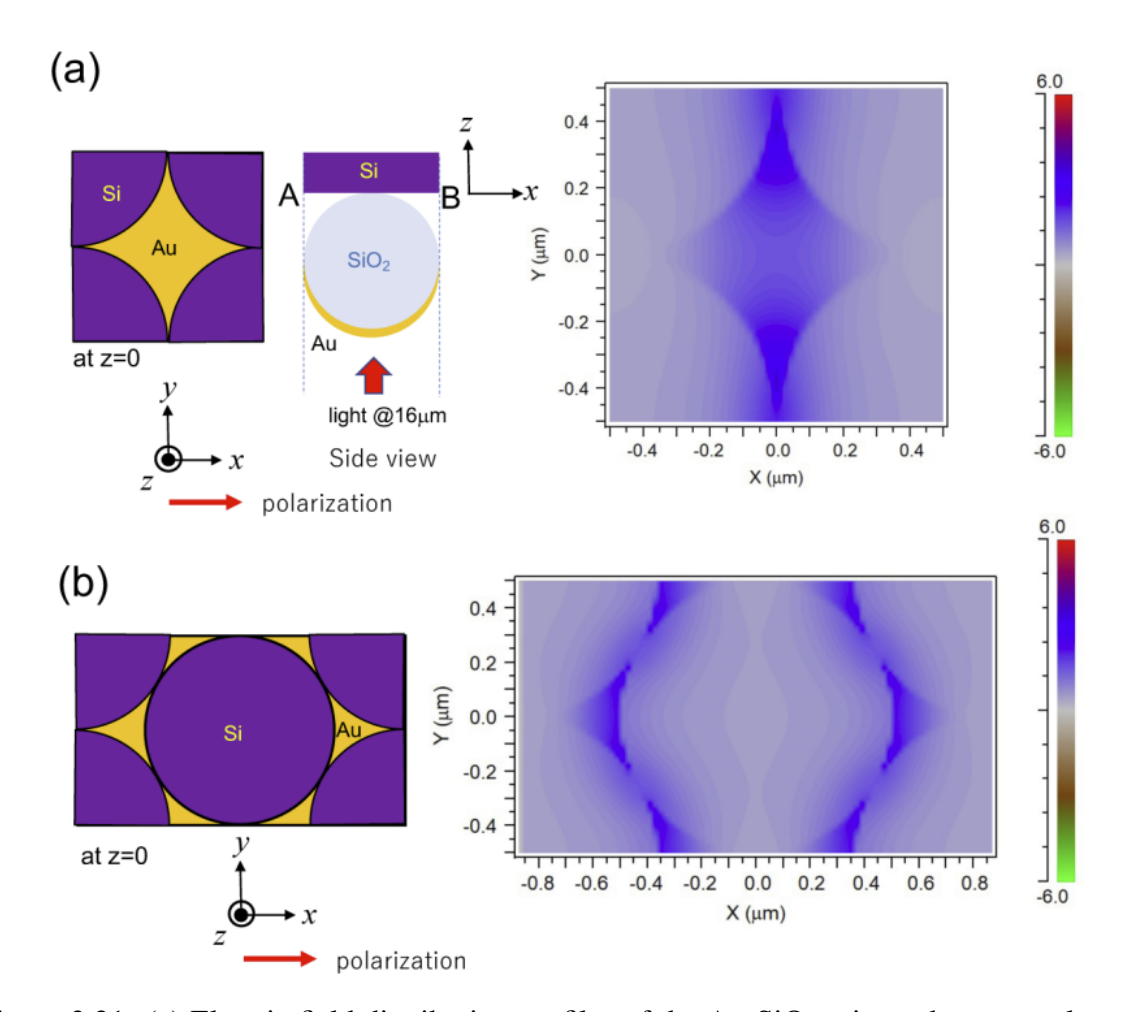


Figure 3.21: (a) Electric field distribution profiles of the Au-SiO<sub>2</sub> microsphere monolayer forming a square lattice (a) and a hexagonal lattice (b), where the microspheres are attached  $(g=0~\mu\text{m})$ , and excited by light at a wavelength of 16  $\mu\text{m}$ . Both electric field distributions in the cut plane at z=0, at the substrate surface.

result indicates that the  $SiO_2$  particles/glass structure is a good candidate for RC materials. At the same time, the EOT phenomena in Au- $SiO_2$ - and Au-PS-microsphere monolayers in the IR range from 5 to 25  $\mu$ m, are explored. The observed transmittance is significantly more excellent than that of the flat gold film with the same thickness, although the surface of the Au- $SiO_2$  microsphere monolayer appears to be covered entirely with gold films when observed from above. The FDTD calculation indicates that light passes through the openings between the gold film on the substrate surface and the gold cap. The EOT occurs in a wide wavelength range of the IR, indicating that the EOT is not attributed to the resonance of the surface plasmons in a metal. This type of EOT is absent in the visible and near-IR

wavelength range, where gold does not function as an ideal metal.

#### **CHAPTER 4**

#### TRANSPARENT MATERIALS FOR DAYTIME-RADIATIVE COOLING

#### 4.1 BACKGROUND

This chapter presents that the transparent polyester and lumiflon are candidates for day-time RC materials. Polyester polymers are polyethylene terephthalate (PET) and polyethylene naphthalate (PEN). Lumiflon is developed by AGC company, called LUMIFLON<sup>TM</sup> (solvent-soluble fluoroethylene and vinyl ether (FEVE) resins). From now on, lumiflon will be referred as LF. Their RC performance was also compared with reported daytime RC materials such as polyethylene (PE), polydimethylsiloxane (PDMS), soda-lime glass (glass), and  $20~\mu$ m-diameter silica particles on the glass (particles/glass). While some daytime-RC materials have been reported, our material, LF, can use in the form we prefer, such as films or paint. In addition, it has the weather-ability. Thus, it is promising for real applications such as cooling buildings and solar cells.

#### 4.2 EXPERIMENT

#### 4.2.1 Polyesters samples

The PET and PEN films used in this study were Lumirror (T60, Toray) and Teonex (Q51, Teijin). The thicknesses of both films were  $250 \,\mu\text{m}$ . Figure 4.1 presents images of polyester polymers. Depending on their processing and thermal history, polyester polymers may exist as amorphous (transparent) and semi-crystalline polymers. Therefore, PET is transparent while PEN is opaque.

Figure 4.2 presents the chemical structures of polyester polymers [93, 94].

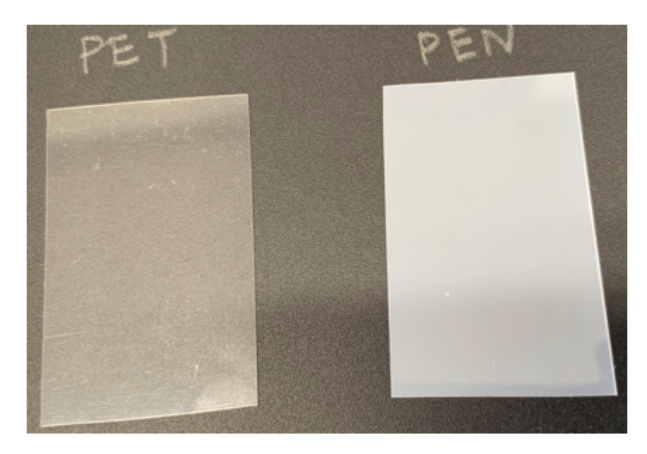


Figure 4.1: Image of (a) 250  $\mu$ m-thick PET, and (b) 250  $\mu$ m-thick PEN films.

(a)
$$\begin{bmatrix}
0 & & & & & & & & & & \\
U & & & & & & & & & \\
C & & & & & & & & & \\
C & & & & & & & & \\
C & & & & & & & & \\
C & & & & & & & \\
C & & & & & & & \\
C & & & & & & & \\
C & & & & & & & \\
C & & & & & \\
C & & & & & & \\
C & & & & \\
C & & & & \\
C & & & & \\
C & & & & \\
C & & & & & \\
C & & & & & \\
C & & \\$$

Figure 4.2: Chemical structures of (a) PET, and (b) PEN films.

# 4.2.2 Lumiflon samples

Figure 4.3 presents the chemical structure of LF as provided by AGC company [95]. LF includes fluoroethylene and vinyl ether; thus, it has properties of both fluoropolymer and hydrocarbons. The fluoroethylene group makes LF has the weather-ability and is resistant to UV degradation because C-F bonding is strong. The vinyl ether group makes LF has a paint-ability. Without the vinyl ether group, the polymer would not be soluble in solvents. Vinyl ether groups also contribute to a high gloss LF. Therefore, the LF polymer is a commercial polymer that has been used to protect many substrates such as concrete and plastic. Figure 4.4 presents the photo images of the LF power and the LF solution. In this study, the LF powder was dissolved in toluene solvent with ratio of 0.25 g/mL and 0.1 g/mL. Four

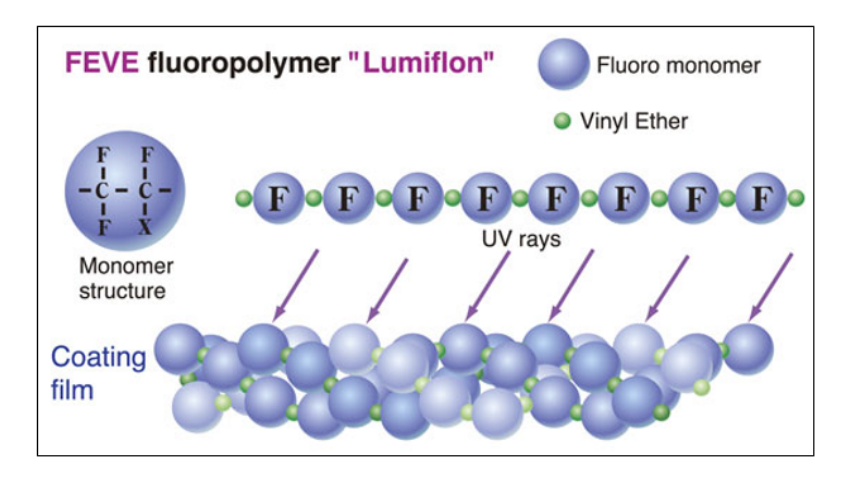


Figure 4.3: Chemical structure of LF [95].

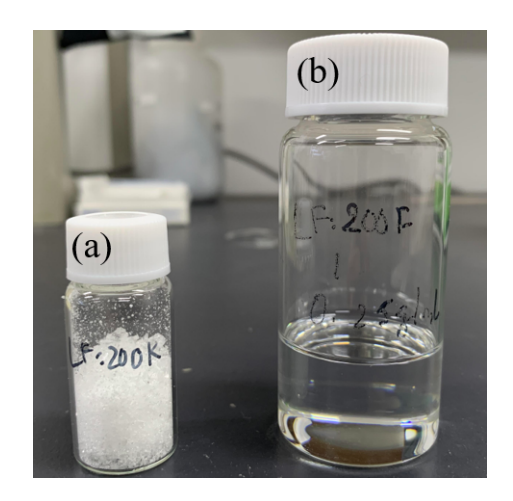


Figure 4.4: Photo images of (a) LF powder, and (b) LF solution after toluene dissolution. different substrates were used.

- 1. The silicone wafer substrate (P-type, high resistance, crystal orientation: 100) was used to estimate a film thickness by cross-sectional scanning electron microscope.
- 2. The glass was used as the RC material reference. It was also used as the substrate to measure the sample's transmittance in the visible region and the temperature reduction field setup.
- The glass-coated both sides by the 100 nm-thick gold film was utilized to confirm
  the spectral reflectance of polymers in the IR region and to support the in-house RC
  measurement.

4. The glass is coated on one side by the 100 nm-thick Ag film to conduct the field RC measurement.

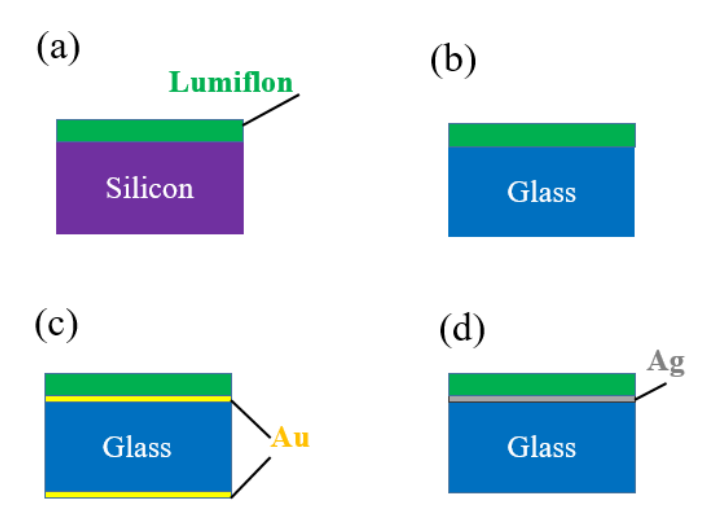


Figure 4.5: Substrates were used in this study are (a) silicon, (b) glass, (c) glass coated on both sides by a 100 nm-thick gold film, and (d) glass coated by a 100 nm-thick silver film.

Substrates with a dimension of 38 x 26 mm<sup>2</sup> were chemically and thermally treated based on the following procedure to remove the surface contamination. Substrates were washed with an aqueous solution of Extran MA 02 (Merk), pure water, and isopropanol, dried by a hairdryer, and cleaned in an Ozone cleaner. The evaporation technique was used to deposit Au or Ag films.

The drop-cast method was applied to propose the LF film on a substrate. The substrate was placed on a flat plate to allow uniformity in the film thickness. Carbon tapes were used as a wall with 200  $\mu$ m in thickness to avoid spreading out of the solution. The volume of the polymer solution changed the thickness of the LF film. For 50  $\mu$ m and 100  $\mu$ m-thick polymer, 0.65 mL and 0.9 mL of a 0.25 g/ml-solution dropped on the substrate, respectively. Then, samples were dried at room temperature. For a 200  $\mu$ m-thick polymer, the fabrication process of 50  $\mu$ m-thick polymer was repeated four times. For the polymer with a thickness less than 50  $\mu$ m, the solution with a ratio of 0.1 g/mL was used. The dropped volumes of 0.13 and 0.5 mL were 12 and 25  $\mu$ m-films, respectively. Cross-sectional SEM images were used to evaluate the thickness of thick films.

The drop-casting method is not fit for fabricating a thin film. Thus, the thin LF film was prepared by the spin coating method. After setting the substrate on the disk of the spin-coater, the coating solution with a ratio of 0.25 g/mL (approx. 0.4 ml) was dropped and spin-coated at 500 rpm for 30 seconds in the air. Then the sample was dried on a hot plate at 100 °C for 20 min. The thickness of the thin samples was estimated from the interference peaks in reflectance spectra. By various fabrication methods, LF films with different thicknesses such as 4, 12, 25, 50, 100, and 200  $\mu$ m, were obtained.

## 4.2.3 Reference samples

The PDMS film was made on the glass substrate using an elastomer and a curing agent (SYLGARD 184, Dow) with a mixing ratio of 10:1. The mixture was stirred for 10 min and kept in a refrigerator for one hour to remove air bubbles. For 350  $\mu$ m-thick PDMS, approximately 2 ml of the mixed solution was dropped on the substrate. Then, the samples were dried at room temperature for five days. For the 250  $\mu$ m-thick PDMS film, after dropping the solution on the substrate, the sample was spin-coated at 400 rpm for 15 s. Finally, it was dried in the oven at 70°C for 24 h. The cross-sectional SEM images evaluated the film thickness.

The particles/glass sample was fabricated by the spin-coating method. The fabrication process explained in Chapter 3.

The PE film with thicknesses of 25, 125, 275, and 400  $\mu$ m was used. Unfortunately, only the 25  $\mu$ m-thick PE film was available; thus, multi-layers were stacked to get thick samples.

### 4.2.4 Material characterization

The transmittance spectra from 400 nm to 750 nm were obtained with a spectrometer (MCPD 3000, Otsuka Electronics Co. Ltd.) using a halogen lamp as the light source. In addition, the transmittance spectra in the near-IR region (750 to 1100 nm) were obtained

by Hitachi UV-Visible (U-2810) spectrophotometer. The reflected and transmitted infrared spectra were measured using the FTIR spectrometer. The spectral range was between 400 cm<sup>-1</sup> to 4000 cm<sup>-1</sup>, with a resolution of 2 cm<sup>-1</sup>. The diameter of the incident light was set at 5 mm using an aperture. References were taken with ambient air and an Al mirror to measure the transmittance and reflectance spectra. According to Kirchhoff's law of thermal radiation, emissivity E is equal the absorptivity E. Therefore, E could be evaluated using E = A = 1 - T - R, where E and E are the transmittance and reflectance, respectively.

## 4.2.5 In-house setup for temperature measurement

Any objects exposed to the sky are affected by solar radiation, atmosphere, and surrounding objects such as buildings, trees, etc. Therefore, the in-house experiment was conducted to avoid those as the first step.

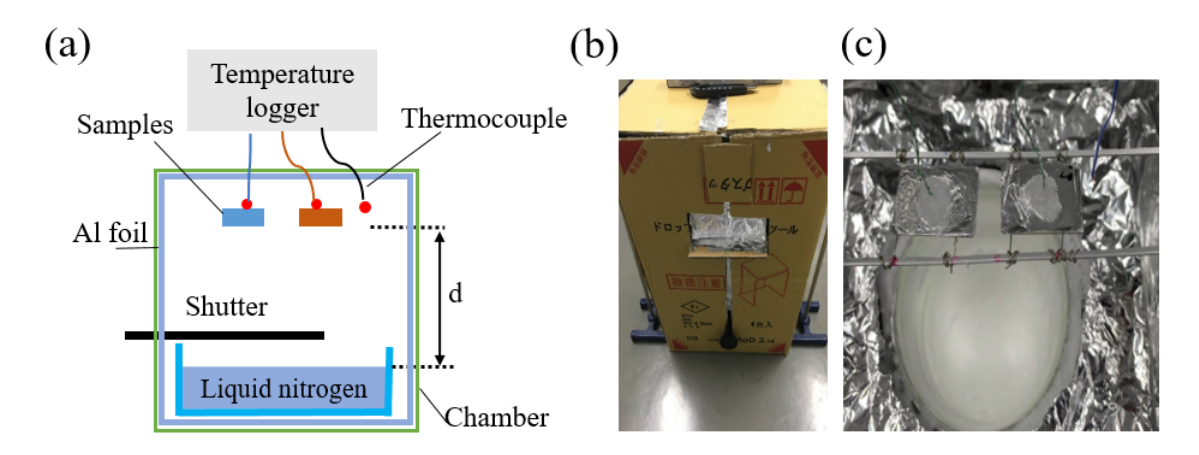


Figure 4.6: (a) Schematic for in-house measurement, (b) and (c) Images of a chamber and the sample's holder, respectively.

The schematic setup for confirming the dropped temperature of materials is presented in Figure 4.6(a). The chamber was made of a packaging box of 45 cm  $\times$  45 cm  $\times$  60 cm. The inner surface of the chamber was covered with an Al foil to prevent surface thermal emission. A glass Dewar vessel filled with LN at 77K was used for refrigeration by absorbing thermal radiation from the sample. The sample was set above the vessel, exposing its surface to LN. Thermocouples were placed in the following positions: near the

sample to measure the ambient temperature and the backside to measure the temperature of the sample. Silicone grease was used to ensure the contact between the thermal couples and samples. Three distances between the sample and the LN surface (d) were examined to reveal the divergence of the emission from the sample.

The experiment was conducted with five steps. First, the sample was separated from LN using the shutter covered with an Al sheet. Then, in the second, third, and fourth steps, the shutter was removed, and the sample surface was exposed to LN at d=23, 19, and 16 cm, respectively. Finally, the sample was separated from the LN again. The temperature drop  $\Delta T$  was evaluated by the difference between ambient temperature in the first step,  $T_{\rm a}$ , and the sample temperature,  $T_{\rm s}$ , using the equation  $\Delta T = T_{\rm a} - T_{\rm s}$ .

# 4.2.6 Field setup for temperature measurement

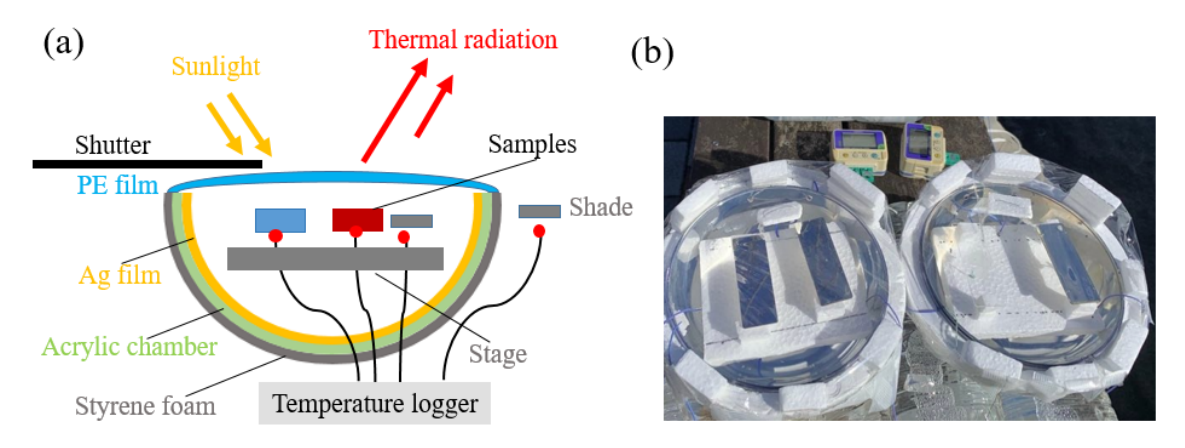


Figure 4.7: (a) Schematic for field temperature measurement, (b) Photograph of the chamber and samples.

Figure 4.7(a) presents the schematic of the experimental field setup. The experiment was conducted in the parking area of Suzukakedai campus, Tokyo Institute of Technology, Japan. The experiment chamber is a clear acrylic hemisphere with a diameter of 17 cm. The inner surface of the chamber was coated with a 100 nm-thick Ag film by the evaporation method. The outer of the chamber is covered by the PS foam. The objective is to reflect the sunlight and to avoid parasitic heating. The thin PE film was used to reduce the affection

of wind. The samples were fixed on the PS foam with a low thermal conductivity to reduce the conduction loss. Thermocouples were placed at (1): the surface of each sample to record their temperature, (2) inside the chamber, and (3) outside the chamber to monitor the surrounding ambient temperature. Under the sunlight, the silicone grease was heated up and melted; rice was used to connect the thermocouples and the samples. The PS foam covered the thermocouples of ambient air to block its thermal radiation and sunlight absorption.

The experiment process has three steps. Firstly, the shutter was used, and samples were not exposed to the sky. Secondly, the shutter was removed. Thirdly, the shutter was used, and the experiment was finished.

#### 4.3 RESULTS OF POLYESTER

# 4.3.1 Optical property

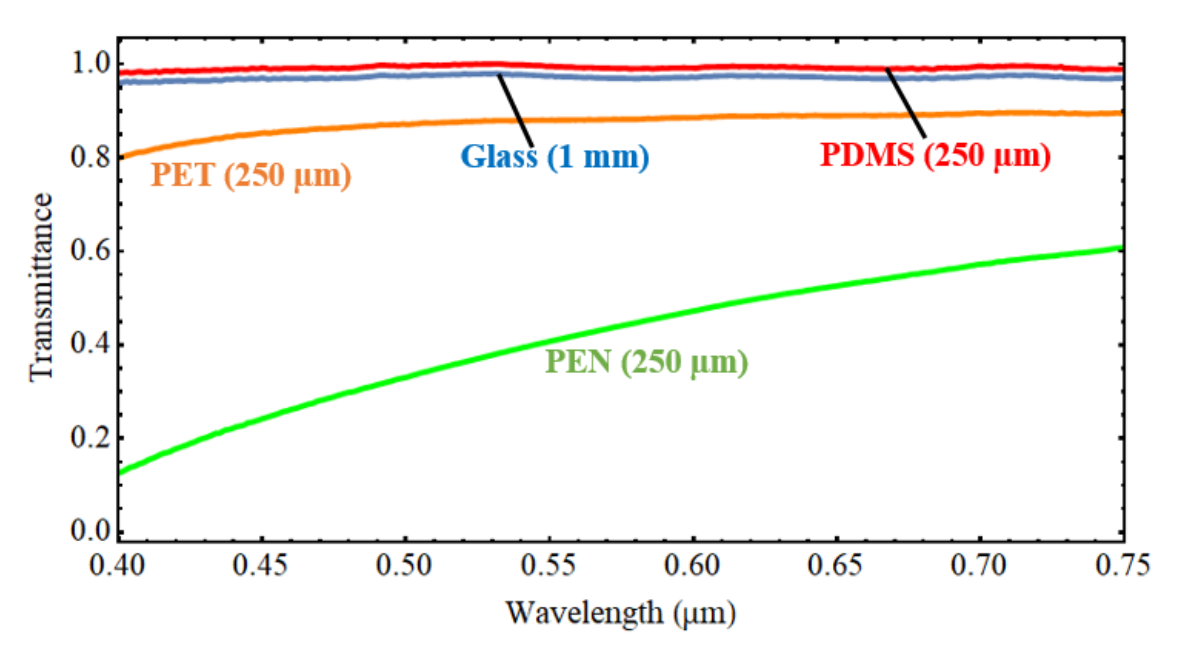


Figure 4.8: Visible transmittance spectra of the samples: PDMS, PET, PEN films, and the glass plate. The thickness is given in parentheses.

Figure 4.8 presents the transmittance spectra of the PDMS, PET, and PEN films, and the glass plate in the visible region, with the thicknesses of each film and plate given in

parentheses. The transmittance of the PET film is approximately 90% over the visible region, which is nearly identical to the PDMS film, and a glass. However, the PEN film is oblique, and its transmittance is low due to light scattering. High transmittance in the visible region is necessary to avoid losing solar energy for daytime RC materials in solar cell refrigeration; thus, the PET film was considered an excellent alternative to the PDMS film and the glass plate. Table 4.1 summarizes the transmittance of the materials averaged over the visible region of 0.4– $0.75~\mu m$ .

Table 4.1: Summary of optical properties of polyester polymers, and reported daytime RC materials. Averaged transmittance in the visible region, ( $\lambda = 0.4$ -0.75  $\mu$ m), and averaged emissivity in the ATW region, ( $\lambda = 8$ -13  $\mu$ m).

Materials	PET	PEN	PDMS	Glass
	$(250~\mu\mathrm{m})$	$(250 \ \mu \mathrm{m})$	$(250 \ \mu m)$	(1 mm)
T in Vis	0.87	0.39	0.99	0.97
E in ATW	0.9	0.9	0.95	0.84

Figure 4.9 presents the emissivity spectra of the PDMS, PET, and PEN films and the glass plate. The mean emissivity over ATW is summarized in Table I. The spectra of both polyesters, PET and PEN, were similar. At the ATW wavelengths, the emissivity of both the polyester films was approximately 90% due to the vibration of the ring in the plane C-H bond and ester C(O)-O modes at 7.7–10 μm (1300–1000 cm<sup>-1</sup>). It was nearly identical to the PDMS film and the glass plate, which are widely used materials for daytime RC [83]. In addition, the emissivity of the films was lower at wavelengths other than ATW, suggesting that the polyesters were less susceptible to the influence of blackbody radiation from the surroundings.

### 4.3.2 In-house RC measurement

The RC efficiency of the polyester polymer was measured using the setup depicted in Figure 4.6. The PET film and ambient temperatures were measured simultaneously, and the results have been plotted in Figure 4.10(a). After removing the shutter at 30 minutes, the

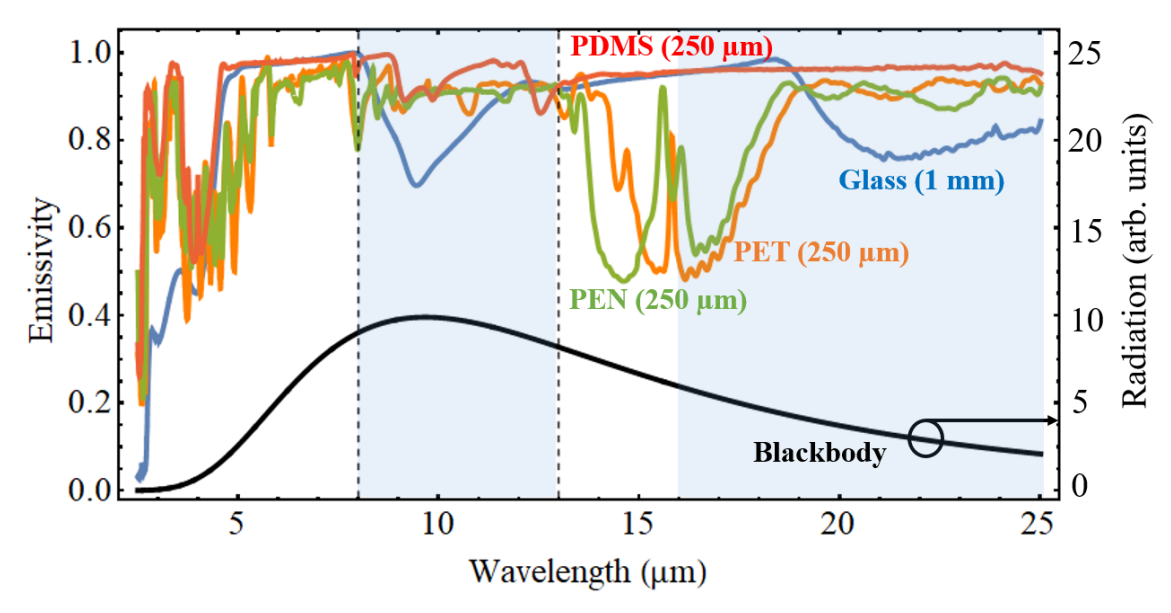


Figure 4.9: Emissivity spectra of the samples: films of PDMS, PET, and PEN; glass plate; and the blackbody radiation spectrum at 300 K. The hatched areas indicate the ATW.

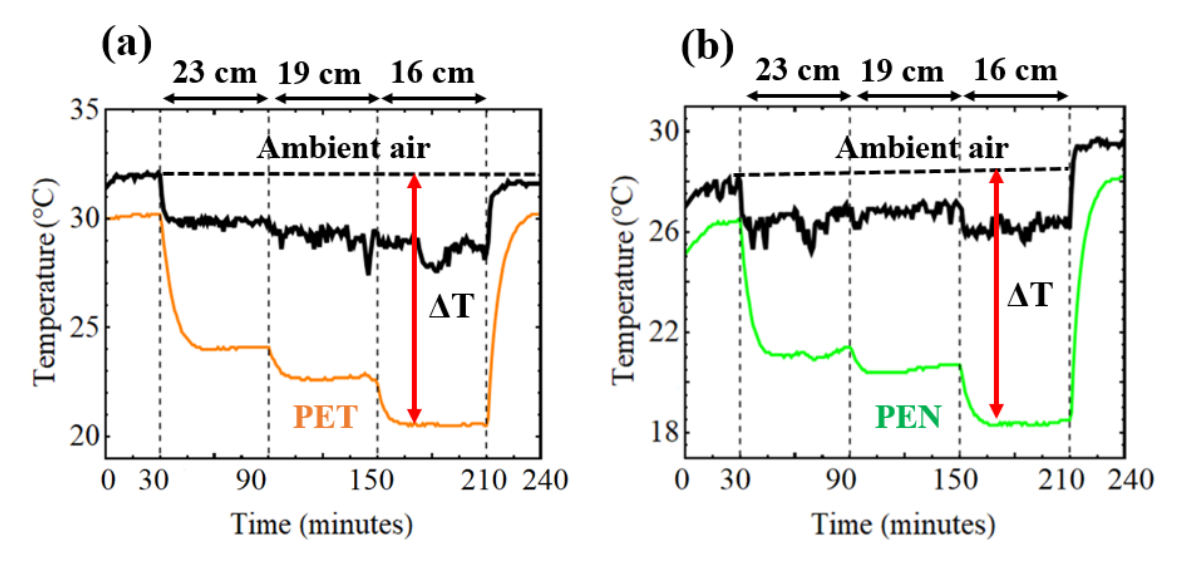


Figure 4.10: Measured temperature between ambient air and (a) 250  $\mu$ m-thick PET, (b) 250  $\mu$ m-thick PEN films.

PET film temperature dropped, in addition to an initial slight drop in the ambient temperature due to the RC of the thermal couple. Therefore, the line connecting the ambient temperature at 30 minutes to 210 minutes was used as the baseline. In the initial state at time 0-30 minutes, the temperature of PET is 2 °C lower than ambient temperature. This dropped temperature is due to the RC of the film to be cooled lid placed above the LN. After the initial drop, the ambient temperature remained nearly constant. The temperature

reduction of a 250  $\mu$ m-thick PET film is presented in Table 4.2. The dropped temperature of the samples increases with decreasing the distance.

Table 4.2: Temperature reduction of a 250  $\mu$ m-thick PET film at different distance between the sample and LN, d, measured and calculated, in the in-house measurement.

Distance d (cm)	23	19	16
Measured (°C)	$6.6 \pm 0.6$	$7.3 \pm 0.9$	$9.3 \pm 0.8$
Calculated (°C)	4.3	6.1	8.0

Table 4.3: Temperature reduction of a 250  $\mu$ m-thick PEN film at different distance between the sample and LN, d, measured and calculated, in the in-house measurement.

Distance d (cm)	23	19	16
Measured (°C)	$6.1 \pm 0.8$	$7.0 \pm 0.9$	$9.3 \pm 0.9$
Calculated (°C)	4.2	6.0	8.0

In the in-house experiment, the dropped temperature of the 250  $\mu$ m-thick PEN film, as displayed in Figure 4.10(b), and Table 4.3, was similar to PET.

Next, Table 4.4 summaries in-house  $\Delta T$  for samples at d = 16 cm, including 250  $\mu$ m-thick PET, 250 $\mu$ m-thick PEN, 250  $\mu$ m-thick PDMS films, and 1 mm-thick glass plate. The performance of the polyesters polymers is as high as that of the PDMS film and the glass substrate.

Table 4.4: The temperature drop ( $\Delta T$ ) of various materials with error bar at d=16 cm.

Materials	PET	PEN	PDMS	Glass
	$(250~\mu\mathrm{m})$	$(250 \ \mu m)$	$(250~\mu\mathrm{m})$	(1 mm)
Measured (°C)	$9.3 \pm 0.8$	$9.3\pm0.9$	$10.3 \pm 0.7$	$9.5 \pm 1.1$
Calculated (°C)	8.0	8.0	9.0	8.4

Although PEN portrayed an RC efficiency that was similar to PET, its transmittance was only 39% in the visible region due to crystallization. Therefore, while PEN is suitable for daytime RC, it is unsuitable for solar cell refrigeration. However, according to the datasheet, PEN can be made transparent by choosing an appropriate manufacturing method. By

manufacturing a transparent PEN, we can obtain another suitable alternative for solar cell refrigeration.

While PET is a crystalline polymer, its crystallization temperature is relatively high (140-200 °C). In addition, its glass transition temperature was reported to be 70°C [96]; the possible effects of crystallization and obliqueness were not considered at temperatures lower than the glass transition temperature. In addition, PET can be manufactured as fibers and used as a textile for daytime RC. Therefore, PET has multiple advantages over other RC materials in optical transparency and mold-ability.

# 4.4 RESULTS OF LUMIFLON

# 4.4.1 Optical property

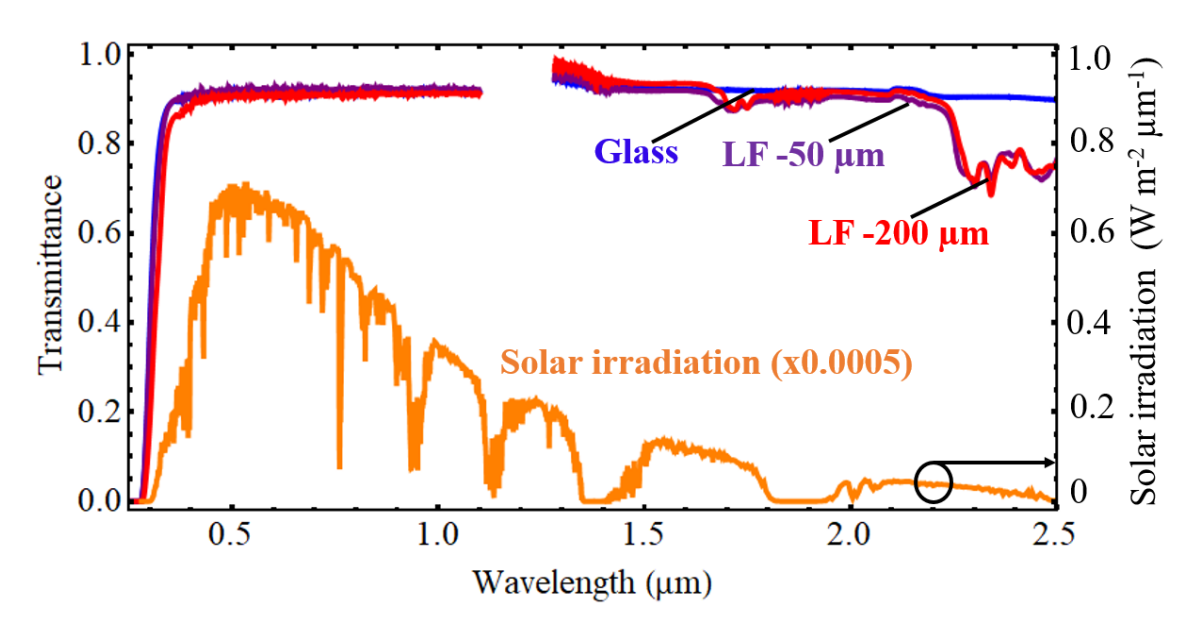


Figure 4.11: Transmittance of LF films on the glass substrate and the solar irradiance. The thicknesses of the film are 50  $\mu$ m and 200  $\mu$ m. Note that the solar irradiance is multiplied by 5 x  $10^{-4}$ .

Figure 4.11 presents the transmittance spectra of the LF on the glass substrate in the visible and near IR regions. The spectrum in the wavelength range of 0.25 to 1.1  $\mu$ m and 1.28 to 2.5  $\mu$ m was obtained by Hitachi UV-Visible (U2810) and FTIR-4600, JASCO spectrometer, respectively. The equipment to measure the transmittance in the wavelength

range of 1.1 to 1.28  $\mu$ m is not available in our group. Results of the LF film with different thicknesses of 50 and 200  $\mu$ m are presented in purple and red lines. The transmittance spectrum of the glass substrate is presented as the reference. The solar irradiance at an air mass of 1.5 is plotted, reduced to 1/20000 of its original. Since the air spectrum was used as the baseline, the transmittance is 0.08 lower than unity due to the reflection at both sample surfaces, even in the case of no absorption. At  $\lambda = 0.55~\mu$ m, at the peak of the solar irradiation, the transmittance and reflectance are 92% and 8%; thus, the LF film are free from sunlight. In the near IR region ( $\lambda = 2$ -2.5  $\mu$ m), because of absorption, the transmittance of LF is lower, approximately 80%. In addition, the solar irradiation in this range is less, which is only 0.3% in total sunlight radiation. Thus, the absorption of LF films under sunlight is not significant.

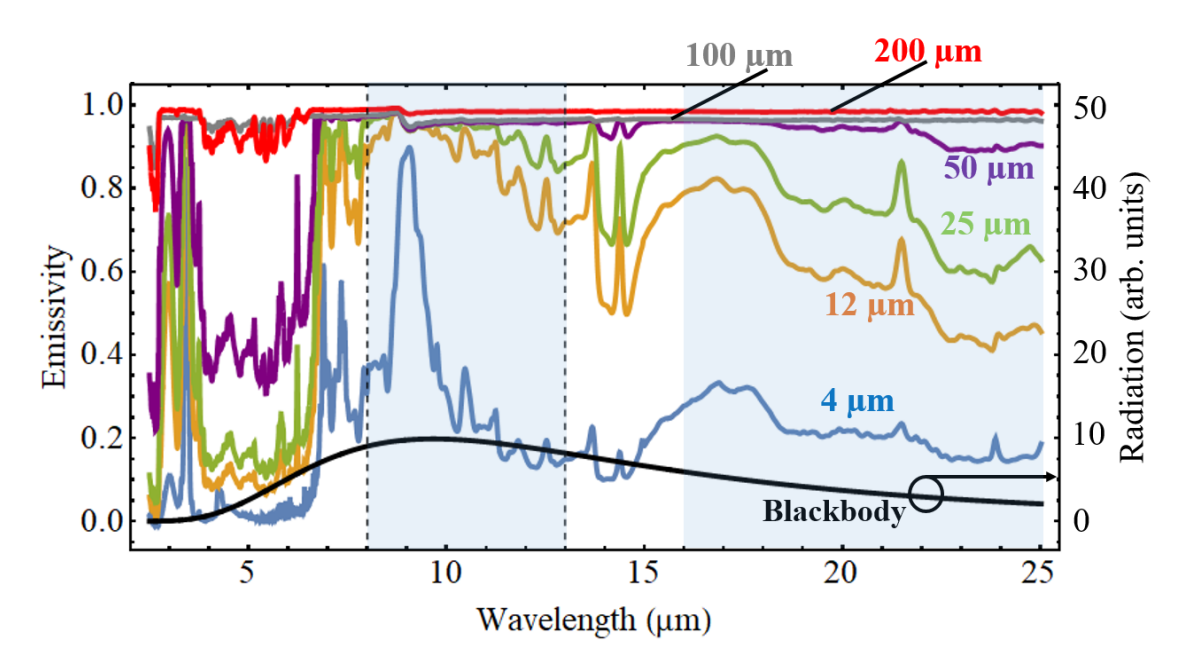


Figure 4.12: Emissivity spectra of LF films with thicknesses of 4, 12, 25, 50, 100 and 200  $\mu$ m in the IR wavelength range (2.5-25  $\mu$ m). Numbers in parentheses indicate film thickness. The hatched areas indicate the ATW.

Figure 4.12 presents IR emissivity spectra of the LF films on the glass-coated in both sides by 100 nm thick gold films. The emissivity E = 1 - R, where R is reflectance, and the transmittance of samples is zero. The thickness of the LF film is 4, 12, 25, 50, 100, and

 $200 \ \mu m$ . Cross-sectional SEM images observed the film thickness more significant than 25  $\mu m$ . The thickness of thinner films is estimated by the interference of visible reflectance spectra. The detail will be explained in Appendix C.

Absorbed in the spectrum of the 4  $\mu$ m-thick LF film, there is a strong vibration band of carbon-fluorine bond, located at 9.1  $\mu$ m (at a wave-number of 1100 cm  $^{-1}$ ). In the thick films, the tail of this peak covers the ATW wavelength (8-13  $\mu$ m), giving a high emissivity in this wavelength region. Another broad and weak peak at 16.5  $\mu$ m covers another ATW wavelength (16-25  $\mu$ m) in thick films.

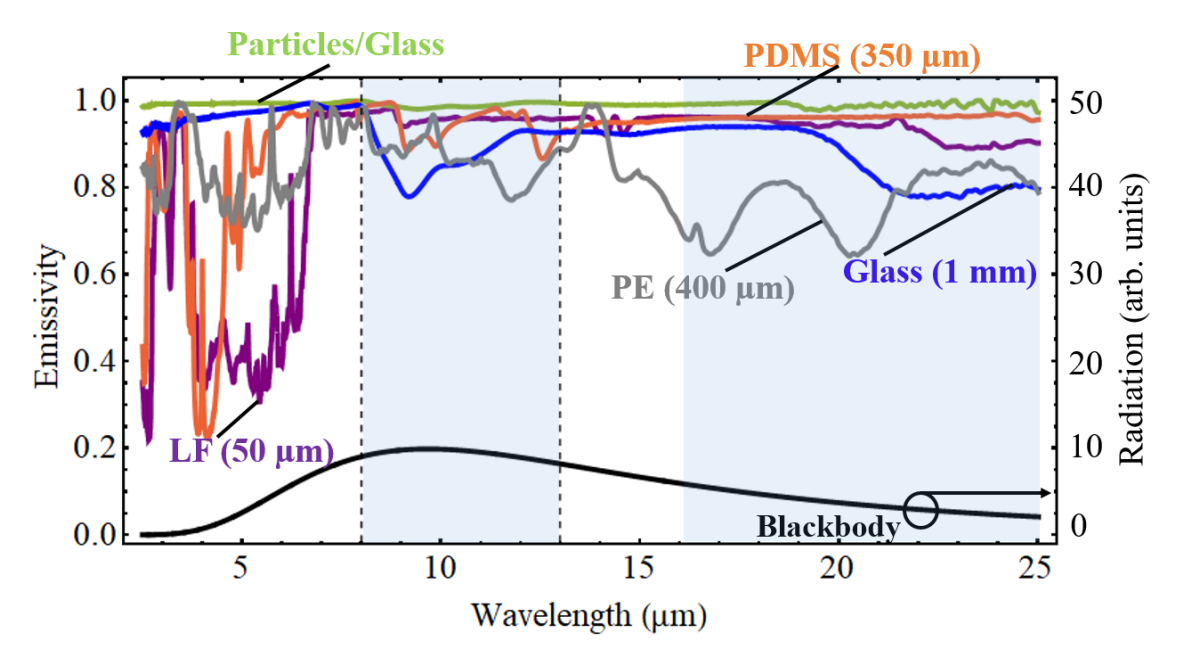


Figure 4.13: Emissivity spectra of various samples in the IR wavelength range (2.5-25  $\mu$ m), including a 350  $\mu$ m-thick PDMS, a 50  $\mu$ m-thick LF, a 400  $\mu$ m-thick PE, a 1 mm-thick glass, 20  $\mu$ m-diameter SiO<sub>2</sub> particles on the glass. Numbers in parentheses indicate film thickness. The hatched areas indicate the ATW.

Figure 4.13 presents IR emissivity spectra of samples, which are the 350  $\mu$ m-thick PDMS, the 50  $\mu$ m-thick LF, the 400  $\mu$ m-thick PE films on the gold substrate, a 1 mm-thick glass, and silica particles with 20  $\mu$ m in diameter on the glass substrate. The PDMS film presents high emissivity in the wavelength range of 8-13  $\mu$ m, which is consistent with the published results [28]. The emissivity of glass and particles/glass is nearly unity over the IR range of 2.5 to 25  $\mu$ m. However, the emissivity of the LF film is high in the range

of 7-25  $\mu$ m, and low at the wavelengths of 5-7  $\mu$ m. Since 7% of the blackbody radiation energy lies in this wavelength range, LF is less affected by the thermal radiation from the atmosphere.

# 4.4.2 In-house RC measurements

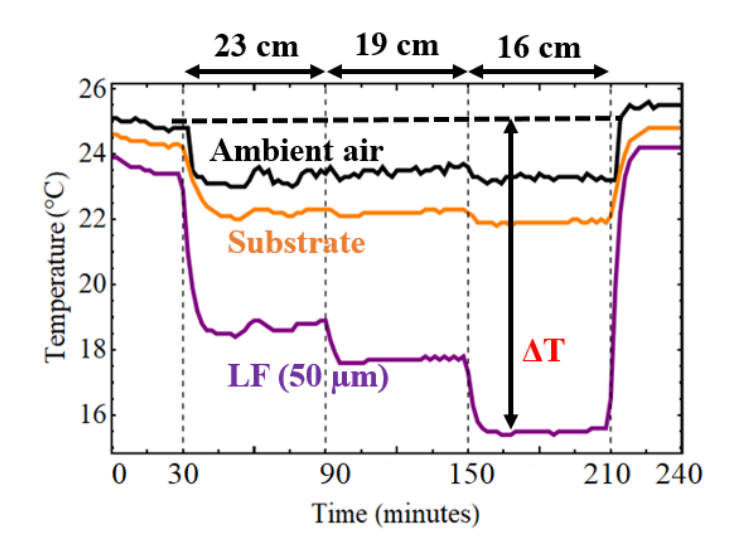


Figure 4.14: Measured temperature of ambient, a glass coated both sides by 100 nm-thick gold films (substrate), and a 50  $\mu$ m-thick LF film. The shutter opened at 30 min, and the gap between the sample and the LN were changed to 23, 19, 16 cm, in order.

Figure 4.14 presents the in-house RC measured result of a 50  $\mu$ m-thick LF film, and the substrate. When the shutter opened at 30 min, an immediate decrease in the ambient temperature was observed. The decrease in temperature immediately recovered upon closing the shutter at 210 min. The line connecting the ambient temperature at 30 minutes to 210 minutes was used as the baseline to evaluate the temperature reduction,  $\Delta T$ , similar to the estimated way of polyester polymers. The largest temperature drop of the LF film was observed as 8.9°C at d=16 cm, whereas the dropped temperature of the substrate is only 3°C.

Table 4.5 presents the temperature reduction of the 50  $\mu$ m-thick LF film. Similarly as the polyester polymer, the dropped temperature increases with d decreases. The calculated temperature drop is also listed.

Table 4.5: The temperature drop ( $\Delta T$ ) at different distance between the sample and LN, d, measured and calculated results, in the in-house measurements.

d (cm)	16	19	23
Measured (°C)	$8.9 \pm 0.8$	$6.9 \pm 0.5$	$6.0 \pm 0.8$
Calculated (°C)	8.6	6.5	4.6

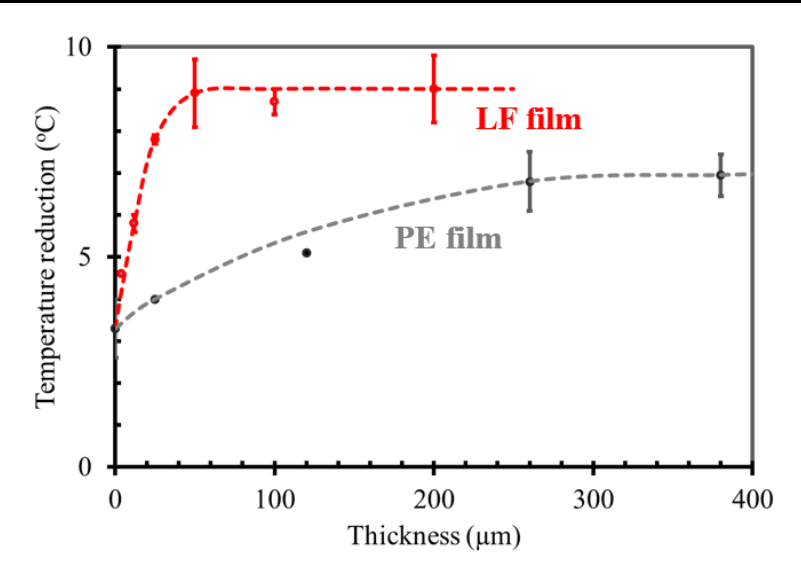


Figure 4.15: Measured temperature reduction by the in-house experiments, as the function of thickness of LF and PE films. The distance of samples and the LN is fixed at d = 16 cm. The dashed line is a guide to eyes.

Figure 4.15 presents the temperature reduction as a function of the thickness of LF and PE films. All samples are coated on the gold substrate. The RC performance of four stacked PE films was measured to compare its efficiency with the LF film. The emissivity of PE films is explained in Appendix D.

The temperature reduction increases with increasing the film thickness. In the case of the LF film, the temperature drops saturated at 50  $\mu$ m, which means a thickness of 50  $\mu$ m is thick enough. On the other hand, the temperature reduction of PE films is lower than LF films, which is become constant at 300  $\mu$ m in thickness. The 25  $\mu$ m-thick PE film shows the low RC efficiency because of the absence of active vibration modes in the ATW wavelengths. Therefore, it is used as the cover for the chamber in field RC measurement. However, PE films with thickness exceeding 100  $\mu$ m micros have a absorption in the ATW because of the absorption tail of the = C–H (flexural) at  $\lambda$  = 11.1-14.5  $\mu$ m, and C=C (vi-

bratory) at  $\lambda = 6.25$ -6.7  $\mu$ m [97]. The measured and calculated results of the different LF thickness are presented in Table 4.6.

Table 4.6: The temperature reduction  $\Delta T$ , at the different thicknesses of the LF film, measured and calculated results, in the in-house RC measurement at distance d = 16 cm.

Thickness (μm)	Measured (°C)	Calculated (°C)
0	$3.3 \pm 0.7$	_
4	$4.6\pm0.7$	2.6
12	$5.8 \pm 0.2$	6.8
25	$7.8 \pm 0.1$	7.8
50	$8.9 \pm 0.8$	8.6
100	$8.7 \pm 0.3$	9.0
200	$9.0 \pm 0.8$	9.1

Table 4.7 presents the temperature reduction of various materials, which are 50  $\mu$ m thick LF, 350  $\mu$ m thick PDMS, 400  $\mu$ m thick PE, 1 mm thick glass, and SiO<sub>2</sub> particles/ glass. The good agreement of measured and calculated results is presented. The temperature reduction of LF, PDMS, glass are similar, which is higher than that of the PE film and lower than that of silica particles/glass. However, the LF film has some advantage points in compare to the other materials. (1) High transparent in the visible region. This feature makes the LF film suitable for applications that require light passing through the film, such as the cooling of solar cells. Also, the LF film does not change the appearance of the substrate, thus it can use to coat on the buildings. (2) The high RC performance can be obtained for the thin film, approximately 50  $\mu$ m thick film. (3) LF has already been used for painting buildings, and has weather-ability. (4) LF is solvent-soluble and paint-able.

## 4.4.3 Field RC measurements

The cooling performance of the LF film was characterized by measuring its temperature under sunlight and in the shade. Four samples were prepared: (1) 1 mm-thick glass substrate, (2) 100 nm-thick Ag film on the glass substrate (Ag substrate), (3) 50  $\mu$ m-thick LF film on glass, (4) 50  $\mu$ m-thick LF film on the Ag substrate.

Table 4.7: The temperature reduction,  $\Delta T$ , of various samples, including: LF, PDMS, PE, glass, particles/glass, measured and calculated results, in the in-house RC measurement at distance d=16 cm.

Samples	Measured (°C)	Calculated (°C)
LF (50 μm)	$8.9 \pm 0.8$	8.6
PDMS (350 μm)	$9.2\pm0.5$	8.9
PE (400 μm)	$7.0\pm0.51$	7.9
Glass (1 mm)	$8.7 \pm 0.7$	8.5
Silica particles (20 $\mu$ m)/ glass (1 mm)	$9.7\pm0.9$	9.2

Figure 4.16(a) presents the experimentally measured temperature of samples and ambient air during the noontime (from 10 AM to 2 PM) with a measurement time interval of 20 seconds. Following the fluctuation of the solar irradiance, the temperature of the samples fluctuated slowly with the time delay due to the finite heat capacity of the glass substrate. At 30 min, when the shutter was opened, the temperature dramatically rose with time, except for the outside ambient temperature. Because both the polystyrene stage and the Ag film coating inside the chamber absorb the sunlight. The LF film on the glass presents the lowest temperature concerning the ambient inside the chamber. This corresponds to the high RC efficiency of LF film and no sunlight absorption of both the glass and LF films.

Table 4.8: The temperature reduction  $\Delta T$  (°C), under the sunlight of the Ag film, the LF film on the Ag substrate, the LF film on the glass substrate, and glass substrate in the sun. The calculated temperature drop is also listed.

Samples	Ag film	LF on Ag	LF on glass	Glass
Measured	$3.8 \pm 1.2$	$8.6 \pm 0.9$	$11.9\pm0.8$	$8.1 \pm 0.9$
Calculated	0.0	7.3	8.6	8.2

Table 4.9: The temperature reduction  $\Delta T$  (°C), in the shade of the Ag film, the LF film on the Ag substrate, the LF film on the glass substrate, and the glass substrate. The calculated temperature drop is also listed.

Samples	Ag film	LF on Ag	LF on glass	Glass
Measured	$0.6 \pm 0.2$	$3.5\pm0.2$	$2.2\pm0.3$	$2.1 \pm 0.3$
Calculated	0.8	3.5	3.4	3.2

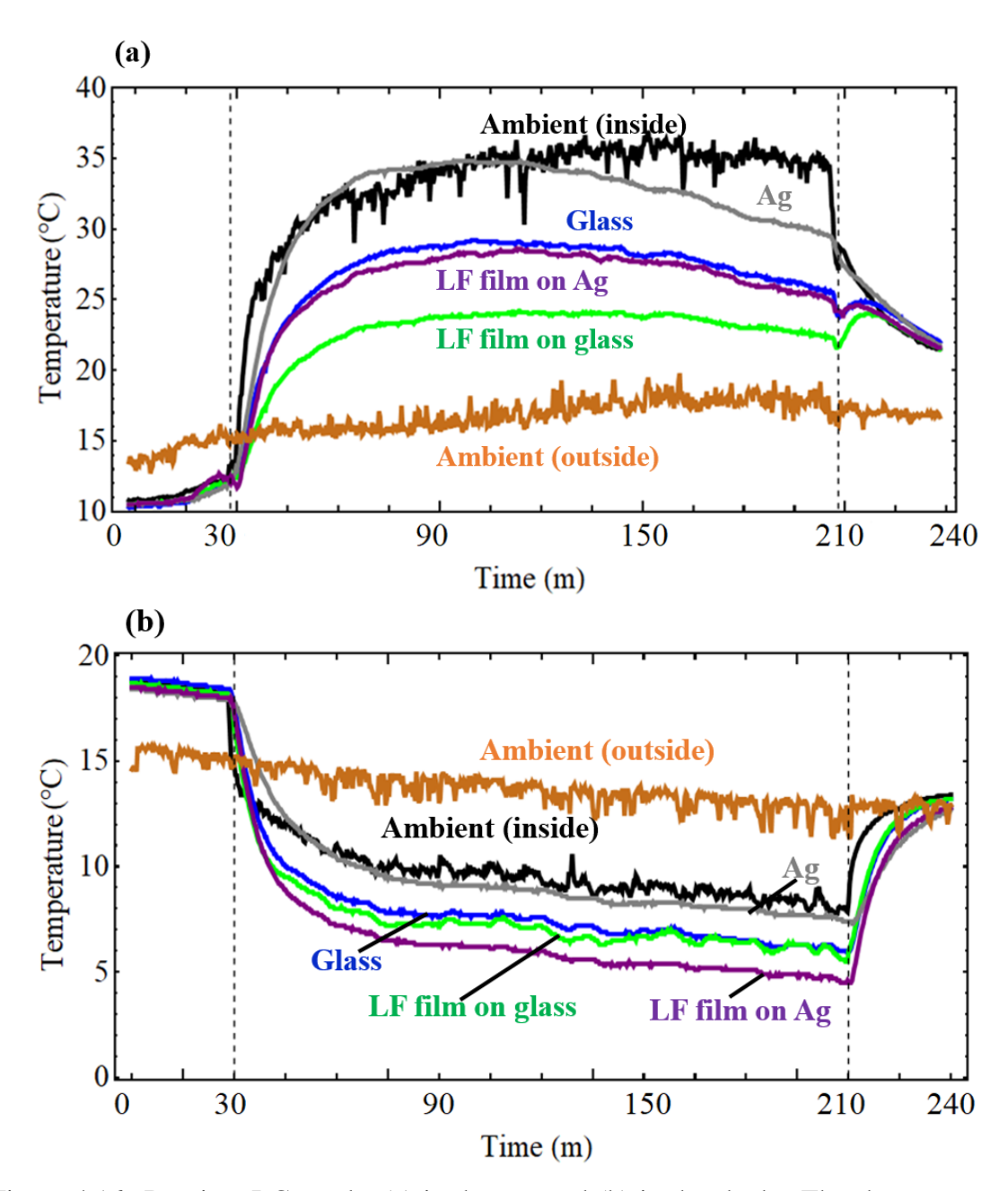


Figure 4.16: Daytime RC results (a) in the sun and (b) in the shade. The shutter opened from 30 min to 210 min. Samples are 100 nm-thick Ag film, 1 mm-thick glass substrate, 50  $\mu$ m-thick LF film on a glass and 50  $\mu$ m-thick LF film on Ag substrate. Temperature of ambient both inside and outside the chamber was recorded.

Samples at the next lowest temperature are the glass substrate and the LF on the Ag substrate. The glass substrate has high RC efficiency and high transparency; thus, the glass temperature is also lower than the ambient inside temperature. However, even the LF film has high RC performance, Ag absorbs a small sunlight. As a result, LF film on the Ag

substrate presents a higher temperature than the LF film on the glass substrate. In addition, Ag with the lowest RC efficiency; thus, its temperature is close to the ambient air inside the chamber. According to these results, the LF film shows higher RC efficiency than the glass substrate in the field measurement. In contrast, their results are similar to the in-house measurement. The reason may be that LF has low absorption in the wavelength range of 5-7  $\mu$ m, while the glass has high emission over this region. It means the absorption of the atmospheric thermal radiation of the LF film is lower than that of the glass.

Figure 4.16(b) presents the measured temperature of samples in the shade. The outside ambient temperature decreases with time because the experiments was measured in the afternoon (from 3:45 PM to 7:45 PM). In the shade, the temperature of ambient inside is lower than ambient outside, because of no solar absorption of the chamber. The temperature of a Ag film is similar to the inside ambient temperature, corresponding to the low RC efficiency. The temperature of a glass and the LF film on the glass are close, which are higher than that of LF on the Ag substrate. The result contributed that Ag works as the back-reflector of blackbody radiation.

The temperature reduction of samples under the sunlight and in the shade are presented in Table 4.8, and Table 4.9, respectively. The reference is the ambient inside the chamber. The averaged temperature was estimated at 150-210 min, with its standard deviation. Obviously, the measured temperature drops in the shade are significantly smaller than those in the sun. The reason is that the ambient inside is higher than ambient outside, under the sunlight, while, the relation is opposite in the shade.

Next, the RC performance of LF films with different thicknesses on the Ag substrate was examined. References are a 1 mm-thick glass substrate and the 100 nm-thick Ag film. The temperature both inside and outside of chamber were measured. The results are presented in Figure 4.17. The temperature reduction of samples in the sun and in the shade also shown in Table 4.10, and Table 4.11, respectively. The averaged temperature was calculated at 60-120 min.

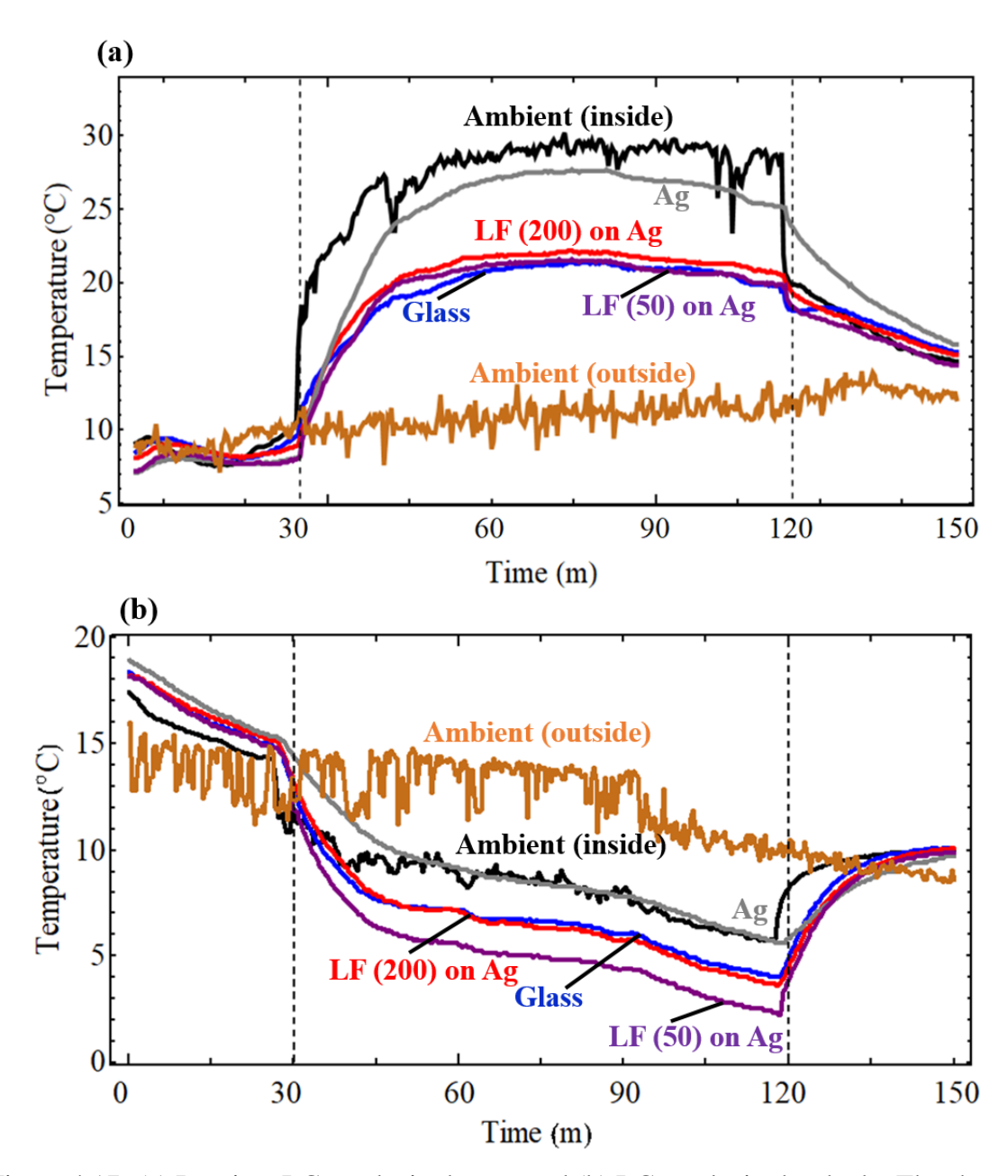


Figure 4.17: (a) Daytime RC results in the sun and (b) RC results in the shade. The shutter opened at 30 min and 120 min. Samples are the 100 nm-thick Ag film, the 1 mm-thick glass substrate, the 50  $\mu$ m-thick LF film on a Ag substrate and a 200  $\mu$ m-thick LF film on a Ag. Temperature of ambient both inside and outside the chamber was recorded. The number indicate the film thickness in  $\mu$ m.

Figure 4.17(a) presents the results of samples under the sunlight. The dropped temperature of the 50  $\mu$ m-thick LF film is 0.7 °C higher than that of 200  $\mu$ m-thick LF film. This relation is also observed in the shade, as presented in Figure 4.17(b). The temperature drop of 50  $\mu$ m-thick LF is 3.4 °C, while that of 200  $\mu$ m-thick LF is only 2.0 °C. This difference

Table 4.10: The temperature reduction  $\Delta T$  (°C), under the sunlight of the Ag film, the glass substrate, the LF film on the Ag substrate with thicknesses of 50 and 200  $\mu$ m. The calculated temperature drop is also listed.

Samples	Ag film	LF (50 $\mu$ m)	LF (200 $\mu$ m)	Glass
Measured	$1.9 \pm 0.7$	$7.9 \pm 0.8$	$7.2 \pm 0.7$	$8.0 \pm 0.7$
Calculated	0.0	6.9	7.2	7.8

Table 4.11: The temperature reduction  $\Delta T$  (°C), in the shade of the Ag film, the glass substrate, the LF film on the Ag substrate with thicknesses of 50 and 200  $\mu$ m. The calculated temperature drop is also listed.

Samples	Ag film	LF (50 $\mu$ m)	LF (200 $\mu$ m)	Glass
Measured	$-0.1 \pm 0.2$	$3.4 \pm 0.3$	$2.0 \pm 0.3$	$1.8 \pm 0.3$
Calculated	0.8	3.3	3.2	3.0

can be explained by the emission spectra. The thin LF film is less susceptible to the thermal radiation at the wavelength range of 5-7  $\mu$ m.

#### 4.5 CONCLUSION

In this chapter, two daytime RC candidates were reported: polyester and LF polymers. The investigated polyesters are PET and PEN films, which present high emissivity, about 90% in the ATW. By the in-house RC measurement, the temperature reduction of PEN and PET films are similar, at 9.3 °C, which is as high as that of the PDMS film and the glass plate. The RC efficiency of PEN film is good as that of the PET film, and even PEN was opaque due to light scattering. If transparent PEN is made available, it can be used as daytime RC material. In addition, PET has advantages over RC materials in terms of chemical stability, optical transparency, and mold-ability.

Another candidate for daytime RC materials is LF film. It has high transparency at solar wavelength while high emission at the ATW, even in the thin thickness. The RC performance of the LF was compared to that of PDMS, glass, PE, and SiO<sub>2</sub> particles/glass. Although, even the RC performance of LF is a little lower than particles/glass, the LF film has exciting features such as solvent-soluble, paintable, and weather-ability. As a result,

the LF film promises cooling solar cells and buildings with a low fabrication cost.

## **CHAPTER 5**

## TRANSPARENT NON-RADIATIVE COOLING MATERIALS

## 5.1 BACKGROUND

This chapter presents some transparent non-RC materials, which are transparent in the visible region while reflectance in the IR region to block unwilling thermal radiation. After evaluating the performance of transparent electrodes such as ITO and DMD structure, the conclusion is that they are good candidates for non-RC materials. At the same time, they still face some challenges, such as high fabrication costs [98, 99], and enlargement difficulties [100, 101]. Thus, the AgNWs mesh film was considered as another candidate for non-RC material. The fabrication techniques of the AgNWs mesh film are low [102, 103] and promise to coat windows or car windshields [104, 105]. The detail of the results will be explained below.

## 5.2 EXPERIMENT

# 5.2.1 Non-RC materials

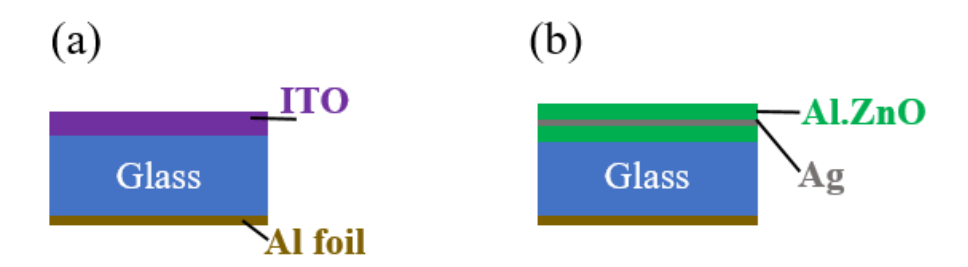


Figure 5.1: Schematic structure of (a) ITO, and (b) DMD films on the glass substrate.

Glass with high RC performance is used as the substrate in this experiment. The substrate size is fixed at 3.8 x 2.6 (cm<sup>2</sup>). The schematic structure of both DMD and ITO films

is presented in Figure 5.1. The ITO film with different thicknesses of 20 nm, 50 nm, 150 nm, and 300 nm was supported by Geomatec company. DMD structure consists of three layers of AZO, Ag, and AZO, with the thickness of 50, 10, and 50 nm, respectively. The Al foil is used to block the unwilling thermal radiation of the backside of the substrate.

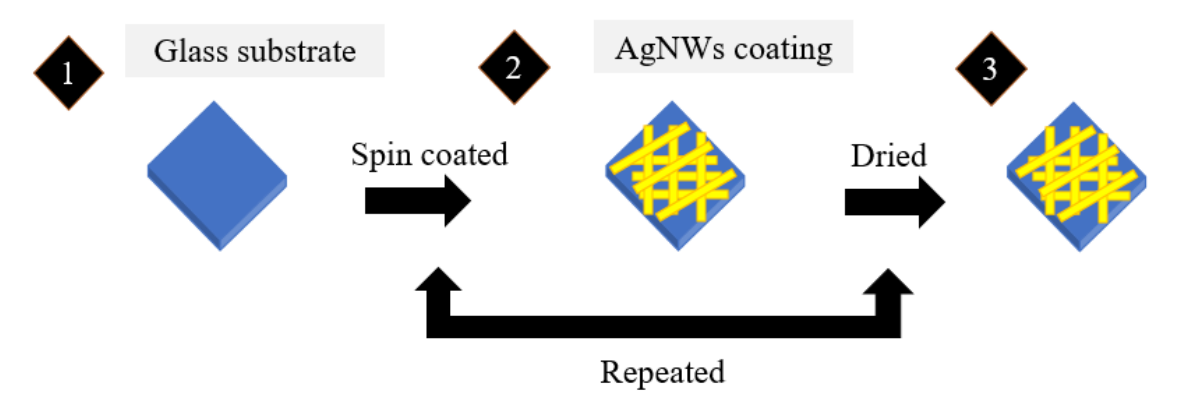


Figure 5.2: Fabrication process of the AgNWs film on the glass substrate.

Figure 5.2 presents the fabrication process of the AgNWs film on the glass substrate. AgNWs dispersed on ethylene glycol were obtained from Novarials company (product name: Nanowire-Ag-70). The length and diameter of AgNWs are 45  $\mu$ m and 70 nm, respectively. The AgNWs film was fabricated onto a cleaned glass substrate by the spin coating method. The treatment of glass substrates was described in the fabrication process of daytime-RC materials. First, the original AgNWs solution was diluted in ethanol with a volume ratio of 1:5. Then, the solution was stirred via sonication. Next, a 50  $\mu$ l AgNWs solution was dropped on a substrate and spin-coated at 500 rpm for 5 minutes. After that, the sample was dried on the hot plate at 60°C for 5 minutes. AgNW films with the various coverage were obtained by repeating the spin-coating process at 3, 7, 14, 21, and 28 times.

#### 5.2.2 Material characterization

The property of samples was investigated as the way of the daytime-RC materials.

# 5.2.3 In-house temperature measurement

The experiment process and used equipment are similar as the daytime-RC materials.

# 5.2.4 Field temperature measurement

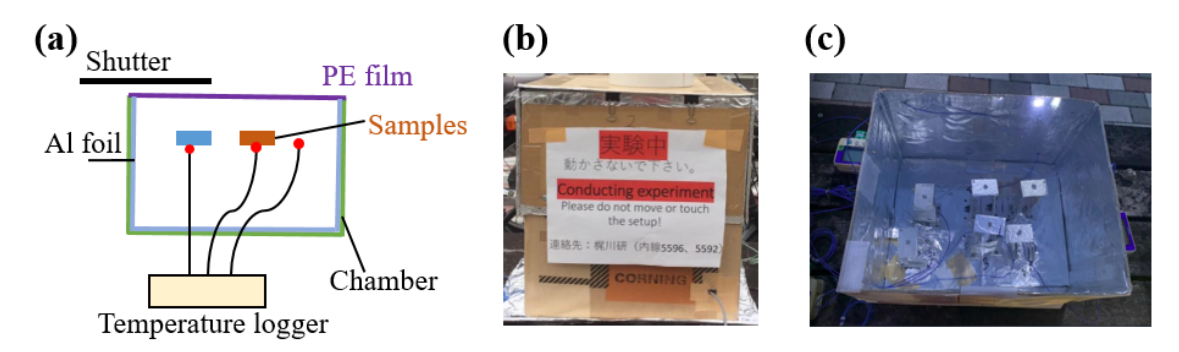


Figure 5.3: (a) Schematic of the field setup, images of (b) a chamber, and (c) samples inside a chamber.

Figure 5.3 presents a schematic of the field-experimental set up in the parking area of Suzukakedai campus, Tokyo Institute of Technology, Japan. The sample temperature was characterized in the evening on a clear day. Samples were placed in a chamber and exposed to the sky. The chamber was made of a packaging box of 30 cm x 25 cm x 18 cm. Similar to the in-house setup, the inner of the chamber was covered with an Al foil. The top surface of the chamber was coated with the PE film to transmit the thermal radiation and minimize the convection heat transfer by the wind. Thermal couples were placed on the backside, near the samples, and outside the chamber to measure the temperature of samples, the ambient inside, and the ambient outside.

The experiments were conducted in four steps:

- 1. Step 1: Cover the top chamber with the shutter for 20 minutes.
- 2. Step 2: Remove the shutter, and samples expose to the sky for 40 minutes.
- 3. Step 3: Repeat the first and second steps one more time.
- 4. Step 4: Use the shutter and finish the experiment.

The dropped temperature is evaluated by the different temperatures of samples and ambient air inside the chamber.

#### 5.3 RESULTS AND DISCUSSION

## 5.3.1 Results of ITO and DMD films

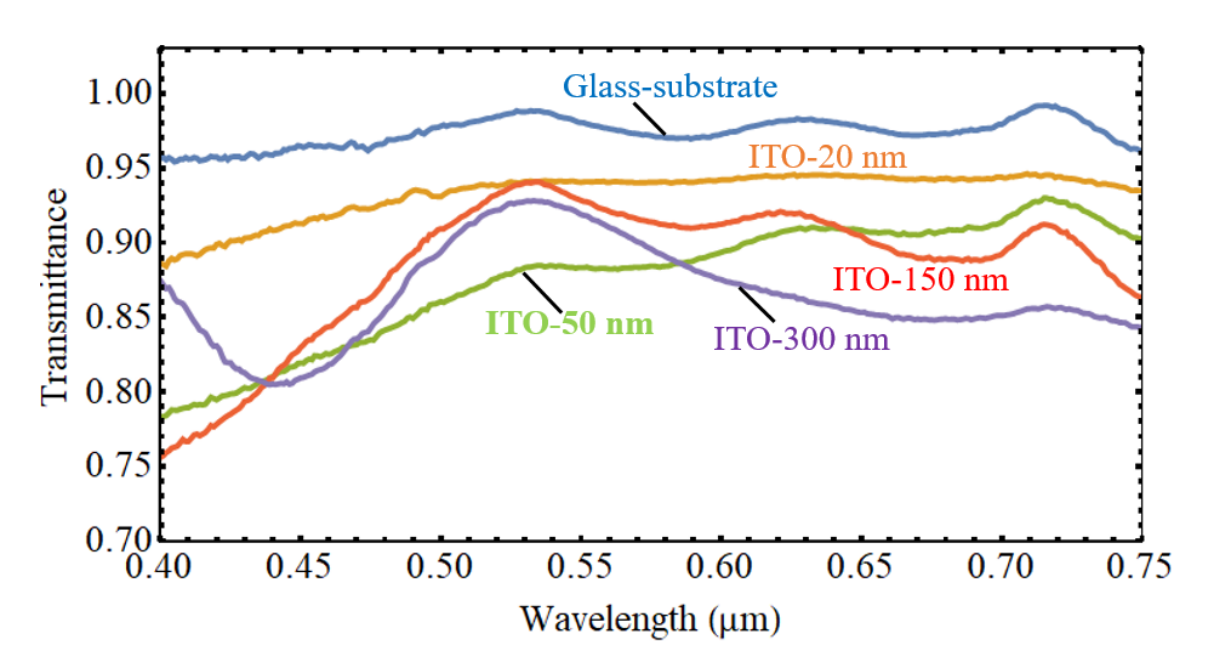


Figure 5.4: Transmittance of ITO films with thicknesses of 20, 50, 150 and 300 nm in the visible wavelength range ( $\lambda = 0.4\text{-}0.75~\mu\text{m}$ ). Numbers in parentheses indicate film thickness.

Figure 5.4 presents visible transmittance spectra of ITO films on the glass substrate. The transmittance of the 1 mm-thick glass is shown as a reference. The ITO film is the mixture of indium oxide ( $In_2O_3$ ) and tin oxide ( $SnO_2$ ), where the Sn substitutes the In. The deficiency of oxygen gives a film that has a high optical transmission, and electrical conductivity [106, 107]. In the 450-750 nm wavelength range, the average transmittance of 20, 50, 150, and 300 nm-thick ITO is 93, 88, 89, 87 %, respectively. However, with increasing the thickness from 20 to 300 nm, the average transmittance in this region decreases slowly. This decrease in transmittance is due to absorption of free carriers that increases the carrier density in the thick films [108].

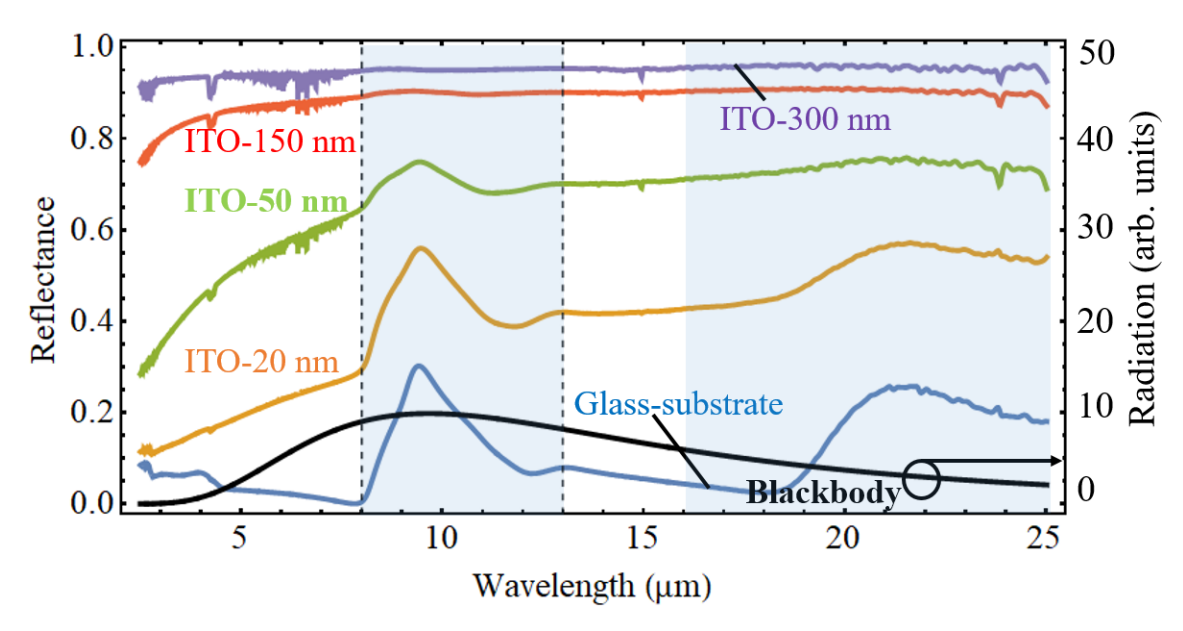


Figure 5.5: Reflectance of ITO films with thicknesses of 20, 50, 150 and 300 nm in the IR wavelength range (2.5-25  $\mu$ m). Numbers in parentheses indicate film thickness.

Figure 5.5 presents the reflectance of the ITO films with different thicknesses. The thermal radiation spectrum of a blackbody at 300 K is shown in the black line as the reference. In the IR region, the reflectance of the ITO film increases with increasing the film thickness which corresponds to the decrease of the transmittance. This phenomenon is caused by the interaction of the incident long-wavelength radiation with the free electrons in the films. In the thicker film, the free carrier increase; as a result, the transmittance decreases.

Figure 5.4, the 300 nm-thick ITO film displays a transmittance higher than 80% in all the visible ranges from 400 to 750 nm. Furthermore, the transmittance of the ITO film is as high as 92% at the wavelength of 550 nm, which is a desirable feature in the window coating since it can help to prevent unwanted heating. In addition, the reflectance of a 300 nm-thick ITO is as high as 95%, especially in the ATW, which allows blocking the losses of heat. Thus, a 300 nm-thick ITO film was chosen to compare with the DMD films.

Figure 5.6 presents the transmittance of 300 nm-thick ITO and DMD films on the glass substrate. The average transmittance of ITO and DMD films is 87 and 94%, respectively, which is high to avoid heating under the sunlight. A 10 nm-thick metal is sand-witched by the 50 nm-thick AZO films in the DMD structure. At 550 nm, the real (n) and imaginary

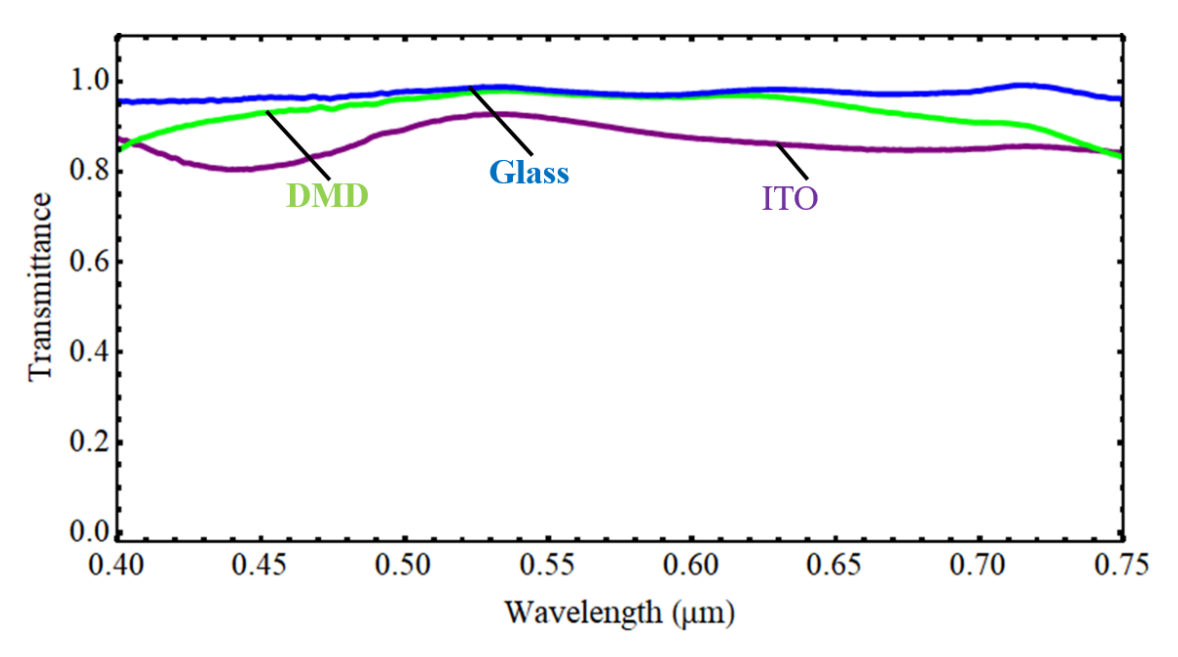


Figure 5.6: Transmittance of different samples in the visible region: a 300 nm-thick ITO, DMD films, and a 1 mm-thick glass.

(k) part of refractive index of Ag are 0.13 and 3.17 [109]. Because nk is small, thus, the Ag has low absorption and high transmittance. Moreover, the AZO film has a high refractive index, n = 1.9; thus, DMD film has a high broadband transmittance while conductivity [110].

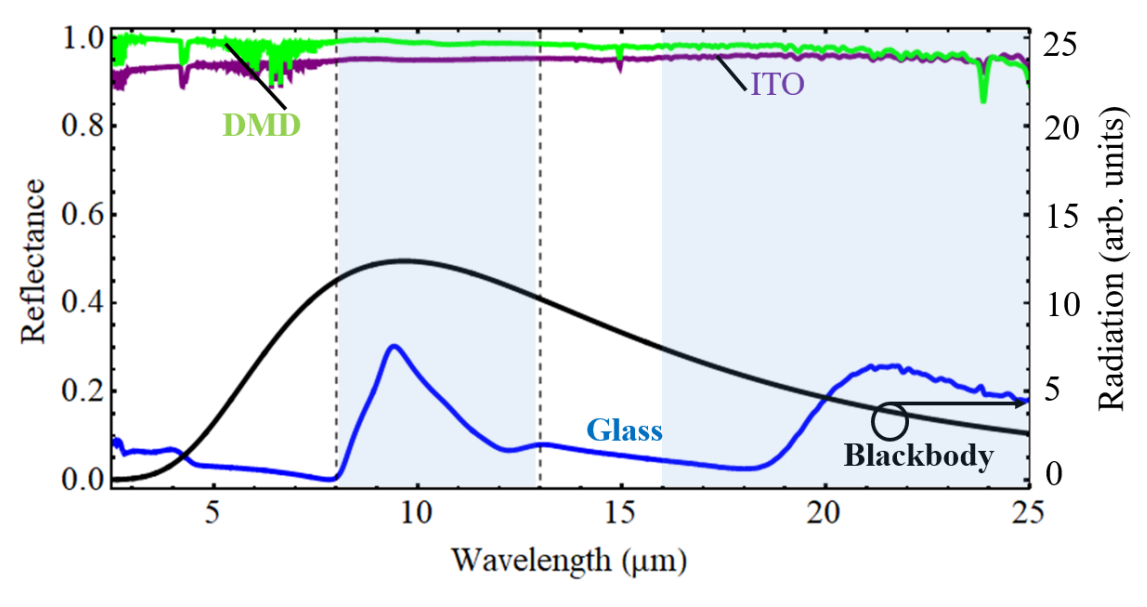


Figure 5.7: Reflectance of different samples in the IR region: a 300 nm-thick ITO, DMD films, and a 1 mm-thick glass.

Figure 5.7 presents the reflectance of 300 nm-thick ITO and DMD films in the IR range. Both ITO and DMD films have higher reflectance than the glass substrate, especially in the ATW. In the wavelength range of 2.5 to 25  $\mu$ m, the 10 nm-thick Ag film acts as the mirror; thus, the DMD has approximately 100% in reflectance. This section realized that both ITO and DMDs films have the high transmittance in the visible region and the high reflectance in the IR region. Thus, they satisfy all required conditions of non-RC materials. The following section will explain the non-RC efficiency of samples.

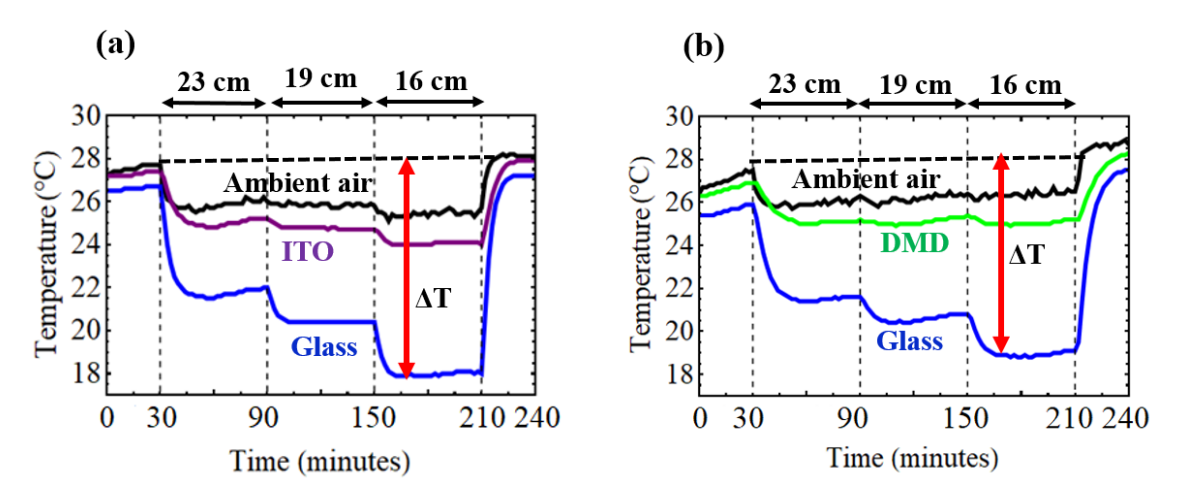


Figure 5.8: Measured temperature between ambient air, glass and (a) a 300 nm-thick ITO, (b) DMD films.

The temperature of the ITO and DMD films was measured using the in-house experiment setup (Figure 4.6). Figure 5.8(a) presents the recorded temperature of a 300 nm-thick ITO, glass, and ambient air. In the initial step, at a time of 0-30 minutes, the temperature of the glass is approximately 2°C lower than the ambient temperature. This is caused by the high emission of the glass to the cooled lid placed above the LN, as explained before. Nevertheless, the temperature of the ITO film with a low emission does not cool down and is approximate to the ambient temperature. After removing the shutter at 30 minutes, the temperature of the glass is dramatically dropped. However, the temperature drop of the ITO film is smaller and slower. This result contributed to the thermal radiation of the glass substrate being blocked by the ITO film. The temperature of the DMD film, as displayed in Figure 5.8(b), was similar to the ITO film.

Table 5.1: Temperature reduction of a 300 nm thick-ITO film at different distance between samples and the LN, d, measured and calculated, in the in-house measurement.

Distance d (cm)	23	19	16
Measured (°C)	$1.5\pm0$	$1.8 \pm 0.1$	$2.7\pm0.4$
Calculated (°C)	0.3	0.4	0.5

Table 5.2: Temperature reduction of a DMD film at different distance between samples and the LN, d, measured and calculated, in the in-house measurement.

Distance d (cm)	23	19	16
Measured (°C)	$2.55\pm0.2$	$2.6 \pm 0.3$	$2.8 \pm 0.4$
Calculated (°C)	0.1	0.15	0.2

Table 5.1 and Table 5.2 present the temperature reduction of ITO and DMD films at different distances, d. The temperature reduction increases as d decreases because the solid angle to the refrigerant from the sample becomes smaller, as described in daytime-RC materials. The calculated temperature drop is also listed. Because of an oxide layer, calculated and measured results of non-RC materials are disagree well while their trend is consistent. For example, at a distance of 16 cm, the measured temperature reduction of ITO, DMD films, and the glass plate are  $2.7 \pm 0.4$ ,  $2.8 \pm 0.4$ , and  $8.9 \pm 0.4$  (°C), respectively. In the calculated result, the dropped temperature of ITO, DMD, and glass are 0.5, 0.2, and 8.5 (°C). The temperature reduction result contributed that the thermal radiation of the glass was blocked by non-RC materials such as ITO and DMD films.

Table 5.3: Temperature reduction of the ITO film with different thicknesses, at d = 16 cm, measured and calculated, in the in-house measurement.

Thickness (nm)	20	50	150	300
Measured (°C)	$6.6 \pm 0.8$	$5.6 \pm 0.0$	$4.7 \pm 0.6$	$2.7 \pm 0.4$
Calculated (°C)	5.7	3.1	1.1	0.5

Table 5.3 presents the measured temperature drop of the ITO film. The thickness of the ITO film is 20, 50, 150, and 300 nm. The temperature drop decreases with increasing thicknesses and is the lowest at 300 nm. As the measured results, the the 300 nm-thick ITO

film's temperature reduction approximates to that of the 100 nm-thick gold film,  $\Delta T = 3.0$  °C. This means that a 300 nm-thick ITO is sufficient for the high non-RC efficiency.

This section concludes that the ITO and DMD films are good candidates for blocking thermal radiation. They satisfy all required conditions of non-RC materials, such as high transmittance in the visible region and high reflectance in the IR region, especially at the ATW. Nevertheless, they still face challenges, such as high fabrication costs and difficulty applying in a large area. Therefore, the following section considered the AgNWs mesh film as another candidate for non-RC materials. Because it has low fabrication cost and paint-ability, thus promises real large-area applications.

# 5.3.2 Results of the AgNWs mesh film

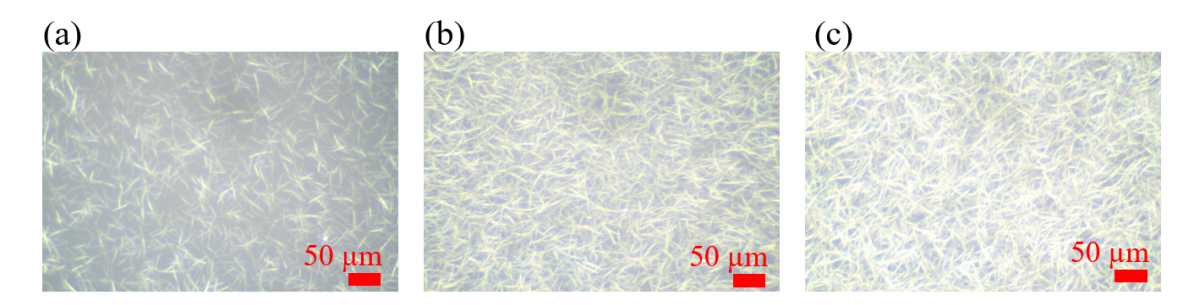


Figure 5.9: Optical microscope images with the magnification of 60 times of the AgNWs mesh film on a glass, (a) 3 times, (b) 14 times and (c) 28 times of spin-coating process repetitions.

Diluted AgNWs dispersion was coated onto the glass substrate, and results are shown in the optical microscopy images in Figure 5.9. At 3 times of repetition, the network of the AgNWs is non-uniform with some holes where the substrate is visible. It is clear from these images that the network becomes less space with increasing the number of repetition. At 28 times of repetition, the substrate cannot be seen, and the network appears spatially homogeneous. An attention is that when increasing the number of repetitions, the hole space decreases, as a result, the coverage of AgNWs increases, too.

Figure 5.10 presents the transmittance spectra of AgNWs films in the visible region. The average transmittance in this range is 93, 88, 84, 79, and 73% at the spin-coating

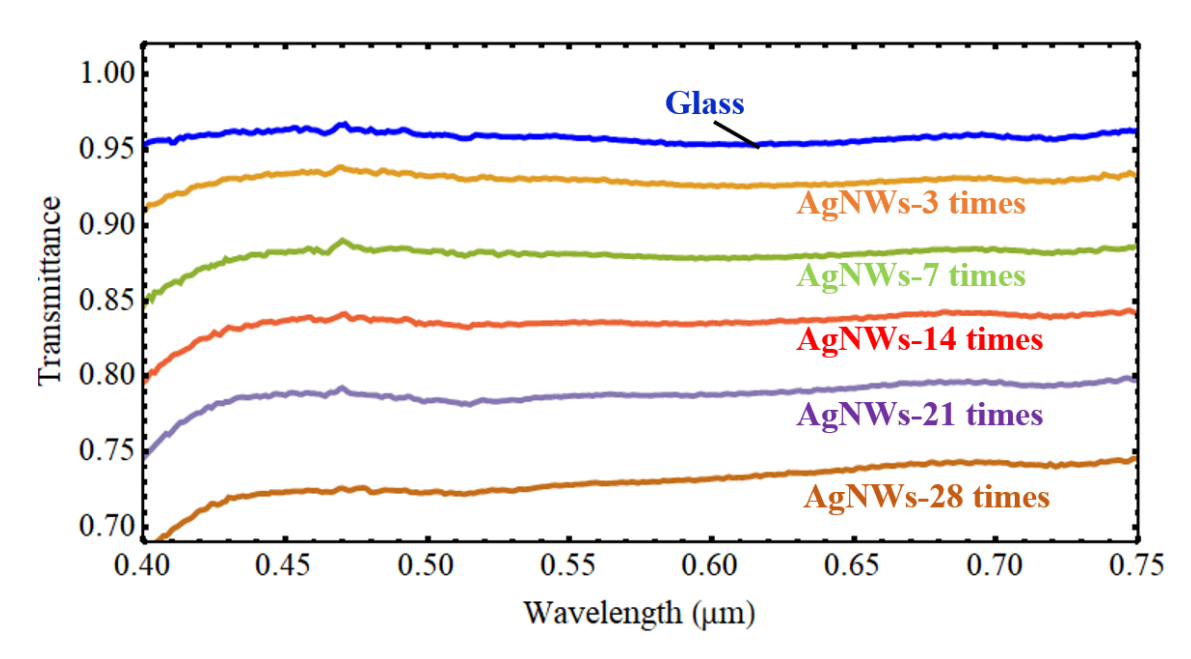


Figure 5.10: Transmittance of AgNWs films on the glass substrate. The result of the glass presents as the reference. The numbers in the parenthesis indicate the number of spin coating repetition.

repetition of 3, 7, 14, 21, and 28 times, respectively. The transmittance of all films is higher than 70%; light passes through the random holes of the AgNWs network. The fraction of holes decreases with increasing the number of repetitions of the spin-coating process; thus, the transmittance also slowly decreases. As the National Transportation Library of the United States, cars are allowed to have window coating treatments that do not reduce the transmittance of light below 70% for the windshield and 35% for other [111]. Thus, the transmittance of the AgNWs film is high enough for coating in car windows.

Figure 5.11 presents the reflectance spectra of the AgNWs film on the glass substrate. The reflectance of the glass is presented as the reference. In the main ATW ( $\lambda$ = 8-13  $\mu$ m), the average reflectance of the AgNWs film at 3, 7, 14, 21, and 28 times of spin-coating repetitions is 24, 35, 48, 59, and 74%, respectively. Increasing the spin-coating time significantly increases the reflectance because of decreasing transmittance. In the long-wavelength range, the incident light can not pass through the holes of the AgNWs network. In addition, the fraction of holes decreases with the increase of the spin-coating time. Thus, the transmittance of the AgNWs films is high in the visible region while is low

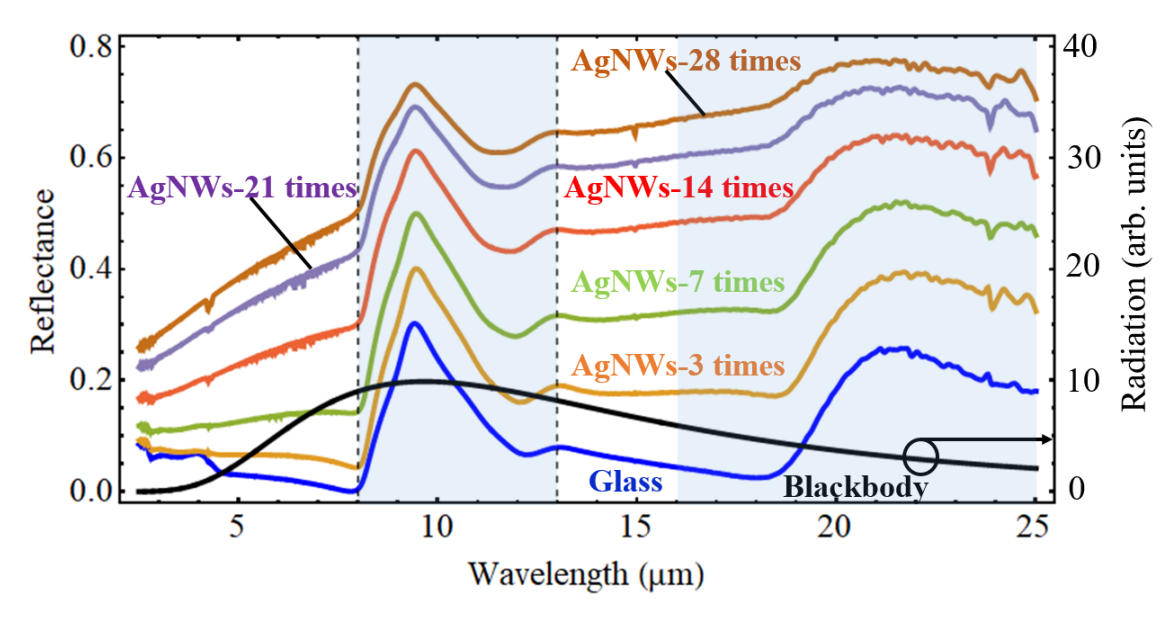


Figure 5.11: Reflectance of AgNWs films on the glass substrate. The result of the glass presents as the reference. The numbers in the parenthesis indicate the number of spin coating repetitions. The black line indicates the blackbody radiation at 300 K. The hatched areas indicate the ATW.

in the IR region and strongly depends on the number of spin-coating times. At the 9.5  $\mu$ m in wavelength, the absorption peak occurs in all spectra because of the SPhP resonance of the glass. In addition, the network of AgNWs films seems to be not dense enough to block all the thermal radiation of the substrate. The solution is to reduce the hole of the AgNWs network while still maintaining the high transmittance in the visible region.

The ambient air and sample temperature were measured by the in-house experiment setup. Samples are the bare glass and the glass coated by the AgNWs film. The spin-coating repetition of the AgNWs film is 28 times. Similar to ITO and DMD films, after removing the shutter, the temperature reduction of the AgNWs film is lower than the glass substrate. For example, at a distance, d, of 16 cm, the temperature drop of the bare glass substrate is nearly 9°C while that of the AgNWs film is only 5.3°C. The result contributed to the thermal radiation of the glass substrate being blocked by the AgNWs film. The measured and calculated temperature reduction of the AgNWs film is presented in Table 5.4. Again, their result does not agree well while their trend is consistent.

Table 5.4: Measured and calculated results,  $\Delta T$ , of AgNWs-28 times at different distances between the sample and LN, d, in the in-house measurement.

Distance d (cm)	23	19	16
Measured (°C)	$3.9 \pm 0.1$	$4.3 \pm 0.1$	$5.3 \pm 0.1$
Calculated (°C)	1.9	2.7	3.7

# 5.3.3 Comparison of various samples

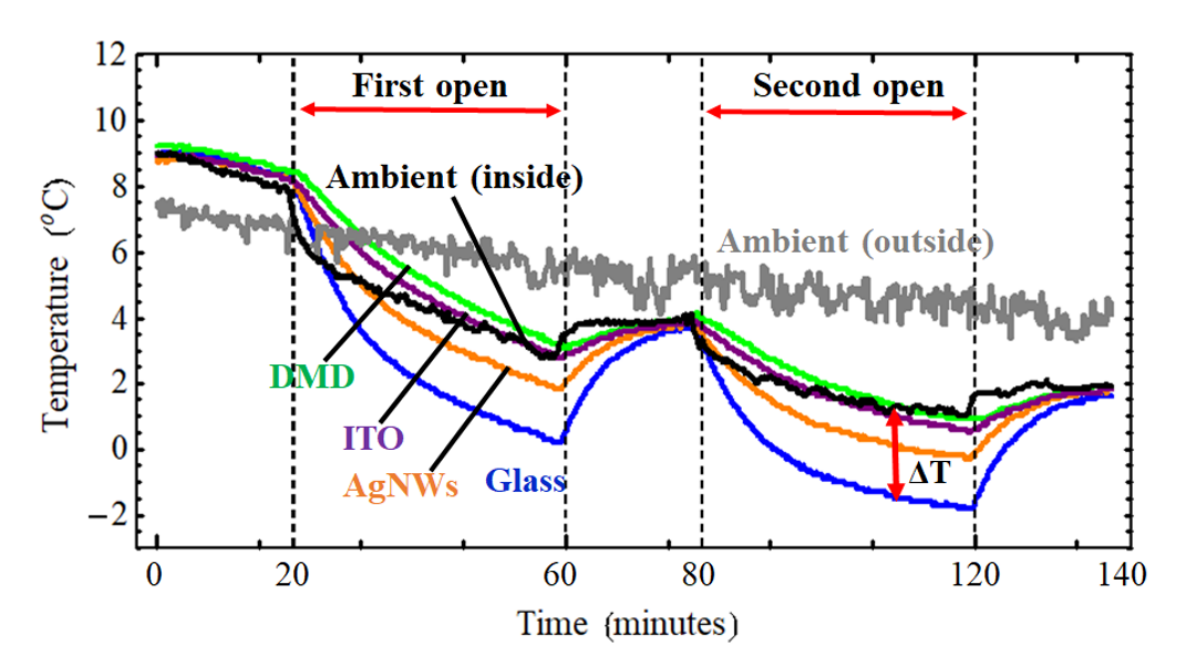


Figure 5.12: Measured field temperature of samples: a 300 nm-thick ITO, DMD, and AgNWs with the spin coating repetition of 28 times and glass substrate. The ambient air both inside and outside the chamber was also measured.

In this section, the temperature of all samples was measured by the field experiment setup as depicted in Figure 5.3. The 1 mm-thick glass, 300 nm-thick ITO, DMD, and AgNWs films are samples. Because the radiated thermal efficiency strongly depends on the weather condition such as humidity, wind speed, and cloud coverage. Thus, samples are set up in the same chamber and simultaneously exposed to the clear sky. The results were recorded on 2022 January, 21st. The experimental produce was as follows: the shutter was used at 0-20, 60-80, 120-140 (min); and the shutter was removed, samples were exposed to the sky at 20-60, 80-120 (min). Temperature decreases were observed when the shutter was removed at 20 min and 80 min. The dropped temperature of the ambient inside the chamber is due to the RC of the chamber. Even the inner chamber is coated with the Al foil, it still has an emission of 0.02.

The dropped temperature of samples equals the ambient inside temperature minus the temperature of the samples,  $\Delta T = T_{\rm amb}$  -  $T_{\rm s}$ . Table 5.5 presents the measured temperature reduction of samples. The dropped temperature of non-RC materials such as AgNWs, ITO, and DMDs films is much lower than that of the glass substrate. For example, in the second measurement, the temperature drop of the bare glass is 2.7 °C while that of AgNWs, ITO, and DMD films is 1.2, 0.3, and 0 °C. This result contributed that the investigated non-RC materials can block the thermal radiation of samples not only in-house but also in the field measurement.

In the first measurement, the sample's temperature was recorded before sunset while samples were in shadow. Therefore, the temperature drop of ITO and DMD films is negative because samples absorbed the scattering of sunlight. However, in the second measurement, the temperature reduction of ITO and DMD films is approximately the ambient air temperature.

Table 5.5 shows that the non-RC performance of ITO and DMD films is better than AgNWs films. Therefore, we come up with an idea to improve AgNWs' performance by increasing the transmittance in the visible region and the reflectance in the IR region. For this purpose, the tiny diameter and the high network density of AgNWs would be necessary. Although the nanowire diameter of 70 nm was recently used, a smaller diameter such as 40 nm is also available. The decrease in a diameter promises to increase the transmittance in the visible region. Moreover, the higher density of the network is expected to improve the reflectance in the IR region.

Table 5.5: Summary of difference temperature of samples and the ambient air inside the chamber,  $\Delta T$  (°C), measured by the field experiments. The average temperature was estimated by using the last 20 min of the first and second measurement of opening the shutter.

Samples	Measured (1st)	Measured (2 <sup>nd</sup> )
Glass	$2.6 \pm 0.2$	$2.7\pm0.2$
AgNWs	$1.0 \pm 0.2$	$1.2 \pm 0.2$
ITO	$-0.1 \pm 0.2$	$0.3 \pm 0.2$
DMD	$-0.5 \pm 0.2$	$0 \pm 0.2$

#### 5.4 CONCLUSION

In this chapter, three candidates of non-RC materials were investigated: ITO, DMD, and AgNWs films. ITO and DMD films are well known as transparent electrodes, above 87% of light transmittance in the visible region and above 95% of light reflected in the IR region. Therefore, they are good candidates for non-RC materials. However, at the same time, their fabrication cost is high and challenging to apply in larger areas. In contrast, the AgNWs film with 73% of light transmittance in the visible range and 74% of light reflectance in the IR region promises significant application at a low cost because of its paint-able properties.

Both in-house and field experiment setups were used to confirm the efficiency of non-RC materials. In the in-house measurement, the temperature reduction of AgNWs, ITO, and DMD films is 5.3, 2,7, and 2.8 °C, respectively. Under the same conditions, the temperature reduction of the glass substrate is 8.9 °C. In the field temperature measurement, the dropped temperature of AgNWs, ITO, and DMD films is 1.2, 0.3, and 0 °C, respectively. In contrast, the dropped temperature of the glass is 2.7 °C. The temperature reduction,  $\Delta T$ , of ITO, DMD, and AgNWs films are lower than the glass plate. It contributed to the fact that ITO, DMD, and AgNWs films can block the unwilling thermal radiation.

## **CHAPTER 6**

#### **CONCLUSION**

This study investigated the optical and thermal radiation properties of polymers and  $SiO_2$  particles in the IR region.

The optical properties in the IR region were investigated through the SPhP resonance and unusual transmittance of the gold-capped microsphere. SPhP resonances of SiO<sub>2</sub> bead are observed at 9 and 21  $\mu$ m. When increasing the size of beads the resonance peaks are wider and cover all range of the ATW. Thus, the SiO<sub>2</sub> beads promise for high RC performance.

The observation of EOT phenomenon can be summarized as follow:

- The EOT phenomenon of gold-capped microspheres was observed in the IR region, which has not been reported before.
- The characteristic of the EOT phenomenon was evident in the size, the coverage, and materials of microspheres.
- The FDTD simulation indicates that light pass through the openings between the gold film on the substrate surface and the gold cap. This type of EOT did not occur in the visible and near-IR regions.

The thermal radiation properties in the IR region were explored through RC technology. Both daytime-RC and non-RC materials were investigated. The results of daytime-RC materials can be listed below.

• Polyester and LF films have high transmittance in the visible region while high emission in the ATW. They satisfy all requirements of daytime-RC materials.

- The method and analysis for evaluating the RC performance of materials in in-house measurements were carried out. LN was used as the refrigerant.
- The field measurements and analysis methods were presented. It is found that the separate treatment of the ambient temperature in the chamber and the atmospheric temperature is essential to explain the result.
- The investigated daytime RC materials present a good performance as the reported RC materials such as glass, PDMS, and SiO<sub>2</sub> spheres on glass. As predicted, SiO<sub>2</sub> particles on the glass sample presents the high RC performance because of SPhP resonance of SiO<sub>2</sub> beads.

After investigating the daytime-RC materials, I realized that the non-RC is also important. The results of non-RC materials can be listed below:

- ITO, DMD, and AgNWs films are transparent in the visible region while reflectance in the IR region. They are satisfied with the condition of non-RC materials.
- Similar to the daytime RC materials, the non-RC performance was confirmed by inhouse and field setup. The results contributed that the reported non-RC materials can block unwilling thermal radiation.

I expected that the EOT phenomenon observed in this study would be helpful to understand the mechanism of extraordinary transmission and apply it in sensing applications. In addition, the daytime-RC materials can improve the performance and lifetime of solar cells, cool the buildings, and generate power. Moreover, the non-RC materials can be relevant to block the unwilling thermal radiation.

# APPENDIX A VIEW FACTOR

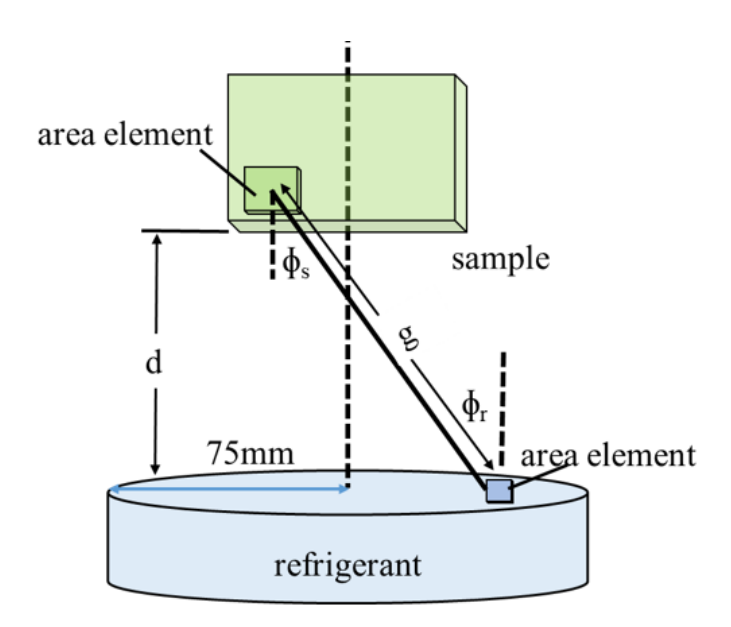


Figure A.1: Geometry for the calculation of the view factors.

Table A.1: View factors  $F_{s \to LN}$  calculated for the present geometry at various distance, d.

d (cm)	16	19	23
$F_{\mathrm{s} \to \mathrm{LN}}$	0.178	0.134	0.0956

To evaluate the view factor, consider the geometry illustrated in Figure A.1, where the rectangular sample with area  $A_{\rm s}$  is placed above the refrigerant with diameter R and area  $A_{\rm r}$ .  $\phi_{\rm s}$  is the angle between the line connecting the area element on the substrate and the area element on the refrigerant surface and the surface normal of the substrate. Similarly,  $\phi_{\rm r}$  is the angle between that line and the surface normal of the refrigerant. The view factor from the sample to the refrigerant is:

$$F_{s\to LN} = \frac{1}{A_s} \int_{A_r} \int_{A_s} dA_s dA_r \frac{\cos\phi_s \cos\phi_r}{\pi g^2},$$
 (A.1)

where the distance between the elements is g. In this study, the sample area is  $38 \times 26$  mm<sup>2</sup>, and the diameter of the refrigerant is 150 (mm). The sample is placed at position d above the refrigerant. The view factors for this geometries are presented in Table A.1

# APPENDIX B

# HEAT CONDUCTION IN THE SAMPLE

Consider a sample as shown in Figure 4.6, in which the temperature  $T_1$  and  $T_2$  are at the rear surface and front surface, respectively. The thickness of the sample, L, and thermal conductivity, k, are considered. The heat flow, Q in the air at the rear surface is described as,

$$Q = h(T_{\text{amb}} - T_1) \tag{B.1}$$

$$Q = \frac{k}{L}(T_1 - T_2) \tag{B.2}$$

then,

$$T_2 = T_1 + \frac{Lh}{k}(T_1 - T_{\rm amb})$$
 (B.3)

In the present case, L=1 x  $10^{-3}$  m, k=1 W m $^{-1}$  K $^{-1}$ , and h=3 W m $^{-2}$  K $^{-1}$ . Since  $\frac{Lh}{k}$   $\approx 3$  x  $10^{-3}$ , and  $T_{\rm amb}$  -  $T_1 \le 10$  K,  $T_1$  and  $T_2$  can be approximated to be equal. Then, the factor of 2 used in Equation (2.6)

# **APPENDIX C**

# ESTIMATE THE THICKNESSES OF LF FILMS

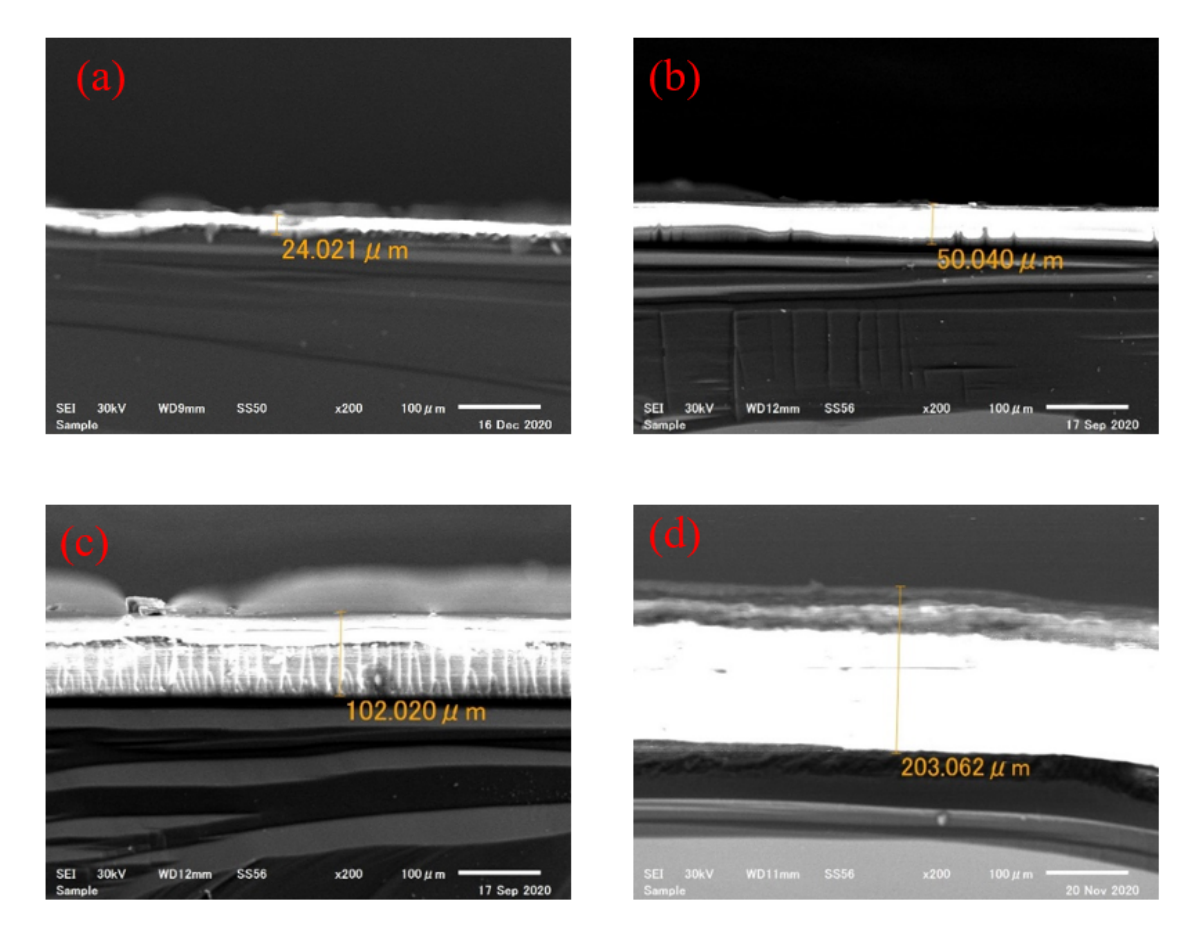


Figure C.1: The cross-sectional SEM images of LF films with different thicknesses (t:  $\mu$ m), (a) t = 25, (b) t = 50, (c) t = 100, (d) t = 200.

Figure C.1 presents the cross-sectional SEM images of LF films with thickness thicker than 25  $\mu$ m.

The thickness of the thin LF films was estimated by the interference of the reflectance spectrum in the visible region. Figure C.2 presents the reflectance spectrum of LF films on the Au thickness. As the ellipsometry results, the refractive index of LF at 1.5 was used.

The thickness of LF films was estimated by using the equation:

$$t = \frac{1}{2n} \frac{\lambda_1 \lambda_2}{\lambda_2 - \lambda_1},\tag{C.1}$$

where, n is the refractive index of LF,  $\lambda_1$  and  $\lambda_2$  are the peak positions of two oscillations next together.

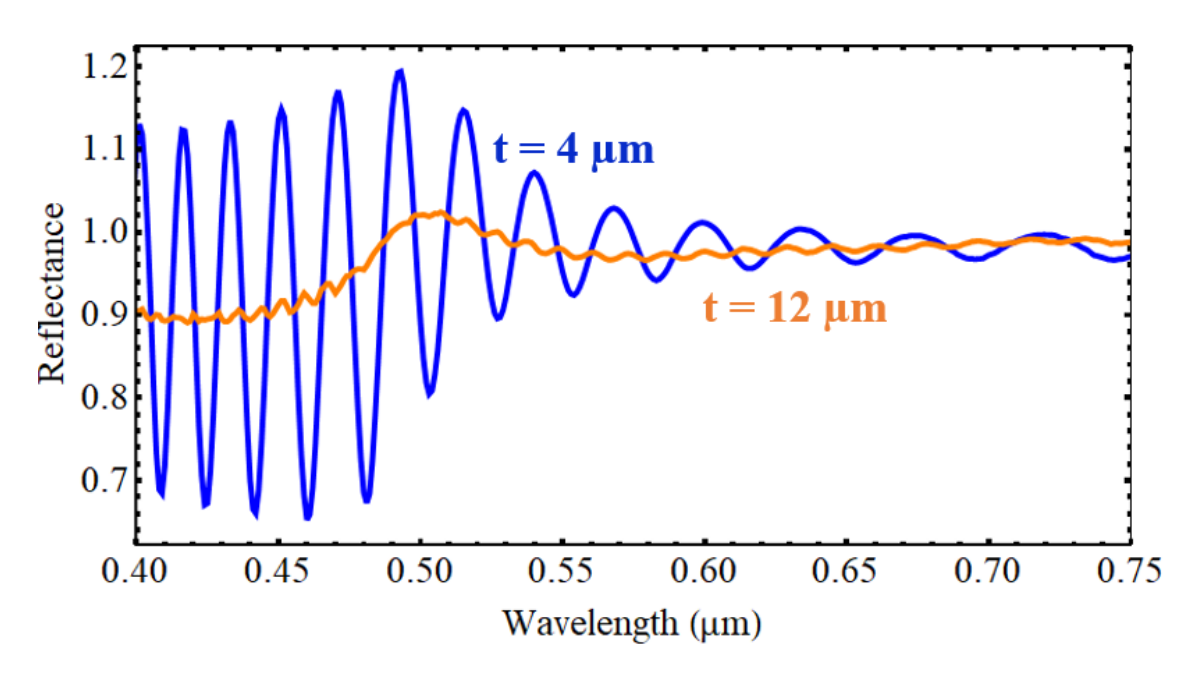


Figure C.2: The reflectance spectrum of LF on the Au substrate in the visible region. The number indicated the estimated thickness.

# APPENDIX D OPTICAL PROPERTIES OF PE FILMS

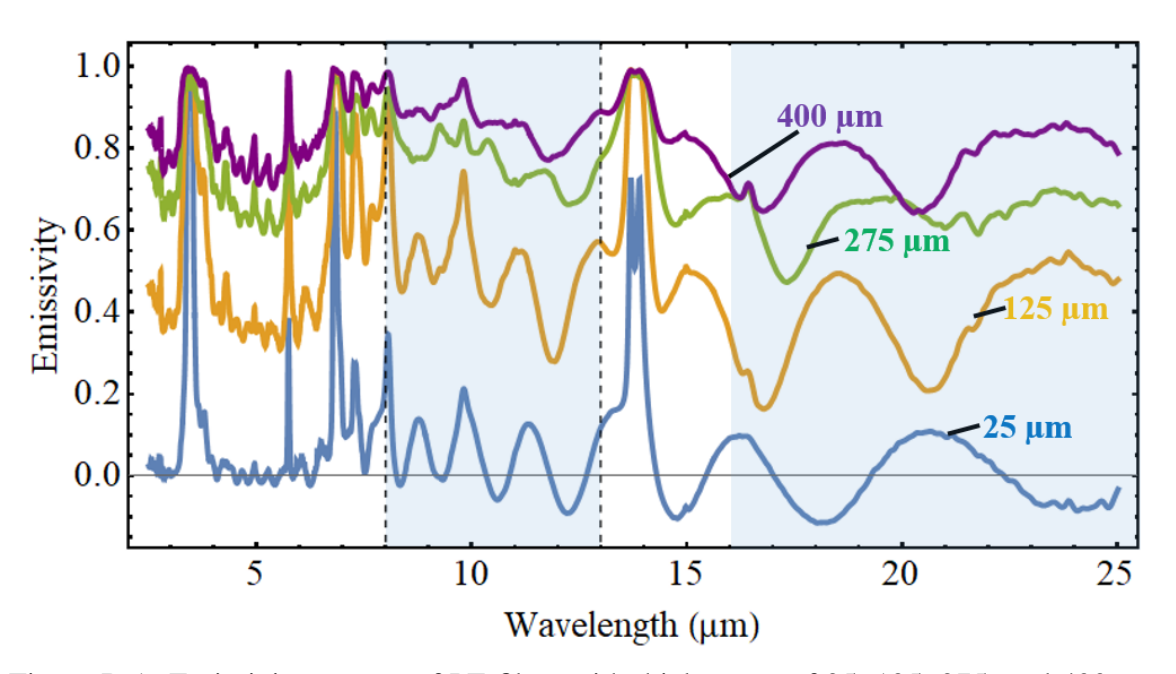


Figure D.1: Emissivity spectra of PE films with thicknesses of 25, 125, 275, and 400  $\mu$ m in the IR wavelength range (2.5 - 25  $\mu$ m). Numbers in parentheses indicate film thickness. The hatched area indicates the ATW.

In the 25  $\mu$ m-thick PE film, the oscillation observed in the spectrum was due to interference in the PE film. The interference profile allows us to evaluate the thickness of the film as 25  $\mu$ m, using the refractive index of PE as 1.52 [112]. Unfortunately, thick PE films are unavailable; thus, 5, 11, and 16 layers were stacked to get thick PE samples. The thicknesses of PE film are 25, 125, 275, and 400  $\mu$ m. Figure D.1 presents the emissivity of PE films in the IR region.

## APPENDIX E

#### RESEARCH ACHIEVEMENTS

# **E.1** Publication list

- Hoang Thi Thanh Tam & Kotaro Kajikawa, "Extraordinary transmission of goldcapped sphere arrays in mid-infrared range", Optics Express, 29 (22) pp 35191-35205 (2021)
- 2. Hoang Thi Thanh Tam, Mana Toma & Kotaro Kajikawa, "Investigation of polyesters as daytime radiative cooling materials", Molecular Crystals and Liquid Crystals, (2022) https://doi.org/10.1080/15421406.2022.2038458
- 3. Hoang Thi Thanh Tam, Mana Toma, Takayuki Okamoto, Miho Hidaka, Kensuke Fuji, Yasuhiro Kuwana & Kotaro Kajikawa, "Weatherable, Solvent-solvle, Paintable, and Transparent Fluoropolymers for Daytime Radiative Cooling", Solar Energy Materials and Solar Cells, (Reviewing)
- 4. Hoang Thi Thanh Tam, Mana Toma & Kotaro Kajikawa, "Transparent non radiative cooling materials" (In preparation)

# E.2 Conferences attended

- 1. Hoang Thi Thanh Tam, Mana Toma & Kotaro Kajikawa "Transparent non-radiative cooling materials", The 69th JSAP Spring Meeting 2022, 24p-E303-10 (2022). (Oral)
- Hoang Thi Thanh Tam & Kotaro Kajikawa, "Mid-infrared extraordinary transmission through gold-covered dielectric microsphere monolayer", The 82nd JSAP Autumn Meeting, 10p – N404 - 6 (2021). (Oral)

- 3. Hoang Thi Thanh Tam, Mana Toma & Kotaro Kajikawa "Polyethylene Teraphplate (PET) film for daytime radiative wavelength", 2021 KJF International Conference on Organic Materials for Electronics and Photonics, PC2-16, (2021). (Poster)
- 4. Hoang Thi Thanh Tam, Mana Toma, Takayuki Okamoto, Mio Hidaka, Kensuke Fujii, Yasuhiro Kuwana & Kotaro Kajikawa, "A transparent fluoropolymer for daytime radiative cooling", META 2021, the 11th International Conference on Metamaterials, Photonic Crystals and Plasmonics, 3P1 (2021). (Poster)
- 5. Hoang Thi Thanh Tam, Mana Toma, Takayuki Okamoto, Mio Hidaka, Kensuke Fujii, Yasuhiro Kuwana & Kotaro Kajikawa, "Transparent fluoropolymer for daytime radiative cooling", The 68th JSAP Spring Meeting 2021, 17a-Z05-8 (2021). (Oral)
- Hoang Thi Thanh Tam & Kotaro Kajikawa, "Extraordinary transmission of gold-capped SiO<sub>2</sub>-sphere array", The 80th JSAP Autumn Meeting, 18p E208 4 (2019).
   (Oral)
- L. T. Nguyen, Hoang T. T. Tam, Junichi Takahara, Takayuki Okamoto & Kotaro Kajikawa "Radiative cooling of SiO<sub>2</sub> glass in the room" The 65th JSAP Spring Meeting, 19p-B203-13 (2018) (Oral)

# REFERENCES

- [1] F. Vatansever and M. R. Hamblin, "Far infrared radiation (FIR): Its biological effects and medical applications," *Photonics Lasers in Medicine*, vol. 4, pp. 255–266, 2012.
- [2] G. Fox, "The brewing industry and the opportunities for real-time quality analysis using infrared spectroscopy," *Applied Science*, vol. 10, pp. 1–12, 2020.
- [3] R. Stanley, "Plasmonics in the mid-infrared," *Nature Photonics*, vol. 6, pp. 409–411, 2012.
- [4] F. K. Tittel and D. Richter and A. Fried, *Mid-Infrared Laser Applications in Spectroscopy: Solid-State Mid-Infrared Laser Sources*. Berlin: Springer, 2003.
- [5] P. Werle, F. Slemr, K. Maurer, R. Kormann, R. Mücke, and B. Jänker, "Near- and mid-infrared laser-optical sensors for gas analysis," *Optics and Lasers in Engineering*, vol. 37, pp. 101–114, 2002.
- [6] G. Zheng, L. Xu, X. Zou, and Y. Liu, "Excitation of surface phonon polariton modes in gold gratings with silicon carbide substrate and their potential sensing applications," *Applied Surface Science*, vol. 396, pp. 711–716, 2017.
- [7] D. A. Chen, R. Hamam, and G. Chen, "Extraordinary optical transmission through subwavelength holes in a polaritonic silicon dioxide film," *Applied Physics Letters*, vol. 90, p. 181 921, 2017.
- [8] W. L. Barnes, A. Dereux, and T. W. Ebbenen, "Surface plasmon subwavelength optics," *Nature*, vol. 424, pp. 824–830, 2003.
- [9] T. W. Ebbensen, H. J. Lezec, H. F. Ghaemi, T. Thio, and P. A. Wolff, "Extraordinary optical transmission through sub-wavelength hole arrays," *Nature*, vol. 391, pp. 667–669, 1998.
- [10] B. K. Rodrigo, F. D. L. Perez, and L. Martin-Mereno, "Extraordinary optical transmission: Fundamentals and applications," *Proceedings of the IEEE*, vol. 104, pp. 2288–2306, 2016.
- [11] H. Liu and P. Lalanne, "Microscopic theory of the extraordinary optical transmission," *Nature*, vol. 452, pp. 728–730, 2008.

- [12] K. J. K. Koerkamp, S. Enoch, F. B. Segerink, N. F. van Hulst, and L. Kuipers, "Strong influence of hole shape on extraordinary optical transmission through periodic arrays of subwavelength holes," *Phys. Rev. Lett.*, vol. 92, 2004.
- [13] S. G. Rodrigo, "Holes with very acute angles: A new paradigm of extraordinary optical transmission through strongly localized modes," *Opt. Exp.*, vol. 18, pp. 23 691–23 697, 2010.
- [14] S. G. Rodrigo, F. J. García-Vidal, and L. Martín-Moreno, "Theory of absorption-induced transparency," *Phys. Rev. B*, vol. 88, 2013.
- [15] X. Zong, "Waveguide and plasmonic absorption induced transparency," *ACS Nano*, vol. 10, pp. 4570–4578, 2016.
- [16] A. Alù, G. D'Aguanno, N. Mattiucci, and M. J. Bloemer, "Plasmonic brewster angle: Broadband extraordinary transmission through optical gratings," *Phys. Rev. Lett.*, vol. 106, 2011.
- [17] T. Ding, M. Hong, A. M. Richards, T. I. Wong, X. Zhou, and C. L. Drum, "Quantification of a cardiac biomarker in human serum using extraordinary optical transmission (EOT)," *PLoS ONE*, vol. 10, 3 2015.
- [18] D. Sato and N. Yamada, "Review of photovoltaic module cooling methods and performance evaluation of the radiative cooling method," *Renewable and Sustainable Energy Reviews*, vol. 104, pp. 151–166, 2019.
- [19] J. Liu, D. Zhang, S. Jiao, Z. Zhou, Z. Zhang, and F. Gao, "Daytime radiative cooling with clear epoxy resin," *Solar Energy Materials and Solar Cells*, vol. 207, p. 110 368, 2020.
- [20] E. Rephaeli, A. Raman, and S. Fan, "Ultrabroadband photonic structures to achieve high-performance daytime radiative cooling," *Nano Letters*, vol. 13, pp. 1457–1461, 2013.
- [21] B. Bhatia, A. Leroy, Y. Shen, L. Zhao, M. Gianello, D. Li, T. Gu, J. Hu, M. Soljacic, and E. N. Wang, "Ultrabroadband photonic structures to achieve high-performance daytime radiative cooling," *Natures Communications*, vol. 5001, pp. 1457–1461, 2018.
- [22] Y. Zhai, Y. Ma, S. N. David, D. Zhao, R. Lou, G. Tan, R. Yang, and X. Yin, "Scalable-manufactured randomized glass-polymer hybrid metamaterial for day-time radiative cooling," *Science*, vol. 355, pp. 1062–1066, 2014.

- [23] J. Huang, M. Li, and D. Fan, "Core-shee particles for devising high-performance full-day radiative cooling paint," *Applied Materials Today*, vol. 25, p. 101 209, 2021.
- [24] J. Hollick, "Nocturnal radiation cooling tests," *Energy Procedia*, vol. 30, pp. 930–936, 2012.
- [25] M. Dong, N. Chen, X. Zhao, S. Fan, and Z. Chen, "Nighttime radiative cooling in hot and humid climates," *Optics Express*, vol. 27, pp. 31587–31598, 2019.
- [26] E. Rephaeli, A. Raman, and S. Fan, "Ultrabroadband photonic structures to achieve high-performance daytime radiative cooling," *American Chemical Society*, vol. 13, 4 2013.
- [27] M. M. Hossain, B. Jia, and M. Gu, "A metamaterial emitter for highly efficient radiative cooling," *Advanced Optical Materials*, vol. 3, 8 2015.
- [28] L. Zhou, H. Song, J. Liang, M. Singer, M. Zhou, E. Stegenburgs, N. Zhang, C. Xu, T. Ng, Z. Yu, B. Ooi, and Q. Gan, "A polydimethylsiloxane-coated metal structure for all-day radiative cooling," *Nature Sustainability*, vol. 2, pp. 718–724, 2019.
- [29] A. P. Raman, M. A. Anoma, L. Zhu, E. Rephaeli, and S. Fan, "Passive radiative cooling below ambient air temperature under direct sunlight," *Nature*, vol. 515, pp. 540–544, 2014.
- [30] Y. Zhai, Y. Ma, S. N. David, D. Zhao, R. Lou, G. Tan, R. Yang, and X. Yin, "Scalable-manufactured randomized glass-polymer hybrid metamaterial for day-time radiative cooling," *Science*, vol. 355, pp. 1062–1066, 2014.
- [31] L. Zhou, H. Song, J. Liang, M. Singer, M. Zhou, E. Stegenburgs, N. Zhang, C. Xu, T. Ng, Z. Yu, B. Ooi, and Q. Gan, "A polydimethylsiloxane-coated metal structure for all-day radiative cooling," *Nature Sustainability*, vol. 2, 2019.
- [32] T. Wang, Y. Wu, L. Shi, X. Hu, M. Chen, and L. Wu, "A structural polymer for highly efficient all-day passive radiative cooling," *Nature Communications*, vol. 12, 2021.
- [33] P. Yang, C. Chen, and Z. M.Zhang, "A dual-layer structure with record-high solar reflectance for daytime radiative cooling," *Solar Energy*, vol. 169, 2018.
- [34] Kreith, F and Bohn, M S, *Principles of heat transfer*. United States, 1986.
- [35] Vedat S. Arpacz, Conduction heat transfer. Addison Wesley, 1966.
- [36] Young, Hugh D., *University Physics*, 7th Ed. Addison Wesley, 1992.

- [37] Young, H.D. and Freedman, R. A., *University Physics*, 11th Ed. Pearson, 2004.
- [38] M. Iguchi and O. J. Ilegbusi, *Convection heat transfer in Basic Transport Phenomena in Materials Engineering*. Springer, Tokyo, 2013.
- [39] X. Yin, R. Yang, G. Tan, and S. Fan, "Terrestrial radiative cooling: Using the cold universe as a renewable and sustainable energy source," *Science*, vol. 370, pp. 786–791, 2020.
- [40] S. Catalanotti, V. Cuomo, G. Piro, D. Ruggi, V. Silvestrini, and G. Troise, "The radiative cooling of selective surfaces," *Solar Energy*, vol. 17, pp. 83–89, 2 1975.
- [41] C. G. Granqvist and A. Hjortsberg, "Radiative cooling to low temperatures: General considerations and application to selectively emitting sio films," *Journal of Applied Physics*, vol. 52, pp. 4205–4220, 6 1981.
- [42] T. Fujieda, "An improved equation for estimating diurnal atmospheric radiation near the surface in japan," *Papers in Meteorology and Geophysics*, vol. 67, pp. 1–14, 2018.
- [43] M. M. Hossain and M. Gu, "Radiative cooling: Principles, progress, and potentials," *Advanced Science*, vol. 3, p. 1500360, 2016.
- [44] T. Elder and J. Strong, "The infrared transmission of atmospheric windows," *Journal of the Franklin Institute*, vol. 6, 1953.
- [45] D. Li, Y. Li, Y. Su, C. Chi, and B. Huang, "Atmospheric-window-matching hierarchical broadband infrared absorber realized by lithography-free fabrication," *Frontiers in Energy Research*, vol. 6, 2018.
- [46] T. Suichi, A. Ishikawa, Y. Hayashi, and K. Tsuruta, "Performance limit of daytime radiative cooling in warm humid environment," *AIP Advance*, vol. 8, pp. 1–7, 6 2018.
- [47] B. Bhatia, A. Leroy, Y. Chen, L. Zhao, M. Gianello, D. Li, T. Gu, J. Hu, M. Soljacic, and E. N. Wang, "Passive directional sub-ambient daytime radiative cooling," *Nature Communications*, vol. 9, 2018.
- [48] N. M. Nahar, P. Sharma, and M. M. Purohit, "Performance of different passive techniques for cooling of buildings in arid regions," *Building and Environment*, vol. 38, pp. 109–116, 2003.
- [49] I. E. Agency, "The future of cooling: Opportunities for energy-efficient air conditioning," *Paris*, 2018.

- [50] M. Sodha, U. Singh, A. Srivastava, and G. Tiwari, "Experimental validation of thermal model of open roof pond," *Building and Environment*, vol. 16, pp. 93–98, 1981.
- [51] J. Chen and L. Lu, "Development of radiative cooling and its integration with buildings: A comprehensive review," *Solar Energy*, vol. 212, pp. 125–151, 2020.
- [52] G. Mihalakakou, A. Ferrante, and J. Lewis, "The cooling potential of a metallic nocturnal radiator," *Energy Building*, vol. 28, pp. 251–256, 1998.
- [53] S. Hodo-Abalo, M. Banna, and B. Zeghmati, "Performance analysis of a planted roof as a passive cooling technique in hot-humid tropics," *Renew Energy*, vol. 39, pp. 140–148, 2012.
- [54] B. Zhao, M. Hu, X. Ao, N. Chen, and G. Pei, "Radiative cooling: A review of fundamentals, materials, applications, and prospects," *Applied Energy*, vol. 236, pp. 489–513, 2019.
- [55] M. Taleghami, M. Tenpierik, A. Dobbelsteen, and D. J. Sailor, "Heat mitigation strategies in winter and summer: Field measurements in temperate climates," *Building and Environment*, vol. 81, pp. 309–319, 2014.
- [56] X. Lu, P. Xu, H. Wang, T. Yang, and J. Hou, "Cooling potential and applications prospects of passive radiative cooling in buildings: The current state-of-the-art," *Renewable and Sustainable Energy Reviews*, vol. 65, pp. 1079–1097, 2016.
- [57] L. Zhu, A. Raman, K. X. Wang, M. A. Anoma, and S. Fan, "Radiative cooling of solar absorbers using a visibly transparent photonic crystal thermal blackbody," *Applied Physical Sciences*, vol. 112, pp. 32–38, 2015.
- [58] Y. An, C. Sheng, and X. Li, "Radiative cooling of solar cells: Opto-electro-thermal physics and modeling," *Nanoscale*, vol. 11, pp. 17073–17083, 2019.
- [59] A. D. Jones and C. P. Underwood, "A thermal model for photovoltaic systems," *Solar Energy*, vol. 70, pp. 349–359, 2001.
- [60] L. Zhu, A. Raman, K. X. Wang, M. A. Anoma, and S. Fan, "Radiative cooling of solar cells," *Optica*, vol. 1, pp. 32–38, 2014.
- [61] S. Kurtz, K. Whitfield, G. TamizhMani, M. Koehl, D. Miller, J. Joyce, J. Wohlgemuth, N. Bosco, M. Kempe, and T. Zgonena, "Evaluation of high-temperature exposure of photovoltaic modules," *Progress in Photovoltaics: Research and Applications*, vol. 19, pp. 954–965, 2011.

- [62] Z. Wang, D. Kortge, J. Zhu, Z. Zhou, H. Torsina, C. Lee, and P. Bermel, "Lightweight, passive radiative cooling to enhance concentrating photovoltaics," *Joule*, vol. 4, pp. 2702–2717, 2020.
- [63] T. Oki and S. Kanae, "Global hydrological cycles and world water resources," *Science*, vol. 313, pp. 1068–1072, 2006.
- [64] M. Zhou, H. Song, X. Xu, A. Shahsafi, Y. Qu, Z. Xia, Z. Ma, M. A. Kats, J. Zhu, B. S. Ooi, Q. Gan, and Z. Yuo, "Vapor condensation with daytime radiative cooling," *PNAS*, vol. 118, pp. 1–7, 2021.
- [65] H. Park, I. Haechler, G. Schnoering, M. D. Ponte, T. M. Schutzius, and D. Poulikako, "Enhanced atmospheric water harvesting with sunlight-activated sorption ratcheting," *Progress in Photovoltaics: Research and Applications*, vol. 14, pp. 2237–2245, 2022.
- [66] J. Brick and B. Vila, *Solved! What to Do About Condensation on Windows*, https://www.bobvila.com/articles/condensation-on-windows/.
- [67] B. Schonewille, Hand wearing glove scratching ice from car window with frost in winter, https://www.123rf.com/photo\_42354654\_hand-wearing-glove-scratching-ice-from-car-window-with-frost-in-winter.html.
- [68] K. Rykaczewski, S. Anand, S. Bengaluru, and K. K. Varanasi, "Mechanism of frost formation on lubricant-impregnated surface," *American Chemical Society*, vol. 29, pp. 5230–5238, 2013.
- [69] Z. Zhao, H. Chen, X. Lin, L. Hong, and L. D. Zhang, "Development of high-efficient synthetic electric heating coating for anti-icing/de-icing," *Surface and Coatings Technology*, vol. 349, pp. 340–346, 2018.
- [70] S. Glagolev, A. Shevtsova, and S. Shekhovtsova, "Basis for application of new-generation anti-icing materials as an efficient way to reduce the accident rate on roads in winter," *Transportation Research Procedia*, vol. 36, pp. 193–198, 2018.
- [71] L. Li, Y. Liu, Z. Zhang, and H. Hu, "Effects of thermal conductivity of airframe substrate on the dynamic ice accretion process pertinent to USA inflight icing phenomena," *International Journal of Heat and Mass Transfer*, vol. 131, pp. 1184–1195, 2019.
- [72] Craig F. Bohren and Donald R. Huffman, *Absorption and scattering by a sphere*. A Wiley-Interscience Publication, 1983.

- [73] John B. Schneider, *Understanding the Finite-Difference Time-Domain Method*. John B. Schneider, 2017.
- [74] I. H. Malitson, "Interspecimen comparison of the refractive index of fused silica," *J. Opt. Soc. Am.*, vol. 10, pp. 1205–1209, 1965.
- [75] R. Kitamura, L. Pilon, and M. Jonasz, "Optical constants of silica glass from extreme ultraviolet to far infrared at near room temperature," *Appl. Opt.*, vol. 33, pp. 8118–8133, 2007.
- [76] T. L. Myers, R. G. Tonkyn, T. O. Danby, M. S. Taubman, B. E. Bernacki, J. C. Birnbaum, S. W. Sharpe, and T. J. Johnson, "Accurate measurement of the optical constants n and k for a series of 57 inorganic and organic liquids for optical modeling and detection," *Appl. Spectrosc.*, vol. 4, pp. 535–550, 2018.
- [77] https://refractiveindex.info..
- [78] R. L. Olmon, B. Slovick, T. W. Johnson, D. Shelton, S.-H. Oh, G. D. Boreman, and M. B. Raschke, "Optical dielectric function of gold," *Phys. Rev. B*, vol. 23, p. 235 147, 2012.
- [79] A. D. Rakić, "Algorithm for the determination of intrinsic optical constants of metal films: Application to aluminum," *Applied Optics*, vol. 34, pp. 4755–4767, 1995.
- [80] T. M. J. Nilsson and G. A. Niklasson, "Radiative cooling during the day: Simulations and experiments on pigmented polyethylene cover foils," *Solar Energy Materials and Solar Cells*, vol. 37, 1 1995.
- [81] A. Aili, X. Yin, and R. Yang, "Passive sub-ambient cooling: Radiative cooling versus evaporative cooling," *Appl. Therm. Eng.*, vol. 202, 2022.
- [82] A. P. Raman, M. A. Anoma, L. Zhu, E. Rephaeli, and S. Fan, "Passive radiative cooling below ambient air temperature under direct sunlight," *Nature*, vol. 514, pp. 540–544, 2014.
- [83] L. Zhou, H. Song, J. Liang, M. Singer, M. Zhou, E. Stegenburgs, N. Zhang, C. Xu, T. Ng., Z. Yu, B. Ooi, and Q. Gan, "A polydimethylsiloxane-coated metal structure for all-day radiative cooling," *Nature Sustainability*, vol. 2, pp. 718–724, 2019.
- [84] *Modtran*, *webstite*, http://modtran.spectral.com/modtran\_index, 2021.
- [85] A. M. M. Gherman, A. Vladescu, A. E. Kiss, and C. Farcau, "Extraordinary optical transmission through titanium nitride-coated microsphere lattice," *Photonics Nanostructures: Fundam. Appl.*, vol. 38, p. 100762, 2020.

- [86] L. Landstroem, D. Brodoceanu, D. Baeuerle, F. J. Garcia-Vidal, S. G. Rodrigo, and L. Martin-Moreno, "Extraordinary transmission through metal-coated monolayers of microspheres," *Optic Express*, vol. 17, pp. 761–772, 2009.
- [87] W. S. Rasband, *Imagej, u. s. national institutes of health, bethesda, maryland,* USA, https://imagej.nih.gov/ij/.
- [88] C. A. Schneider, W. S. Rasband, and K. Eliceiri, "Nih image to imagej: 25 years of image analysis," *Nat. Methods*, vol. 7, pp. 671–675, 2012.
- [89] G. L. Whitworth, J. Jaramillo-Fernandez, J. A. Pariente, P. D. Garcia, A. Blanco, C. Lopez, and C. M. Sotomayor-Torres, "Simulations of micro-sphere/shell 2d silica photonic crystals for radiative cooling," *Optics Express*, vol. 29, 11 2021.
- [90] J. Jaramillo-Fernandez, G. L. Whitworth, J. A. Pariente, A. Blanco, P. D. Garcia, C. Lopez, and C. M. Sotomayor-Torres, "A self-sssembled 2d thermofunctional material for radiative cooling," *Small*, vol. 15, 1905290 2019.
- [91] M. M. Junda and N. J. Podraza, Optical properties of soda lime float glass from 3 mm to 148 nm (0.41 mev to 8.38 ev) by spectroscopic ellipsometry, https://avs.scitation.org/doi/am-pdf/10.1116/1.5024390.
- [92] K. Kiyota and K. Kajikawa, "Effective medium and equivalent circuit analysis of extraordinary transmission through metallic grating in the infrared range," *OSA Continuum*, vol. 5, pp. 1639–1651, 2019.
- [93] Polyethylene terephthalate (PET): A comprehensive review, https://omnexus.specialchem.com/selection-guide/polyethylene-terephthalate-pet-plastic.
- [94] *Polyethylene naphthalate (pen) resin teonex*, https://www.teijin-resin.com/products/resin/teonex/.
- [95] AGC chemicals company: Fluoroproducts business, https://www.agc-chemicals.com/jp/en/fluorine/products/detail/index.html?pCode=JP-EN-F002.
- [96] K. Ravindranath and R. A. Mashelkar, "Polyethylene terephthalate—ii. engineering analysis," *Chemical Engineering Science*, vol. 41, 12 1989.
- [97] P. Asgari, O. Moradi, and B. Tajeddin, "The effect of nanocomposite packaging carbon nanotube base on organoleptic and fungal growth of mazafati brand dates," *Int Nano Lett*, vol. 98, pp. 1–6, 2014.

- [98] M. T. Dang, J. Lefebvre, and J. D. Wuest, "Recycling indium tin oxide (ito) electrodes used in thin-film devices with adjacent hole-transport layers of metal oxides," *ASC Sustainable Chem.Eng*, vol. 12, pp. 3373–3381, 2015.
- [99] W. Gao and Z. Li, "zno thin films produced by magnetron sputtering," *Ceramics international*, vol. 30, pp. 1155–1159, 2004.
- [100] H. Shen and C. Yang, "Preparation and properties of AZO thin films on different substrates," *Progress in Natural Science: Materials International*, vol. 20, pp. 44–48, 2010.
- [101] S. Bouden, A. Dahi, F. Hauquier, H. Randriamahazaka, and J. Ghilane, "Multifunctional indium tin oxide electrode generated by unusual surface modification," *Scientific Reports*, vol. 6, pp. 35 191–35 205, 2016.
- [102] J. Y. Lee, S. T. Connor, Y. Cui, and P. Peumans, "Semitransparent organic photovoltaic cells with laminated top electrode," *Nano Letters*, vol. 10, pp. 1276–1279, 2010.
- [103] J.-Y. Lee, S. T. Connor, Y. Cui, and P. Peumans, "Solution-processed metal nanowire mesh transparent electrodes," *Nano Letters*, vol. 8, no. 2, pp. 689–692, 2008.
- [104] A. R. Madaria, A. Kumar, F. N. Ishikawa, and C. Zhou, "Uniform, highly conductive, and patterned transparent films of a percolating silver nanowire network on rigid and flexible substrates: Using a dry transfer technique," *Nano Research*, vol. 3, pp. 564–573, 2010.
- [105] T. Kim, A. Canlier, G. H. Kim, J. Choi, M. Park, and S. M. Han, "Electrostatic spray deposition of highly transparent silver nanowire electrode on flexible substrate," *Applied Materials and Interfaces*, vol. 5, pp. 788–794, 2013.
- [106] H. Kim and C. M. Gilmore, "Electrical, optical, and structural properties of indium—tin—oxide thin films for organic light-emitting devices," *Journal of Applied Physics*, vol. 86, pp. 6451–6461, 1999.
- [107] C. M. Lampert, "Heat mirror coatings for energy conserving windows," *Solar Energy Materials*, vol. 6, 1981.
- [108] A. P. Amalathas and M. Alkaisi, "Effects of film thickness and sputtering power on properties of ito thin films deposited by rf magnetron sputtering without oxygen," *Journal of Materials Science: Materials in Electronics*, vol. 10, pp. 11 064–11 071, 2016.

- [109] R. E. Treharne, A. Seymour-Pierce, K. Durose, K. Hutchings, S. Roncallo, and D. Lane, "Optical design and fabrication of fully sputtered cdte/cds solar cells," *J. Phys: Conf. Ser.*, vol. 286, p. 012 038, 2011.
- [110] C. Ji, D. Liu, C. Zhang, and L. J. Guo, "Ultrathin-metal-film-based transparent electrodes with relative transmittance surpassing 100%," *Nature Communications*, vol. 11, p. 3367, 2020.
- [111] D. R. Proffitt, The effects of motor vehicle window tinting on traffic safety and enforcement: Final report: A report to the governor and general assembly in response to senate joint resolution 293, 1993 session. Report Number: VTRC 94-R14;VTRC 94-R141, https://rosap.ntl.bts.gov/view/dot/19355, 1994.
- [112] D. R. Smith and E. V. Loewenstein, "Optical constants of far infrared materials. 3: Plastics," *Applied Optics*, vol. 14, pp. 1335–1341, 1975.